REVIEW ARTICLE

Key Points:
- We describe FORC diagrams, including measurements and calculations
- Interpretation of magnetic particle behavior using FORC diagrams is discussed
- Technical and interpretational considerations are useful in many applications

Understanding fine magnetic particle systems through use of first-order reversal curve diagrams

Andrew P. Roberts[1], David Heslop[1], Xiang Zhao[1], and Christopher R. Pike[1]

[1]Research School of Earth Sciences, Australian National University, Canberra, ACT, Australia

Abstract First-order reversal curve (FORC) diagrams are constructed from a class of partial magnetic hysteresis loops known as first-order reversal curves and are used to understand magnetization processes in fine magnetic particle systems. A wide-ranging literature that is pertinent to interpretation of FORC diagrams has been published in the geophysical and solid-state physics literature over the past 15 years and is summarized in this review. We discuss practicalities related to optimization of FORC measurements and important issues relating to the calculation, presentation, statistical significance, and interpretation of FORC diagrams. We also outline a framework for interpreting the magnetic behavior of magnetostatically noninteracting and interacting single domain, superparamagnetic, multidomain, single vortex, and pseudosingle domain particle systems. These types of magnetic behavior are illustrated mainly with geological examples relevant to paleomagnetism, rock magnetism, and environmental magnetism. These technical, experimental, and interpretational considerations are relevant to applications that range from improving particulate media for magnetic recording in materials science, to providing a foundation for understanding geomagnetic recording by rocks in geophysics, to interpreting depositional, microbiological, and environmental processes in sediments.

1. Introduction

First-order reversal curve (FORC) diagrams [*Pike et al.*, 1999; *Roberts et al.*, 2000] provide important insights into the magnetic properties of the rock-forming minerals responsible for diverse magnetic signals in rock magnetism, environmental magnetism, and paleomagnetism. FORC diagrams have, therefore, become a popular tool in these research fields. FORC diagrams have also proved useful for probing the behavior of magnetic particulate arrays in the magnetic recording industry and are widely used in solid-state physics. The differences between "dirty" geological samples and "clean" magnetic particulate arrays have resulted in an understandable divergence in research involving FORC diagrams. Nevertheless, there remains considerable scope for developments from these different research spheres to inform each other. The concepts that underpin FORC diagrams are based on the formalism of *Preisach* [1935]; however, an interpretive framework for the Preisach diagram did not materialize until development of the phenomenological model of *Néel* [1954]. Likewise, over the last decade or so, much attention has been given to understanding the magnetic information provided by FORC diagrams. A sophisticated and detailed literature has emerged, published both in the geophysics and solid-state physics literature, that provides valuable details concerning measurement, calculation, presentation, and interpretation of the response of magnetic particle systems in FORC diagrams through theoretical, experimental, numerical and micromagnetic modeling, and statistical approaches. The importance of these advances makes it timely to provide an overview of the state of the art in understanding fine magnetic particle systems using FORC diagrams.

2. Magnetic Hysteresis

Magnetic hysteresis loops (Figure 1a) are measured while subjecting a sample to an applied magnetic field cycle. Measurement of a major hysteresis loop usually starts at a strong positive field, which is reduced to zero and continuously swept in the opposite direction to high negative values, and then back to the strong original positive field. Application of a large positive magnetic field is aimed at saturating the magnetization to provide a measure of the saturation magnetization (M_s). When the applied field reaches peak negative values, the magnetization approaches $-M_s$. The magnetization remaining when the applied field is reduced to zero is referred to as the saturation remanent magnetization (M_{rs}). The field at which the magnetization is reduced to zero is known as the coercive force (B_c). This set of measurements is referred to as a hysteresis loop
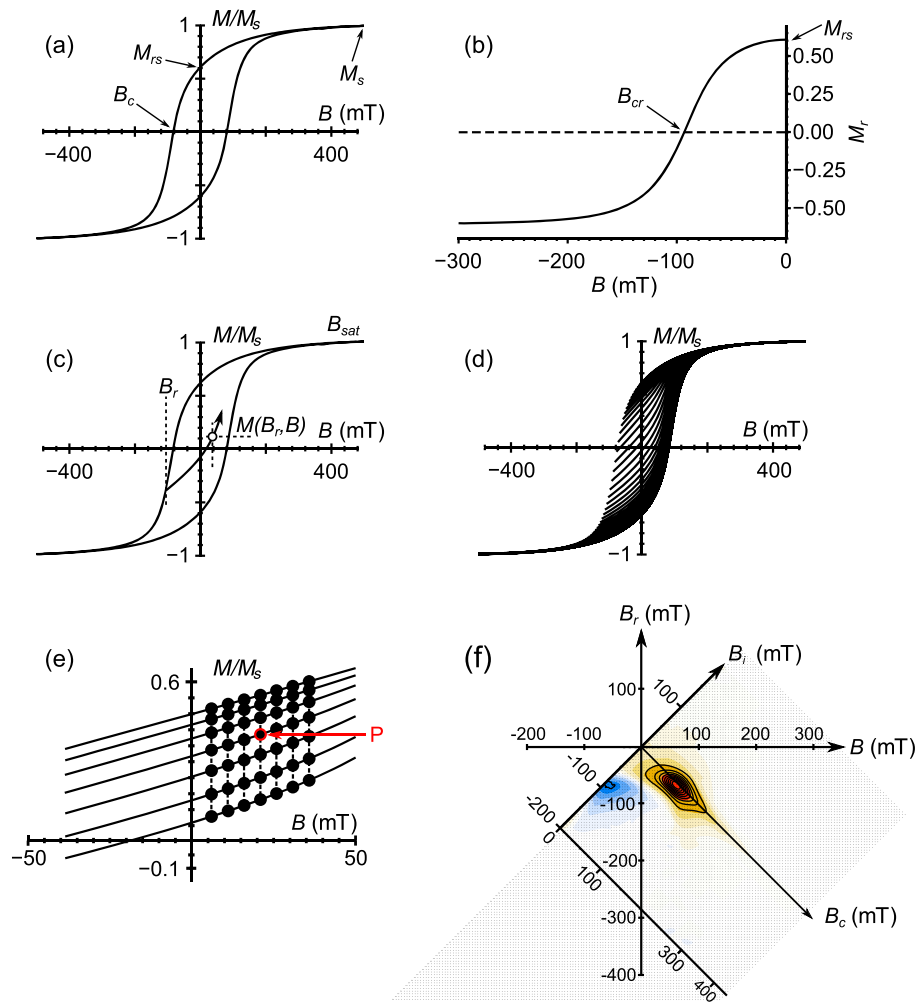
Figure 1. Definitions of key parameters and concepts. Examples are all from a floppy recording disk with strongly interacting stable SD particles. (a) Major hysteresis loop with definition of M_{rs}, M_s, and B_c. (b) Backfield demagnetization curve, with definition of M_{rs} and B_{cr}. (c) Definition of a FORC. Measurement starts at B_r, with magnetization measurements along the FORC represented by $M(B_r, B)$ en route back to positive saturation, M_s, at the saturating field, B_{sat}. (d) Suite of FORCs, where the outer envelope of the FORCs defines the major hysteresis loop. (e) Illustration of how the FORC distribution $\rho(B_r, B)$ is calculated at a point P using measurements from consecutive FORCs for SF = 3. That is, smoothing is performed over a 7 × 7 grid (from $(2SF + 1)^2$) about P. (f) Grid of measurement fields that illustrates the relationship between $\{B_r, B\}$ space and the transformation to $\{B_i, B_c\}$ space with a FORC distribution superimposed for illustration. Measurement of data points beyond the upper, lower, and right-hand limits of the FORC diagram enables rigorous calculation of $\rho(B_r, B)$ to the limits of the FORC diagram at the required SF value. Each row of data points corresponds to measurements along a single FORC. The two closely spaced data points at the beginning of each FORC correspond to the initial less precise attempt to sweep the magnet from B_{sat}, while the second data point is the more precisely controlled field value for B_r. The second, rather than the first, measurement is used to calculate $\rho(B_r, B)$.

because, for many magnetic materials, the measured magnetization does not describe a reversible curve; the difference between the upper and lower branches of the hysteresis loop results from a lag of the magnetization with respect to the forcing due to application of the magnetic field [*Ewing*, 1882]. Magnetic hysteresis is a fundamentally important phenomenon that is useful for characterizing magnetic particle systems and is the subject of the present paper. In addition to hysteresis loops, remanence curves, such as isothermal remanent magnetization (IRM) acquisition and backfield demagnetization curves, are often measured. A backfield demagnetization curve (Figure 1b) is measured after applying a strong (saturating) positive field. When $+M_{rs}$ has been measured, the sample is then progressively demagnetized by applying a direct current backfield in the opposite direction to that used to impart M_{rs} until the IRM decays to zero and

then becomes fully saturated in the opposite direction at $-M_{rs}$. The field at which the IRM is reduced to zero is known as the coercivity of remanence (B_{cr}). In paleomagnetism and environmental magnetism, we are most interested in particles that carry a remanent magnetization, which makes remanence curves an important supplement to hysteresis measurements.

Magnetic hysteresis arises due to various effects: through coherent rotation of the magnetic moment in uniformly magnetized single domain (SD) particles, through more complex modes of magnetic moment reversal, including curling, buckling, and fanning, or vortex nucleation and annihilation in nonuniformly magnetized particles, or through a series of irreversible steps known as Barkhausen jumps [*Barkhausen*, 1935] associated with domain wall dynamics in nonuniformly magnetized multidomain (MD) particles. A typical hysteresis loop will appear as a smooth function (Figure 1a), which can be the product of a large number of infinitesimally small events (with respect to the total magnetization of the particle system) of any of these types. The fact that such a wide range of microscopic magnetic processes can be studied with hysteresis measurements explains why magnetic hysteresis is so useful in fine particle magnetism.

3. What Are FORC Diagrams?

FORC diagrams are calculated from a class of partial magnetic hysteresis curves known as first-order reversal curves [*Mayergoyz*, 1986]. A FORC is measured by first magnetically saturating a sample (if possible) in a strong positive applied field (B_{sat}). The field is then decreased to a so-called reversal field, B_r. A FORC is the magnetization curve that is measured at a series of approximately evenly spaced applied fields, B, from B_r to B_{sat} (Figure 1c). The magnetization at any field B with reversal field B_r is denoted as $M(B_r, B)$, where $B \geq B_r$ (Figure 1c), and the field spacing is denoted by δB. Multiple FORCs are measured for a range of evenly spaced B_r values (Figure 1d) to obtain the gridded magnetization measurements needed (Figure 1e) to create a FORC diagram (Figure 1f). Magnetization data from consecutive measurement points on consecutive FORCs (Figure 1e) are used to determine the FORC distribution, which is defined as a mixed second derivative [*Wilde and Girke*, 1959; *Mayergoyz*, 1986; *Pike et al.*, 1999]:

$$\rho(B_r, B) = -\frac{1}{2}\frac{\partial^2 M(B_r, B)}{\partial B_r \partial B}, \tag{1}$$

where $\rho(B_r, B)$ is well defined for $B \geq B_r$. The second derivative is scaled by -0.5 because the magnetization switch from $+M_s$ to $-M_s$ has a magnitude of $2M_s$. Purely reversible magnetization components (e.g., due to paramagnetism or diamagnetism) do not exhibit hysteresis, so will be eliminated by the mixed second derivative and will not contribute to a FORC distribution. When plotting a FORC distribution, it is convenient to change coordinates from $\{B_r, B\}$ to

$$\{B_c = (B_r - B)/2, B_i = (B_r + B)/2\} \tag{2}$$

as illustrated in Figure 1f. The physical meaning of B_c and B_i is discussed in section 5. A FORC diagram is a contour plot of a FORC distribution with B_c and B_i on the horizontal and vertical axes, respectively (Figure 1f). By definition, $B \geq B_r$, so $\rho(B_r, B)$ is only well defined for $B_c \geq 0$, so that a FORC diagram is confined to the right-hand half plane. FORC diagrams are often rotated counterclockwise by 45° from the $\{B_r, B\}$ coordinate view shown in Figure 1f, so that the *x-y* Cartesian axes are the B_c and B_i axes of the FORC diagram.

Direct calculation of the mixed second derivative in equation (1) by finite differences from experimental data will amplify measurement noise, which can overwhelm the measured signal. This fundamentally important aspect associated with calculating the mixed second derivative is addressed by smoothing over a suitable range of data points. With uniform field spacing δB, measured data points in the $\{B_r, B\}$ coordinate system fall on an evenly spaced grid (Figures 1e and 1f). To calculate the FORC function $\rho(B_r, B)$ for any measurement point, a local square grid of data points is used with the data point in question, *P*, at the center (Figure 1e). A smoothing factor (SF) is used where the number of grid points is $(2SF + 1)^2$. SF is set at 2 for well-behaved samples and 9 for samples with low signal-to-noise ratios (SF = 9 will degrade the signal so that key features of interest could be easily misinterpreted; it is, therefore, best to use the smallest feasible SF value). The case for SF = 3 is illustrated in Figure 1e, where smoothing occurs over the local grid of 7 × 7 data points from

consecutive FORCs. The mixed second derivative in equation (1) is calculated numerically from the discrete data points by fitting a local polynomial surface [*Pike et al.*, 1999]:

$$a_1 + a_2 B_r + a_3 B_r{}^2 + a_4 B + a_5 B^2 + a_6 B_r B. \tag{3}$$

The mixed second derivative of this polynomial surface is simply a_6, which is scaled by a factor of -0.5 as in equation (1). The value of $-0.5\,a_6$, therefore, represents $\rho(B_r, B)$ at the point of interest on the grid. $\rho(B_r, B)$ is then evaluated at all points on the grid within the boundaries of the FORC diagram; these data are contoured, or are plotted using a continuously varying color map, to represent the FORC distribution (Figure 1f). Optimization of measurements and data processing protocols, including alternative approaches to data smoothing, are discussed in section 6.

For this paper, we obtained original measurement files wherever possible from the authors of studies cited and reprocessed data to provide a consistent presentation style (using the algorithm of *Heslop and Roberts* [2012a]). Where this was not possible, we modified older gray scale FORC diagrams produced with the widely used code of *Pike et al.* [1999] by adjusting them to the nonlinear color map of *Egli et al.* [2010]. The major differences are that these older FORC diagrams do not include significance levels and are contoured with discretely rather than continuously varying colors. Despite these differences, a similar overall appearance has been achieved.

4. Why FORC Diagrams?

Many types of magnetic measurements are used to characterize magnetic particle systems. Why are FORC diagrams useful and what are their advantages with respect to other magnetic measurements? We illustrate the value of FORC diagrams with dirty samples of relevance to geophysics and with clean samples of relevance to solid state physics.

First, in paleomagnetism, four main hysteresis parameters are routinely measured (Figures 1a and 1b) and are used to plot M_{rs}/M_s versus B_{cr}/B_c in a so-called Day diagram [*Day et al.*, 1977]. Data trends in Day diagrams are mainly interpreted in terms of grain size variations [*Dunlop*, 2002]. This type of magnetic granulometry suffers from the fact that bulk magnetic measurements of any type, including hysteresis measurements, represent an average of the magnetic properties of all particles in a sample. In our experience, samples that contain a single magnetic mineral with a narrow grain size range are extremely rare. Even the binary mixtures emphasized by *Dunlop* [2002] are rare in our experience, with samples frequently containing three or more magnetic components [*Heslop and Roberts*, 2012b, 2012c; *Roberts et al.*, 2013]. Multicomponent mixing invalidates the overly simplistic interpretations of Day diagrams that are all too common in the paleomagnetic literature. There is a need for methods that can discriminate between different magnetic components within a sample. In this regard, interpretation of IRM acquisition curves has been significantly enhanced by routine use of unmixing techniques [e.g., *Robertson and France*, 1994; *Kruiver et al.*, 2001; *Heslop et al.*, 2002; *Egli*, 2004]. Unmixing methods are now also available for magnetic hysteresis data and should be useful for this important class of data [*Heslop and Roberts*, 2012c]. FORC diagrams provide a map of the magnetic response of all particles in a sample with irreversible magnetizations in terms of the coercivity and magnetic interaction field distribution (B_c and B_i axes, respectively; for details of the physical meaning of FORC distributions, see section 5 below). Thus, by definition, FORC diagrams provide the broader type of representation needed to assess the full magnetic complexity of a sample compared to the assumed low level of complexity usually associated with interpretation of bulk magnetic parameters. When viewed in these terms, a FORC diagram represents one among several methods that can be applied to unmix a magnetic mineral assemblage into its component parts. However, FORC diagrams have an additional advantage in that they enable assessment of magnetic interactions among particles within a sample. The reliability of IRM unmixing can be affected strongly by undetected magnetostatic interactions [*Heslop et al.*, 2002, 2004]. This sets FORC diagrams apart as an especially useful tool even though FORC measurement times are long compared to many methods. Magnetostatic interactions are important in paleomagnetism and rock magnetism. For example, interactions can nullify partial thermoremanent magnetization (pTRM) additivity [*Thellier*, 1938], which can compromise estimation of ancient absolute geomagnetic field intensity from igneous rocks and archeomagnetic samples [e.g., *Dunlop*, 1969; *Carvallo et al.*, 2006a; *Paterson et al.*, 2010]. Interactions can also significantly affect hysteresis parameters [*Sprowl*, 1990; *Muxworthy et al.*, 2003].
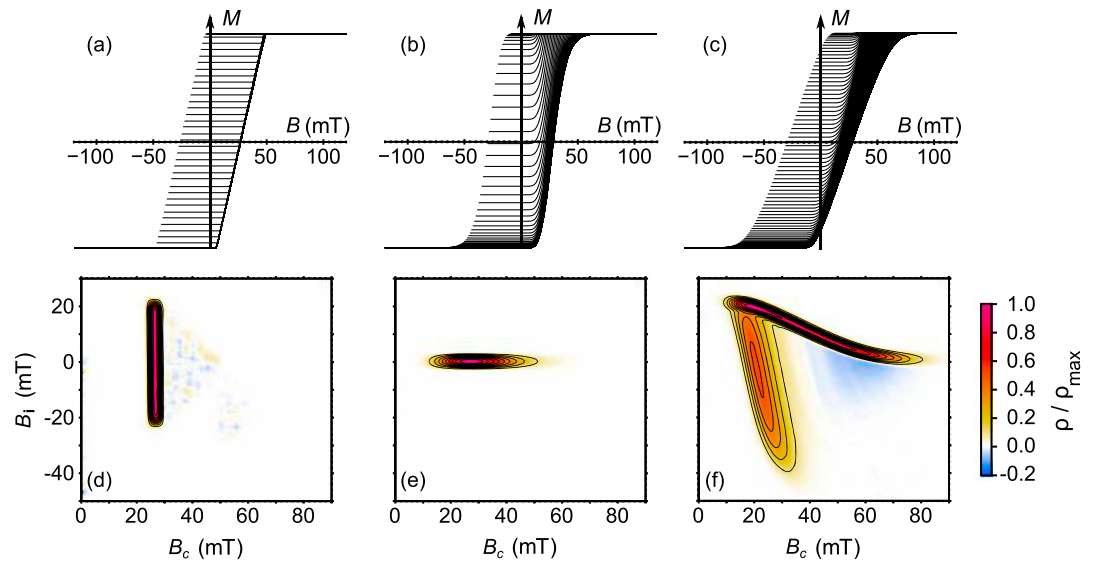
Figure 2. Illustration of how similar hysteresis loops for different (a–c) particle systems can give rise to strongly contrasting (d–f) FORC diagrams. Results are from numerical models for 10^6 hysterons (140 FORCs). In Figures 2a and 2d, a narrow Gaussian coercivity distribution is modeled with mean field interactions. In Figures 2b and 2e, a broader gamma coercivity distribution is modeled with no interactions. In Figures 2c and 2f, a particle system with a gamma coercivity distribution is modeled with a mean interaction field. The diagram in Figure 2f replicates features for a high-density perpendicular nickel nanopillar array. All results were calculated to replicate those of *Pike et al.* [2005].

Use of FORC diagrams helps to recognize such effects. Identification of the inorganic ferrimagnetic remains of magnetotactic bacteria in sediments provides a clear example of the usefulness of FORC diagrams [*Egli et al.*, 2010]. These benefits explain why FORC diagrams have become a popular tool in rock magnetism over the last decade.

Second, in industrially relevant magnetic recording media, it is desirable to manufacture uniform arrays of stable SD particles with high recording fidelity. *Pike et al.* [2005] calculated FORCs for a range of simulated magnetic particle systems (Figures 2a–2c), where the shape of the major hysteresis loops, as indicated by the outer envelope of FORCs, and associated hysteresis parameters, are similar. Despite this similarity, the FORC distributions (Figures 2d–2f) are distinctly different from each other because they reflect fundamentally different magnetization processes within the magnetic particle systems. This indicates that much more information is provided about the switching behavior of magnetic particles from FORC measurements than from a major hysteresis loop alone. FORC distributions are, therefore, a powerful tool for exploring subtle magnetization processes that are unrecognizable in less detailed measurements.

In rock magnetism, we usually aim to characterize samples to determine the types of magnetic particles present. This information is used to understand paleomagnetic recording fidelity or environmental processes. In solid-state physics, the aim is often to understand magnetization processes in novel materials. In both cases, FORC diagrams are a powerful tool for characterizing and investigating magnetic systems. The complexity of features illustrated in Figure 2 reflects the importance of understanding the physical meaning of a FORC distribution (see section 5) and the need for a framework for interpreting FORC diagrams (see section 7).

5. What Is the Physical Meaning of a FORC Distribution?

We use the classical Preisach model [*Preisach*, 1935; *Néel*, 1954] to explain the hysteresis behavior represented in FORC diagrams. In this model, a hysteron (i.e., a rectangular hysteresis loop; Figure 3a) is used to represent the magnetic response of a SD particle with uniaxial anisotropy and coercivity $\pm B_{sw}$ and magnetization states $\pm m_s$ when a magnetic field is applied parallel to its easy axis of magnetization (the easy axis is the most energetically favorable direction of the spontaneous magnetization). If the SD particle is magnetically
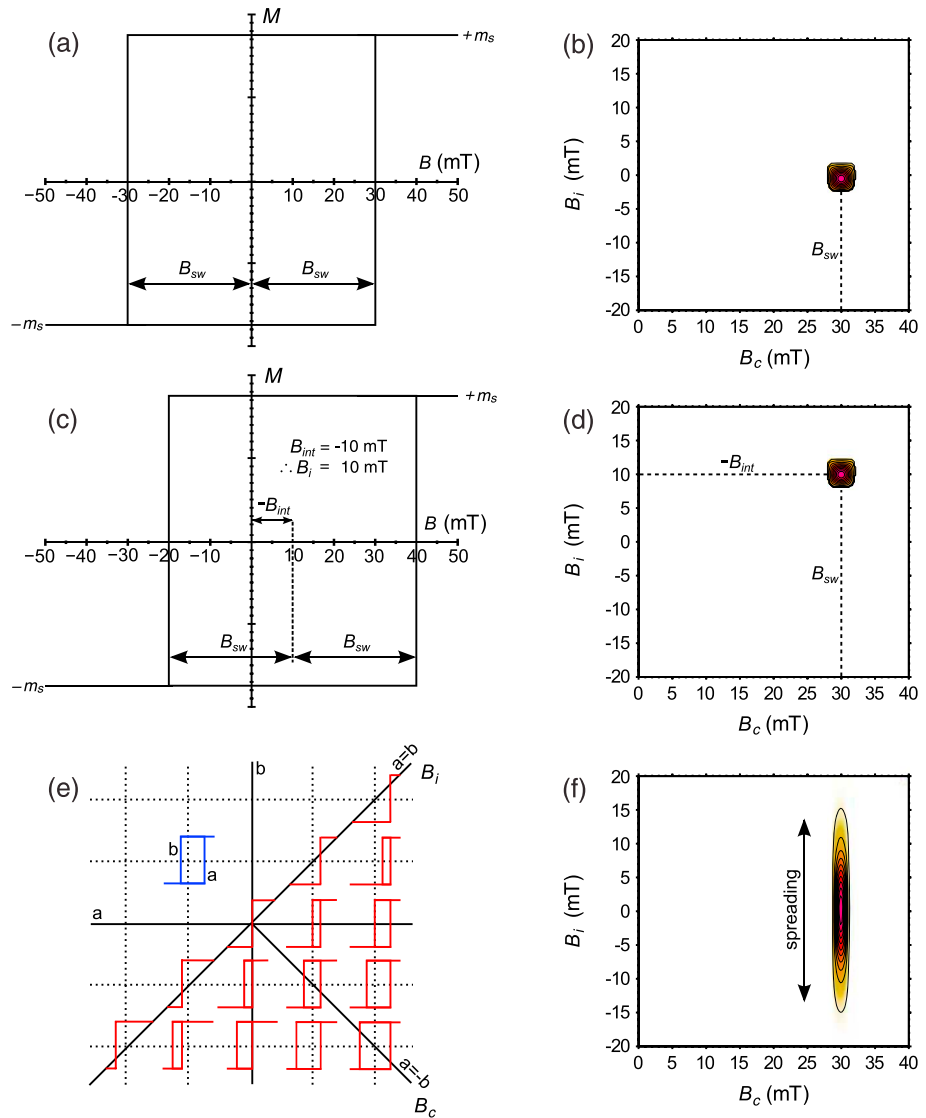
Figure 3. Illustration of how idealized rectangular hysteresis loops (hysterons) for single particles whose easy axis of magnetization is aligned with the applied field can be used to interpret FORC diagrams (based on *Preisach* [1935]). (a) Hysteron with no local interaction field. (b) For the noninteracting hysteron in Figure 3a, the response on the FORC diagram occurs at $B_i = 0$, $B_c = B_{sw}$. (c) Hysteron with an interaction field. (d) For the interacting hysteron in Figure 3c, the FORC diagram response occurs at $B_i = -B_{int}$, $B_c = B_{sw}$. (e) Illustration of how different hysterons for uniaxial interacting SD magnetic particles contribute to different parts of a Preisach (FORC) diagram [after *Fabian and von Dobeneck*, 1997]. (f) Numerical simulation of a Gaussian distribution of local interaction fields for an assemblage of 10^5 hysterons. In this case, $B_c = B_{sw}$, while the vertical spreading is the result of the local interaction field distribution.

isolated, using equation (2), it contributes to a FORC diagram at $\{B_c = B_{sw}, B_i = 0\}$ (Figure 3b). When the same SD particle is placed in a constant local interaction field B_{int} that acts parallel to the applied field (Figure 3c), it will contribute to a FORC diagram at $\{B_c = B_{sw}, B_i = -B_{int}\}$ (Figure 3d). In the case shown in Figure 3c, the local interaction field (B_{int}) of -10 mT will shift the applied external field required for a downward magnetization switch from -30 mT to -20 mT (i.e., $-B_{sw} - B_{int}$). Correspondingly, the same -10 mT interaction field shifts the external field necessary for an upward magnetization switch from $+30$ mT to $+40$ mT (i.e., $+B_{sw} - B_{int}$). Such changes in switching field due to local interactions are represented by B_i, which reflects the shifted position of the hysteron with respect to its position in the absence of an interaction field (so that $B_i = -B_{int}$). With this simple model, to first approximation, a FORC diagram describes the magnetic switching field (coercivity) and local interaction field distributions for the measured SD particle system (e.g., Figure 3d). Graphical illustration of a
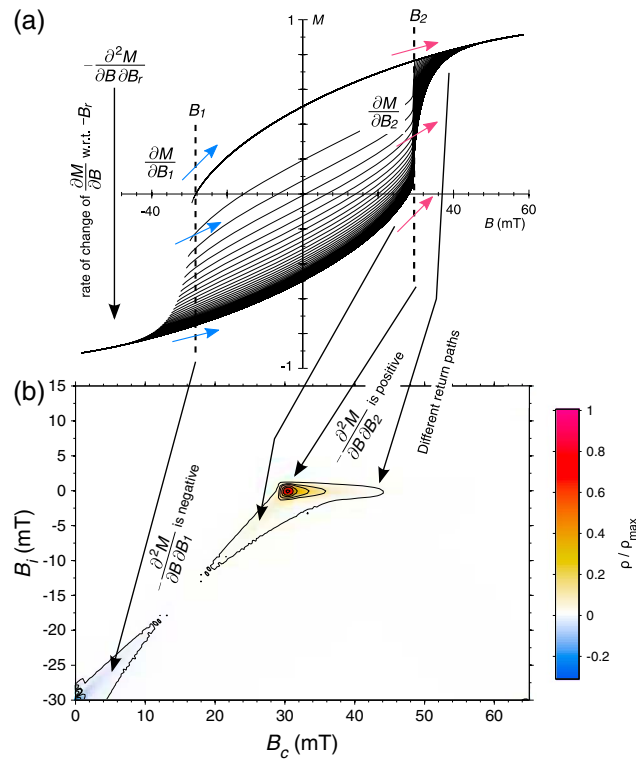
Figure 4. Illustration of how SD particles contribute to different parts of a FORC diagram. (a) FORCs and (b) FORC diagram for a numerical model of 1000 identical noninteracting Stoner-Wohlfarth particles with randomly distributed uniaxial anisotropy. Responses in different regions of the FORC diagram are related to switching events in different parts of the illustrated FORCs (see text for a more detailed explanation) [after *Muxworthy et al.*, 2004].

system of hysterons in Figure 3e [from *Fabian and von Dobeneck*, 1997] provides a visualization of the expected relationship between coercivity and interaction fields in {B_c, B_i} space. Magnetostatic interactions for an assemblage of 10^5 particles with a Gaussian distribution of interaction field strengths give rise to vertical spreading of a FORC distribution (Figure 3f), rather than an isolated peak at a single interaction field (Figure 3d).

While the use of hysterons provides an easy to visualize representation of the physical meaning of FORC diagrams, it is physically unrealistic. For example, in geological samples it is expected that magnetic moments will be randomly oriented, so that perfect alignment of the field with the easy axis of magnetization is not expected in such particle systems. There is an expected continuous variation in hysteresis loop shape for Stoner-Wohlfarth particles from rectangular loops when particles are parallel to the applied field (0°) as in Figure 3, to loops with rounded shoulders when their easy axes are oriented 45° to the field, to loops with no hysteresis when particle easy axes are oriented 90° to the field [*Stoner and Wohlfarth*, 1948].

In Figure 4b, we illustrate a FORC distribution calculated for Stoner-Wohlfarth particles that have hysteresis loops with rounded shoulders (Figure 4a). The resulting FORC distribution is more complicated than for the oversimplified illustrations in Figure 3. A key difference is that such particles can produce a response in more than one part of the FORC diagram [e.g., *Pike and Fernandez*, 1999; *Muxworthy et al.*, 2004; *Newell*, 2005; *Dumas et al.*, 2007a]. For example, uniaxial noninteracting SD particles can give rise to three main features on a FORC diagram [*Muxworthy et al.*, 2004]. The first feature is the expected central peak, the second is an asymmetric "boomerang"-shaped peak around the main peak, while the third is a negative region in the lower left-hand corner of the FORC diagram (see explanations by *Newell* [2005] and *Muxworthy and Roberts* [2007]). The central peak results from the predominant magnetization switching at B_2, which is equivalent to the single switching event for hysterons (Figure 3b). This positive peak is associated with the increase in $\partial M / \partial B_2$ with decreasing B_r (Figure 4a). The lower left-hand part of the boomerang feature is related to FORCs at fields just below the relatively abrupt positive switching field at B_2. The right-hand part of the boomerang is related to differences in FORC return paths as saturation is approached (Figure 4). These return paths are controlled by different particle easy axis orientations with respect to the applied field (because orientation controls coercivity). The return curves are initially dominated by particles oriented ~45° with respect to the field. As B_r decreases, particles with orientations closer to 90° and 0° start to contribute to the FORCs, so that the return path includes contributions from particles with slightly differently shaped FORCs. The right-hand part of the boomerang, therefore, results from moving from the return path for an initial 45°-oriented assemblage, into the return path for a randomly oriented assemblage. The negative region in the lower left-hand part of the FORC diagram is related to sections of the FORCs where $B < 0$ [*Newell*, 2005]. $\partial M / \partial B$ decreases at field B_1 with measurement of successive FORCs (Figure 4a), which causes the negative $\rho(B_r, B)$ values always observed in FORC diagrams for SD particle systems (Figure 4b) [*Muxworthy and Roberts*, 2007].

This decrease in $\partial M/\partial B$ is not as pronounced for $B < 0$; the negative region is, therefore, significantly smaller than the large central peak due to switching events near B_2. If the SD particle assemblage has distributed switching fields, the FORC diagram will stretch out in the B_c direction, which is more typical of natural samples than the assemblage of identical particles depicted in Figure 4. While the hysteron-based explanation for the physical meaning of FORC diagrams is helpful, understanding FORC diagrams requires consideration of the magnitude of the mixed second derivative (equation (1)) throughout a set of measured FORCs.

Interpretation of FORC diagrams as representing coercivity and interaction field distributions has been borne out by rigorous tests of a range of magnetic particle systems [e.g., *Muxworthy and Williams*, 2005; *Egli*, 2006; *Winklhofer and Zimanyi*, 2006; *Dubrota and Stancu*, 2013]. Nevertheless, it is important to recognize that a FORC diagram is a nonunique map of the coercivity and interaction field distributions for a given sample. Many models, with different combinations of magnetization processes, could be developed to explain features observed in FORC diagrams. This is particularly important for material scientists when analyzing new materials where poorly understood magnetization processes could be present. In rock magnetism, this potential ambiguity can be well constrained because extensive work over the last decade or so provides a detailed experimental, theoretical, numerical, micromagnetic, and statistical framework for interpretation of FORC diagrams from geological and archeological materials. This framework is explained in detail in section 7 below.

6. How to Make Good FORC Measurements and Optimal FORC Calculations

Most treatments of FORC measurements emphasize data analysis or interpretation. There has been little emphasis on how to make good measurements. Calculating the mixed second derivative in equation (1) means that any measurement noise will be amplified, which makes acquisition of high-quality FORC measurements highly important. Practical aspects associated with FORC measurements and data processing are outlined in this section. Overlap exists between the issues handled under different subheadings below; readers are, therefore, encouraged to read all subsections if they do not find a complete description under the respective subheadings. Readers who are more interested in interpretation of FORC diagrams can skip to section 7.

6.1. FORC Measurements

FORC measurements can be made with any system that can measure hysteresis data rapidly with high sensitivity. In practice, FORC measurements in rock magnetism are almost always made with Princeton Measurements Corporation MicroMag^{TM} systems (now owned by Lakeshore Cryotronics, Inc.). We discuss measurement procedures in terms of MicroMag^{TM} system commands because this is of greatest relevance to most readers. Nevertheless, our description will be useful for other instruments because of the restricted range of parameters that are important for FORC measurements.

Before starting a FORC measurement sequence, several input parameters must be selected within the MicroMag^{TM} software. These parameters include the saturating field B_{sat}, the range of B_i values that define the upper and lower limits of the desired FORC diagram (given in the software as Hb1 and Hb2), the B_c range for the FORC diagram (Hc1 and Hc2 in the software), the averaging time t_{avg}, the field increment δB, the number of FORCs to be measured N, the maximum SF (up to nine), the pause time to settle at B_{sat}, the pause at the calibration field B_{cal} (the field at which the magnetization is measured before the start of each FORC; successive measurements at this field are used to correct for measurement drift), and the pause at B_r. The choice of most of these parameters depends on the magnetic properties of the sample. For example, a B_{sat} value of 500 mT is appropriate for low-coercivity magnetic minerals such as magnetite and titanomagnetite, but even the highest field that can be applied with the largest MicroMag^{TM} system (2 T) often will not magnetically saturate high-coercivity minerals such as hematite and goethite (e.g., an induction of 57 T can be insufficient to magnetically saturate goethite [*Rochette et al.*, 2005]). In this case, FORC measurements will represent the nonsaturation properties of such minerals. Magnetic measurements are often made to detect high-coercivity minerals within the range of applied fields available using standard equipment. *Roberts et al.* [2006] argued that measurement of nonsaturation properties can be adequate in such contexts and provided FORC diagrams for a range of hematite and goethite samples for this purpose. Other technical considerations are also important for setting the value of B_{sat}. For example, if a sample is saturated at 500 mT,

it is better to use this B_{sat} value rather than, say, 1 T because sweeping the magnet to a larger field and back to B_r will unnecessarily lengthen the measurement time.

As can be seen by the range of B_i and B_c values for FORC diagrams in this paper, setting of the upper and lower limits of a FORC diagram will depend on the magnetic properties of the sample. For SD-dominated systems, the main peak of the FORC diagram will occur around the coercive force of the sample, B_c. It is necessary to choose values of Hb1, Hb2, Hc1, and Hc2 that enable full depiction of the FORC distribution for the sample. When these boundary values are larger, the MicroMag^{TM} software automatically increases the field step size δB. In general, it takes longer to measure high-coercivity minerals such as hematite, compared to low-coercivity minerals such as magnetite. Also, measurement time depends on the aspect ratio of the FORC diagram; a square FORC diagram will optimize measurement time, which becomes longer as the diagram becomes more rectangular [*Muxworthy and Roberts*, 2007]. If δB becomes too large, the resultant FORC diagram will be inadequately defined, which can lead to incorrect interpretations of the strength of magnetostatic interactions within a sample (and is exacerbated by increased smoothing during FORC processing). This becomes particularly important when seeking to assess the absence of interactions in a fine magnetic particle system, such as between intact magnetosome chains produced by magnetotactic bacteria (see *Egli et al.* [2010] for an in-depth discussion, including a table with measurement parameters for ideal resolution of noninteracting SD particle assemblages). Decreasing δB allows better resolution of features on a FORC diagram but also significantly lengthens FORC measurement time and increases noise (as discussed below). Depending on the system and sample, technical considerations can become important for long measurement runs, as outlined in section 6.2. Given the high level of measurement automation, it is often a good strategy to make a rapid (~1 h) low-resolution scan of the entire expected FORC space for a sample and then make high-resolution measurements (several hours to days) of detailed regions of the FORC space in order to characterize details of the magnetic particle system under investigation. This approach has been used extensively for geological samples since *Roberts et al.* [2000], the importance of which was emphasized by *Egli et al.* [2010].

The averaging time t_{avg} is the time taken to measure each data point and is an important parameter (it can vary between 0.1 and 1 s). Increasing t_{avg} will increase the overall measurement time, but it should also improve the signal-to-noise ratio of measurements. It, therefore, seems logical that longer t_{avg} values will provide better measurements for weakly magnetized samples. However, increasing t_{avg} does not remove noise produced by the electromagnet, and it can increase undesired effects associated with instrument drift [*Egli et al.*, 2010]. FORC measurements are made while the field sweeps continuously from B_r to B_{sat}, so larger t_{avg} values will cause averaging over a wider field range and increases errors in achieving the specified measurement field. Thus, the most obvious benefits of longer t_{avg} values can be counteracted by negative factors. We, therefore, generally set t_{avg} to 150 ms. Improving the signal-to-noise ratio to recover usable results for weak samples is then best achieved by stacking multiple repeated measurements [*Egli et al.*, 2010; *Heslop and Roberts*, 2012a] or by removing individual excessively noisy FORCs (or both). Repeated measurements required for stacking lengthens the measurement time to days (1 week in extreme cases). The automated nature of the measurement routine removes some of the associated inconvenience. Nevertheless, stacking of multiple measurements makes it convenient to consider measurement sequences that involve repeated measurements of only the most important parts of the FORC space and not, for example, the approach to B_{sat} where the mixed second derivative in equation (1) usually equals zero. Such measurement schemes will vary from sample to sample, but the potential reduction in measurement time produced is likely to make such schemes a target for future development. Just as it is important to specify the SF value used to calculate a FORC distribution when publishing results, it can be important to specify the t_{avg} value. This is particularly important for particle systems that undergo magnetic relaxation on the same (short) timescales as t_{avg}. In such cases, different FORC distributions can be obtained for the same sample if measured with different t_{avg} values [*Pike et al.*, 2001a]. Superparamagnetic (SP) particle systems with this behavior can be widely important (see section 7.3 below). While obtaining different FORC diagrams with different measurement parameters might seem alarming, the ability to resolve features associated with rapidly relaxing magnetic particle systems is also an advantage of rapid measurement times that can be exploited to understand SP systems [*Pike et al.*, 2001a].

The number of FORCs to be measured N is an important parameter because it dictates the time needed to complete a measurement sequence. Early studies were restricted by a MicroMag^{TM} software limitation that

prevented measurement of more than 99 FORCs [e.g., *Pike et al.*, 1999; *Roberts et al.*, 2000]. For many samples, this was adequate, but FORC diagrams that span a wide range of fields in $\{B_c, B_i\}$ space are often not adequately resolved with 99 FORCs (e.g., Figure 8b (by comparison with Figures 8c and 8d) in *Roberts et al.* [2000]). This limitation no longer applies, which makes it reasonable to ask: "what is the optimal number of FORCs to measure?" The answer is that this is always sample dependent. Covering a larger B_c range for FORC diagrams with rectangular aspect ratios will require more measurements compared to square FORC diagrams. This can be visualized in Figure 1f. The parameter that ultimately controls N is δB. *Egli et al.* [2010] showed that decreasing δB and, therefore, increasing N did not appreciably improve the resolution of features that were already well resolved with fewer FORCs. In contrast, to detect an absence of magnetostatic interactions in a FORC distribution requires resolving of a sharp central ridge at $B_i = 0$. *Egli et al.* [2010] showed that lower δB (and higher N) values produced an important improvement in resolution of the central ridge that would be excessively smoothed and inadequately resolved with fewer FORCs. In studies where resolving the central ridge is important, it is common for N to exceed 200. The key to selecting an appropriate number of FORCs is to ensure that features of interest are adequately resolved. When starting FORC analyses for a new set of samples, it is useful to survey the full $\{B_c, B_i\}$ space at low resolution to detect features of interest that can then be explored with higher-resolution measurements.

Finally, making good FORC measurements depends not only on the sample magnetization but also on the extent of hysteresis. That is, it is easier to make high-quality FORC measurements for SD than MD materials. This reflects the magnitude of the irreversible magnetization detected with FORC measurements [*Pike et al.*, 2001b]. Lower M_{rs}/M_s ratios for MD compared to SD materials means that the signal of interest compared to the total magnetization is weak, which decreases the signal-to-noise ratio. Calculation of the mixed second derivative in equation (1) amplifies measurement irregularities and gives rise to noisier FORC diagrams. The measures discussed above in relation to stacking and below in relation to optimizing technical considerations, therefore, become more important for MD compared to SD-dominated samples.

6.2. Technical Considerations for FORC Measurements

The two MicroMag^{TM} systems used for FORC measurements are the vibrating sample magnetometer (VSM) [*Foner*, 1959] and the alternating gradient magnetometer (AGM) [*Flanders*, 1991]. These instruments perform differently in terms of measurement sensitivity and environment, which makes it important to understand the conditions required to make high-quality measurements for both systems. The AGM is more sensitive than the VSM by about an order of magnitude, but it requires smaller samples (masses up to several hundred milligrams) than a VSM (masses up to several grams). Thus, the lower sensitivity of the VSM can be compensated for by measurement of larger samples (although many samples measured on a VSM are small, which reduces the benefit of this potential trade-off). In rock magnetic applications, it is usually preferable to measure a larger sample to avoid problems associated with potential inhomogeneity of small samples. This requirement generally makes use of a VSM preferable to an AGM.

The AGM operates within the range of audible frequencies; prior to measurement, the piezoelectric probe must be tuned to the resonant frequency of the springs that hold the probe in place. This means that the AGM is highly sensitive to acoustic noise (voices, doors closing, etc.). It is, therefore, highly desirable for the AGM to be located in a quiet space. In many laboratories, the AGM measurement space is enclosed within a padded box to assist with soundproofing (with a door for sample access; Figures 5o and 5p). Suspension of the piezoelectric probe on a set of springs (Figure 5l) also means that it is an effective seismometer. Thus, minimization of vibration and airflow (e.g., air conditioning) through the laboratory is required to make good measurements. Reduction of airflow is also aided by use of an acoustically padded box. Building vibrations are best minimized in ground floor or basement locations, away from busy streets, construction sites, elevators, or motions caused by tree roots on windy days. Temperature variations in the region of the sample can also affect measurements [*Jackson and Solheid*, 2010]. The most likely causes of temperature change are magnet heating or excessive cooling if chilled water is used to cool the magnet. A constant temperature environment is optimal. Temperature-related problems are most likely to occur during the first few minutes of measurement if there is a strong temperature gradient between a cool magnet and the sample. In this case, it is best to give time for the sample to reach thermal equilibrium, such as by measuring a hysteresis loop [*Jackson and Solheid*, 2010]. With either the AGM or VSM, significant nonlinear instrument drift, which often occurs as sudden jumps, can occur within 20 min of switching the system on. *Egli et al.* [2010] and *Egli*
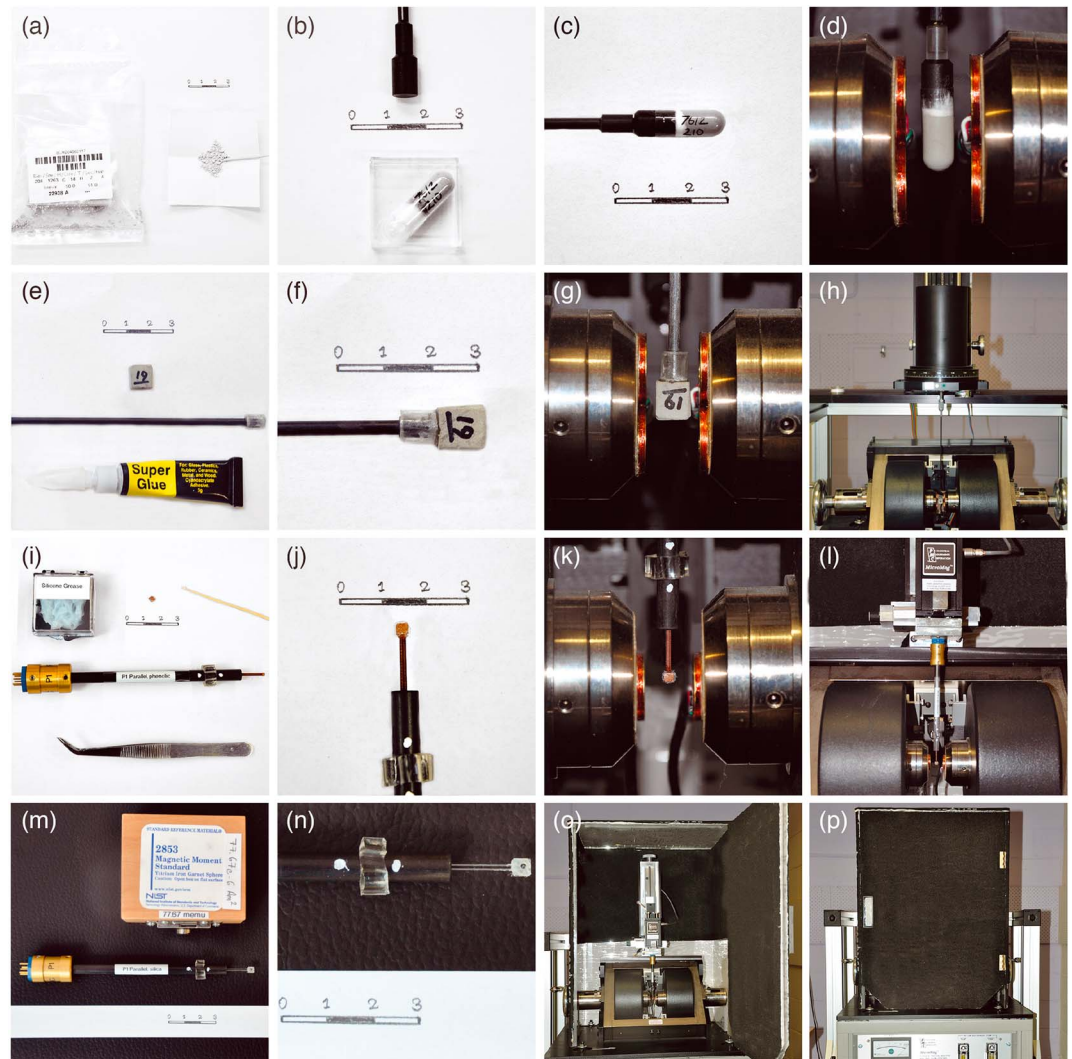
Figure 5. Sample preparation and measurement for typical sample types. (a) Preparation of loose sediment into (b) a pharmaceutical gel cap holder, where the top of the sample is packed with quartz wool. (c) The gel cap is slipped onto a plastic end piece, which is then screwed onto the VSM drive rod for measurement. (d) The drive rod is then placed into the vibrating head of the VSM, and the sample is lowered into, and centered within, the measurement region between the VSM pickup coils (see two sets of vertically mounted coils with copper windings on the face of the magnet pole pieces). (e, f) For lithified materials, cubic samples can be cut with a rock saw. Fixing the sample to a plastic end piece with superglue, and screwing it onto the VSM drive rod, ensures strong contact with the rod. (g) Close-up view of a centered cubic rock sample within the VSM measurement space. (h) More distant view of the VSM head, the drive rod, the mounted cubic rock sample, and the magnet. (i) Tools used to mount small samples onto a phenolic AGM probe. (j) Silicone grease is often used to hold the sample onto the glass square at the probe tip. (k) Close-up view of a centered sample within the AGM measurement space. (l) More distant view of the probe in measurement position (suspended with four springs from the AGM head). (m) More fragile quartz AGM probe with spherical yttrium iron garnet calibration sample. (n) Close-up of the calibration sample on the quartz probe. (o) More distant view of the mounted quartz probe in measurement position, within a box that restricts acoustic noise and air movement. (p) View of the sound-damping box, which is kept closed during AGM measurements. Scale bars in Figures 5a–5c, 5e, 5f, 5i, 5j, 5m and 5n are in centimeters.

[2013] recommend that dummy measurements should be made for the first 20 min until the electronics have warmed to steady state. FORC measurements are made over protracted periods of time, which means that slight temperature changes can affect the springs that support the AGM probe and change its resonant frequency, which can affect measurement quality. This aspect is difficult to resolve, especially for longer measurement runs. Despite these potential difficulties, much valuable work has been done with AGM systems. Control of the above aspects will contribute to improved measurements. The AGM is sometimes the
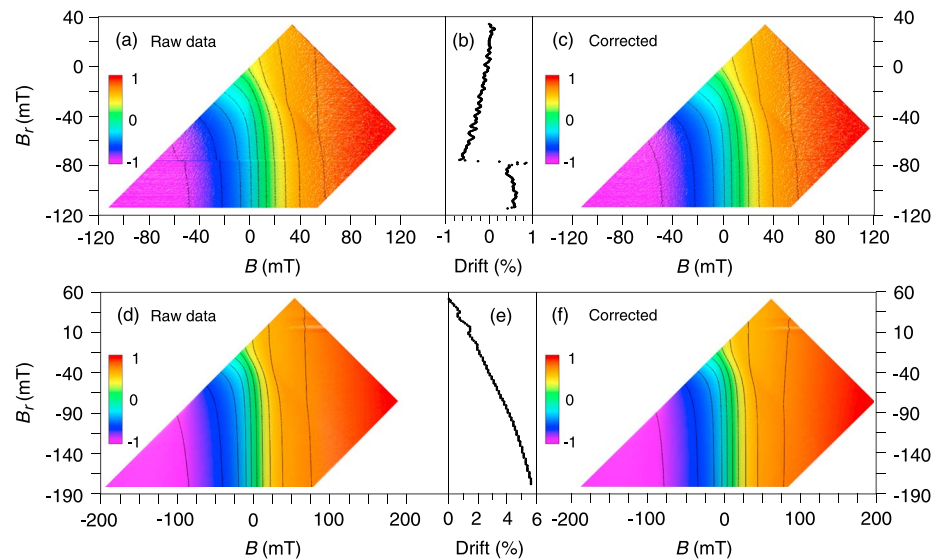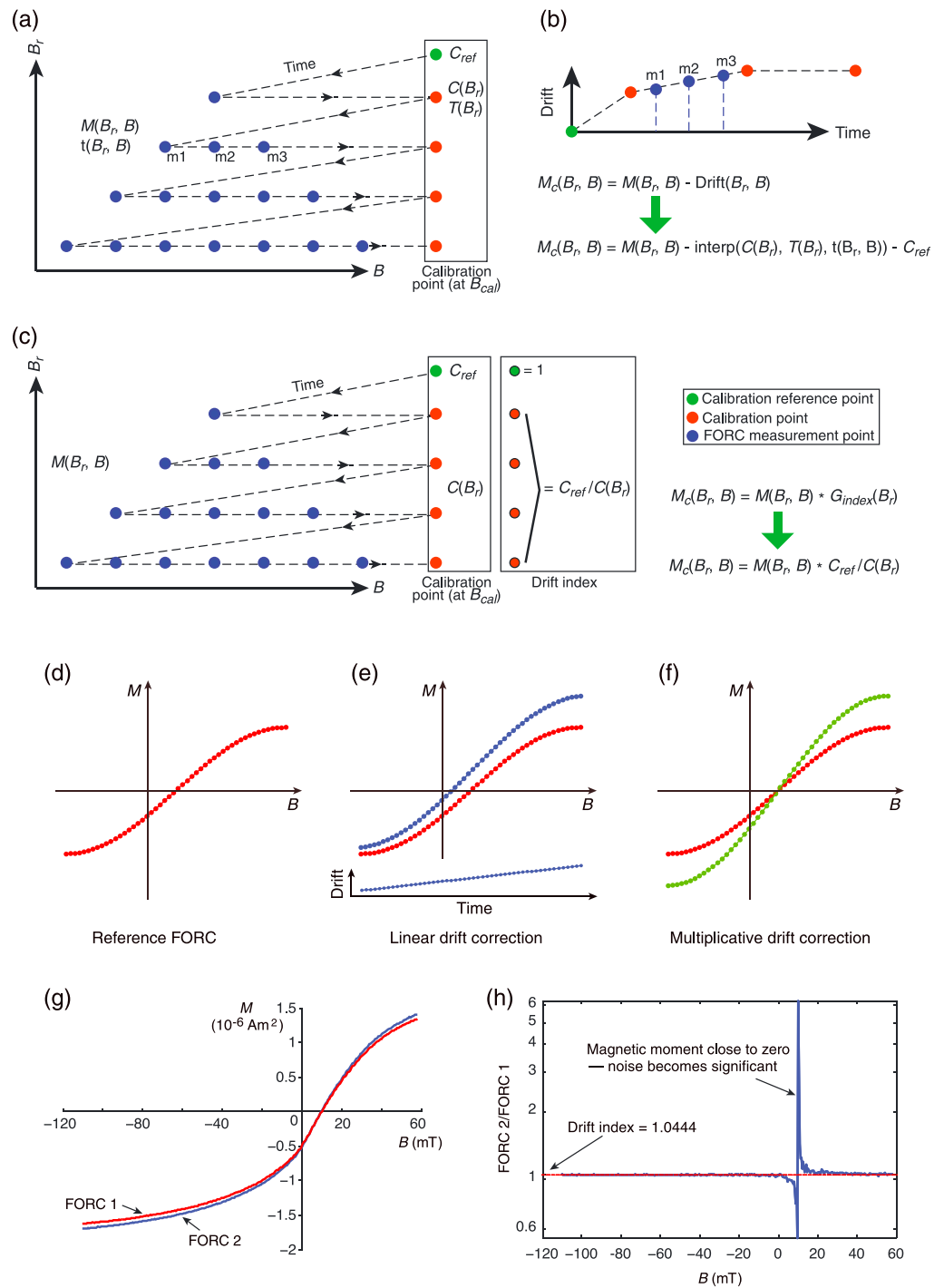
Figure 6. Illustration of drift correction for FORC measurements. (a, d) Normalized, contoured raw magnetization data in $\{B_r, B\}$ coordinates, with (b, e) percentage drift, determined from repeat measurements of B_{cal} before the start of each FORC measurement. A sudden impulsive drift event at $B_r \approx -75$ mT in Figures 6a and 6b can be readily removed by (c) drift correction. Apart from the impulse event, overall drift is reasonably steady (~1%) and can be corrected straightforwardly. For another sample, overall drift is larger (~6%), which can also be corrected straightforwardly (f) except for two relatively short-period oscillatory drift events between $B_r = 15$ and 30 mT in Figures 6d and 6e. Correction is most effective when drift is smooth.

only suitable instrument (e.g., for single crystal measurements [e.g., *Tarduno et al.*, 2006]), but generally, the VSM is a more stable platform from which to make FORC measurements. In contrast to the AGM, the VSM is insensitive to acoustic noise, vibration, and airflow. In cases where samples are large enough to compensate for its lower sensitivity, the VSM is an ideal instrument for FORC measurements.

Magnetometer measurement drift can occur on a range of timescales, both short and long. Drift involves spurious changes in measured signal strength and can occur during a 2 min hysteresis loop measurement and can be manifest, for example, as failure of the loop to close. The causes of drift are variable and include temperature change within the sample, displacement or reorientation of the sample during measurement, or slow changes in vibration drive instability, electronic drift, or thermal variation within the sensor [*Jackson and Solheid*, 2010]. Drift can occur smoothly or can be sharp and nonlinear (Figure 6); it can occur as a function of time or field. Drift is checked for within FORC measurements each time M is measured at the calibration field B_{cal} at the end of each FORC measurement. Sharp nonlinear drift can be corrected (Figures 6a–6c). Otherwise, drift is expected to be gradual (Figures 6b and 6e) and is corrected for by assuming a constant drift rate between successive measurements at B_{cal} (Figures 7a, 7b, and 7e). Thus, even though the overall drift throughout the FORC measurement sequence is usually nonlinear (Figures 6b and 6e), it is considered reasonable to treat drift as linear for the relatively short time intervals between successive measurements at B_{cal}. Short-term instabilities are more difficult to correct (e.g., between B_r values of 30 and 15 mT in Figures 6d–6f). If such instabilities affect only one or two consecutive FORCs, the FORCs concerned are best discarded [*Egli*, 2013]. Recent FORC calculation algorithms enable removal of individual FORCs that are affected by such problems, which avoids their overall damaging effect on the quality of calculated FORC diagrams [e.g., *Harrison and Feinberg*, 2008; *Heslop and Roberts*, 2012a; *Egli*, 2013].

Linear drift correction (Figures 7a, 7b, and 7e), which was used in all early FORC processing algorithms, does not correct properly for drift. Linear correction involves interpolating between successive calibration measurements of M at B_{cal} with respect to time (Figures 7a, 7b, and 7e). A reference FORC (Figure 7d), once corrected for linear drift, will be offset upward or downward with the slope of the FORC becoming progressively steeper or shallower from the beginning to the end of the FORC (Figure 7e; the direction of offset and slope will depend on the direction of drift). We propose a more appropriate drift correction similar to that proposed by *Egli* [2013], where drift correction is multiplicative rather than additive so that the slope varies about $B = 0$ (Figure 7f) rather than at B_r for each FORC (Figure 7e). The extent of the correction is

Figure 7. Illustration of linear and multiplicative drift corrections. (a) Time sequence of FORC measurements with repeated measurement at calibration point C (at B_{cal}) at the end of each FORC. (b) The time at each calibration measurement is calculated using the magnet slew rate, measurement pause time, and averaging time so that drift can be calculated for each magnetization measurement by linear interpolation. (c) Multiplicative drift correction is performed using the drift index, which is the ratio of the initial calibration measurement (C_{ref}) divided by the calibration measurement for each FORC ($C(B_r)$). Corrections are illustrated for (d) a FORC using (e) linear and (f) multiplicative drift corrections. With linear correction, the corrected FORC is shifted vertically in Figure 7e at B_r with a progressive change in slope along the FORC that depends on the direction of drift. By contrast, in Figure 7c, multiplicative drift correction involves a change in slope of the FORC about $B = 0$. (g) For two measurements of the same FORC, (h) the ratio of the two FORCs is 1.0444, which is the index by which FORC 1 needs to be multiplied to obtain FORC 2 (the magnetization becomes noisier close to $B = 0$). The drift index is constant in each case (red line in Figure 7h), which justifies use of a single value for correction.

ROBERTS ET AL. 569
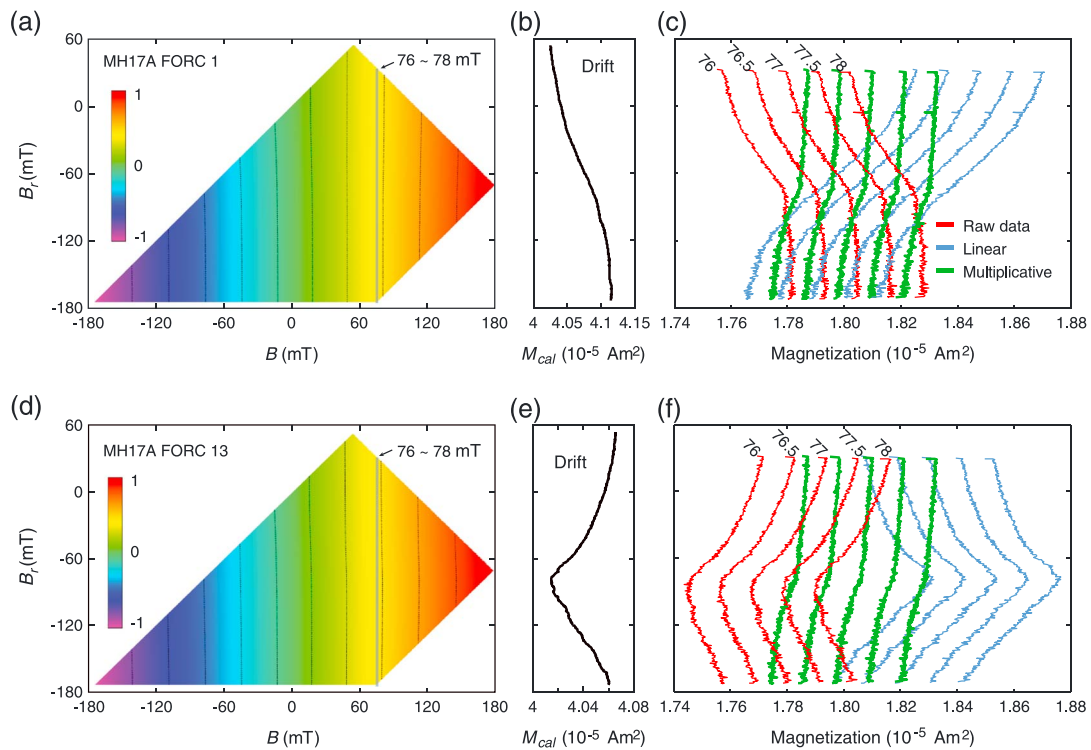
Figure 8. Illustration of the effects of linear and multiplicative drift corrections on FORC data. (a, d) Normalized magnetization with respect to B_r and B for two high-resolution FORC measurements of a dominantly paramagnetic sample with little hysteresis. (b, e) The drift pattern is different for two sets of measurements. (c, f) Raw magnetization data (red) for profiles at applied fields of 76, 76.5, 77, 77.5, and 78 mT reflect these different drift trends, as do the corrected data after conventional linear drift correction (blue). By contrast, multiplicative drift correction (green) provides a consistent set of corrected curves.

illustrated by taking the ratio of repeated measurements of a single FORC (FORC 2/FORC 1 in Figure 7g). In this case, the drift index is 1.0444 (Figure 7h), so that FORC 1 is multiplied by 1.0444 to obtain the drift-corrected FORC (Figure 7c). The drift index remains constant throughout the measured FORC (except near $M \approx 0$ where noise becomes significant; Figure 7h), which confirms that this drift affects the entire FORC. With this multiplicative drift correction, a measured FORC is compared with the reference FORC (Figure 7c) rather than at a repeated measurement of M at B_{cal}.

We compare the relative performance of the multiplicative drift correction with linear drift correction using a dominantly paramagnetic sample with a small ferrimagnetic component (Figure 8). Drift is different for two repeated measurements of the same sample (Figures 8a, 8b, 8d, and 8e). Raw data are plotted in Figures 8c and 8f (red) for all FORCs in the $B = 76$–78 mT range, along with corrected values for both types of correction. The shape of the overall drift curve (Figures 8b and 8e) has a strong influence on the linear drift correction (blue; Figures 8c and 8f), which produces markedly different corrected data for the two sets of measurements. In contrast, the multiplicative drift correction produces identical corrected data for the two data sets (green; Figures 8c and 8f), which demonstrates that this correction is more suitable than linear drift correction. Calculation of a FORC distribution involves smoothing across multiple FORCs (Figure 1e). The different drift corrections, therefore, do not necessarily produce major differences in FORC diagrams. Nevertheless, to achieve proper drift correction, the multiplicative drift correction should be adopted in FORC processing algorithms, as is the case in the variable smoothing FORC algorithm (VARIFORC) of *Egli* [2013].

When discussing measurement errors, it is useful to consider applied field errors associated with FORC measurements in addition to magnetization errors. Precise field control is achieved for each FORC by sweeping the magnet from B_{sat} to a point close to the next desired B_r value. This makes it easier for the magnetometer system to precisely control the magnet with a finer field step to the desired B_r value to start measuring the next FORC. This feature has been part of the FORC measurement protocol since *Pike et al.* [1999] and is evident as two closely spaced data points at the beginning of each FORC in Figure 1f. Most data
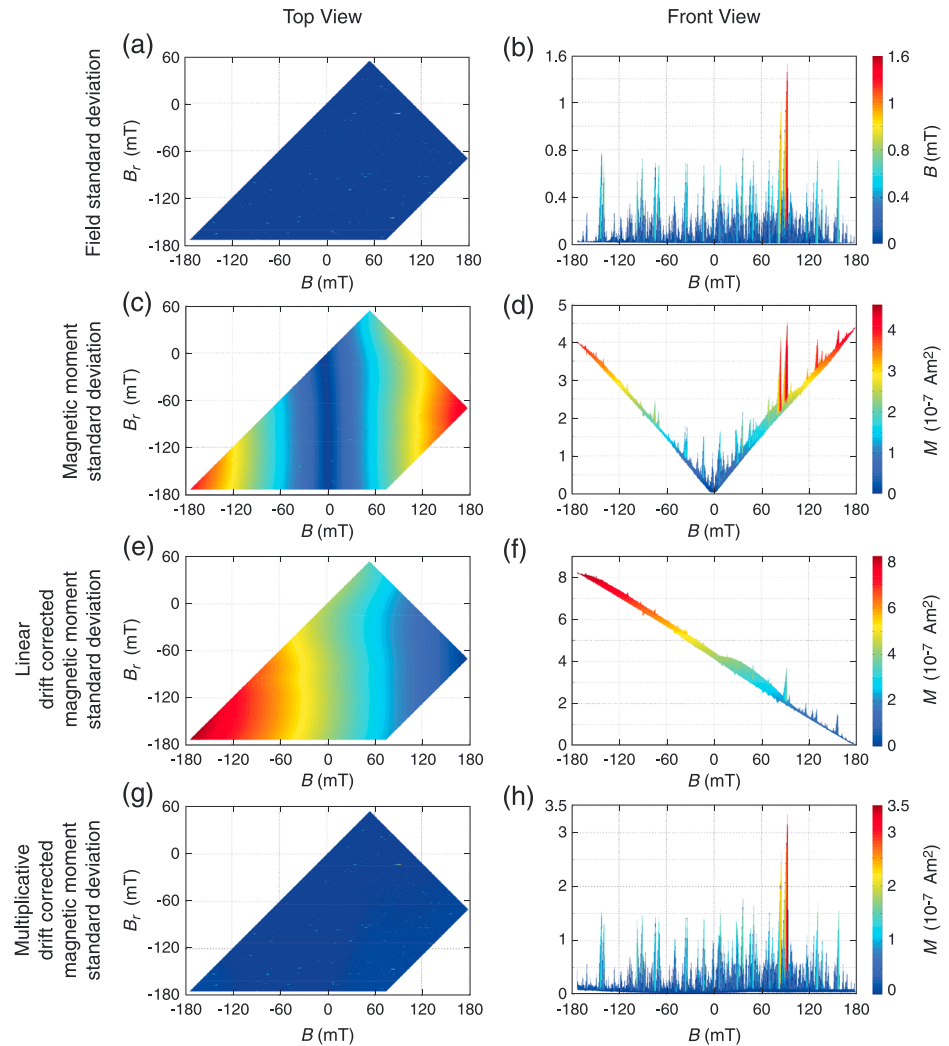
Figure 9. Illustration of magnetization and field noise in FORC measurements. Color maps of magnetization and field noise standard deviations in B_r versus B space (left-hand side) for 30 repeated high-resolution FORC measurements (498 FORCs each) alongside views of the standard deviation for all data with respect to B (right-hand side). Paired plots are for (a, b) standard deviation of B, (c, d) standard deviation of M, (e, f) standard deviation of M after conventional drift correction, and (g, h) standard deviation of M after multiplicative drift correction. The latter, Figure 9h, closely matches the standard deviation of B in Figure 9b, which suggests that multiplicative correction is the most appropriate.

processing algorithms remove this first measurement point. Nevertheless, as indicated by *Egli* [2013], field control is not absolutely precise; he attributed this to possible coupling between the electromagnet and measurement unit. We are unaware of previous documentation of the nature of errors in reaching the desired applied field. Here we provide the first documentation of field "noise" in FORC measurements (Figure 9). For 30 repeated high-resolution measurements (498 FORCs each), field control is imperfect, as indicated by nonzero standard deviations. Large spikes away from expected field values occur occasionally (Figures 9a and 9b); most standard deviations are <0.4 mT for this large data set (Figure 9b). The few major outliers are probably best dealt with by removing the FORCs in question. Standard deviations associated with repeated magnetization measurements are variable (Figures 9c and 9d), but the largest outliers correspond to major outliers in the applied field data (Figures 9b and 9d). When magnetizations are corrected using linear (Figures 9e and 9f) and multiplicative (Figures 9g and 9h) drift corrections, the multiplicative correction has standard deviations with the same pattern of variability and comparable magnitudes as the applied field standard deviations (Figures 9b and 9h). This confirms that the multiplicative correction is more appropriate than the linear drift correction and that field and magnetization noise are as important as each other. Field
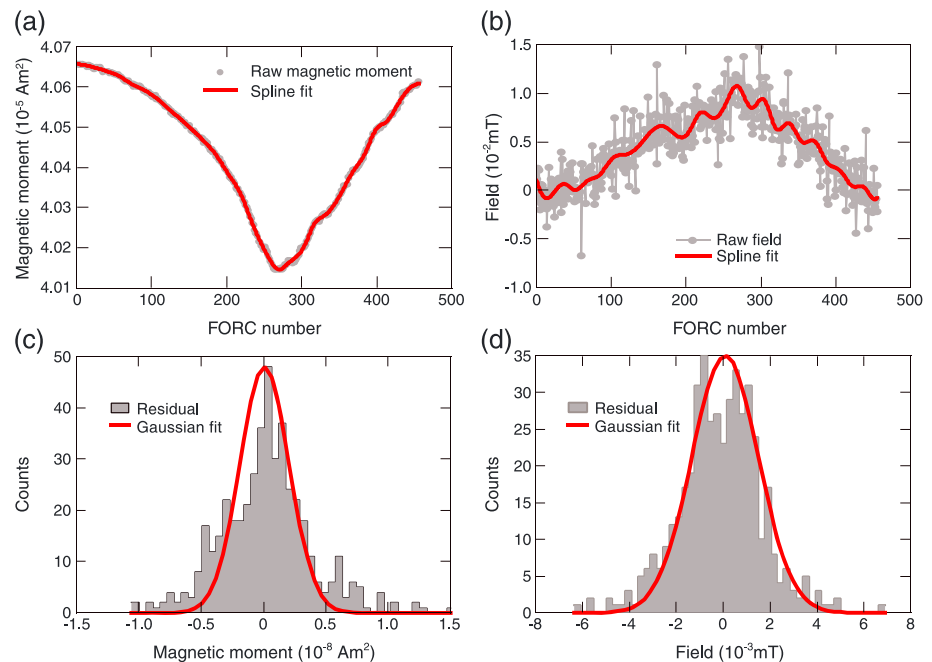
Figure 10. Illustration of the nature of magnetization and field noise in FORC measurements. (a, b) For a single set of high-resolution FORC measurements, noise is represented by the deviation of data (gray) away from a spline fit (red), with (c, d) residuals. Magnetic moment measurements in Figure 10a are from M measurements at B_{cal}, with applied field data at B_{cal} (the value of the first B_{cal} measurement was subtracted to indicate the extent of field drift). Residuals in Figures 10c and 10d have an approximately normal distribution, which means that Gaussian statistics can be used to treat noise [cf. *Heslop and Roberts*, 2012a].

noise, therefore, also deserves consideration in FORC analysis. After subtraction of raw data from spline fits through calibration measurements of M at B_{cal} (Figures 10a and 10b), residual magnetization and field noise have approximately Gaussian distributions (Figures 10c and 10d). This means that noise can be treated with standard Gaussian statistics [cf. *Heslop and Roberts*, 2012a; *Egli*, 2013].

6.3. Sample Preparation

Sample preparation is an important consideration for optimizing FORC measurements. There are too many sample preparation methods to provide an exhaustive treatment here. We outline some key strategies that, based on experience, provide better results than others.

When using an AGM, it is common to attach samples to the probe using silicon vacuum grease (Figures 5i, 5j, 5m, and 5n). This can work well for short measurement runs, but a sample can creep or slip on the probe surface during longer measurements. The probe response to the magnetic signal will then no longer be optimized and measurement quality will be degraded. Measurement quality can be significantly improved when using a water-soluble glue to secure the sample to the probe. When measurements are completed, samples can be liberated from the probe by holding it in water until the glue dissolves. The fragility of the fine quartz AGM probes can make this an expensive strategy if the user is careless or does not have steady hands; we bear no responsibility for breakages incurred. This strategy is better employed with the more robust phenolic probes (Figures 5i–5k), but breakages can still occur. The overall aim is to maximize contact between the probe and the sample so that their response remains the same throughout the measurement run.

Regularity of sample shape is preferable to avoid shape-related effects on measurements. Use of a cylindrical sample mold for loose sediment, which can be held together with water-soluble glue, can work well for AGM measurements. Rock chips are often used for hysteresis and FORC measurements. When using a VSM, we advocate cutting rock samples into cubic (1 cm^3) shapes (Figures 5e–5h). Internally threaded plastic end pieces can then be glued to the top surface of the cube (Figure 5f) using a strong, rapidly curing adhesive. Once cured (usually in minutes), the sample can be screwed onto the drive rod of the VSM (Figures 5f–5h).

This provides a strong contact with the VSM drive rod, it maximizes sample volume to make up for the lower sensitivity of a VSM compared to an AGM, and makes it easy to rotate and align the sample into an optimal position with respect to the VSM pickup coils (which are evident in close-up images in Figures 5d and 5g). Once measurements are complete, the plastic end piece can be snapped off from the surface of the rock sample and any remaining glue or rock can be scraped off with a scalpel. Loose sediment samples (Figure 5a) are more difficult to analyze than rock samples and are often packed into pharmaceutical gel caps (Figure 5b) that can be attached to the VSM drive rod with various techniques (Figures 5c and 5d). Bigger gel caps are preferable to maximize sample size. The user must seek to minimize movement of material within the gel cap because this will increase measurement noise and act against the goal of making high-quality measurements. For example, *Chen et al.* [2005] demonstrated an undesirable inflection in FORCs across $B = 0$ when the magnetization of mechanically unfixed particles can rotate from alignment with negative to positive fields. Likewise, use of pressure to pack more sediment into, for example, a pellet could increase magnetic interactions among particles. Such negative effects due to sample preparation have been illustrated by *Chen et al.* [2005]. Overall, optimal sample preparation for high-quality FORC measurements requires good contact between sample and probe for an AGM, maximizing sample size to increase signal-to-noise ratio for AGM and VSM, and secure fixing of samples to minimize incoherent vibration of material within a sample for a VSM.

6.4. Statistical Significance

Statistical significance is not considered widely in rock magnetism, yet it is fundamentally important for FORC measurements where noise is often large and is amplified by calculation of the mixed second derivative in equation (1). Statistical significance is also important when making quantitative rock magnetic interpretations. It is, therefore, important to be able to assign a level of statistical significance to a FORC feature of interest. *Heslop and Roberts* [2012a] demonstrated how significance levels can be calculated for FORC distributions; FORC diagrams in this paper (where we could reprocess the data) have the 0.05 significance level plotted, as indicated by a bold black line (e.g., Figures 11a and 11d). Profiles of coercivity or interaction field distributions are also often reported through different parts of a FORC diagram. The method of *Heslop and Roberts* [2012a] enables calculation of confidence intervals for such profiles (Figure 11), which provides a further check on interpretational limitations. For example, for FORC diagrams that contain a central ridge signature that is not ideally defined because of measurement noise (Figure 11a), the use of 95% confidence intervals suggests that it is not meaningful to make interpretations concerning the high coercivity part of the distribution beyond ~85 mT. Nevertheless, plotting a series of coercivity distributions through the central ridge signature for three pelagic carbonate samples [*Roberts et al.*, 2013] demonstrates that the central ridges contain contributions from different populations of noninteracting SD magnetite particles, including mixtures of biogenic hard and soft components [cf. *Egli*, 2004]. *Heslop et al.* [2014] described procedures for extracting meaningful environmental data from central ridge signatures. Likewise, a profile of the interaction field distribution (Figure 11c) demonstrates the presence of the sharp central ridge signature; it has finite rather than zero width because of the finite spacing between successive measurements and because of smoothing (in this case, SF = 5). In contrast, for a sample containing strongly interacting stable SD greigite particles (Figure 11d), the coercivity distribution has higher coercivities with a Gaussian rather than a skewed profile (Figure 11e). The interaction field distribution also has a Gaussian form and is shifted below the $B_i = 0$ axis (Figure 11f). Profiles of the type shown in Figure 11 can be used for quantitative interpretation and comparison of FORC distributions. It is only meaningful to compare profiles through different FORC distributions [e.g., *Muxworthy and Dunlop*, 2002; *Carvallo et al.*, 2006a; *Rowan and Roberts*, 2006; *Geiss et al.*, 2008; *Roberts et al.*, 2011a] when using identical SF and δB values. Such comparisons depend on the noise level of the noisiest sample rather than the best or average sample.

Through appropriate recognition of statistically constrained limits to interpretation, it is possible to adapt measurement protocols. For example, the magnetic signal in some samples can be so weak that stacking of multiple measurements [*Egli et al.*, 2010; *Heslop and Roberts*, 2012a] is required to enable adequate identification of signals of interest (where noise is reduced as the square root of the number of measurements if noise has a Gaussian distribution (Figures 10c and 10d)). Calculation of statistical significance and confidence intervals in such cases can help to identify the number of times a measurement needs to be stacked to obtain results within a prescribed confidence interval. The approaches described by *Heslop and Roberts* [2012a] can be built into any algorithm used to calculate FORC distributions, as discussed in section 6.5. The variable
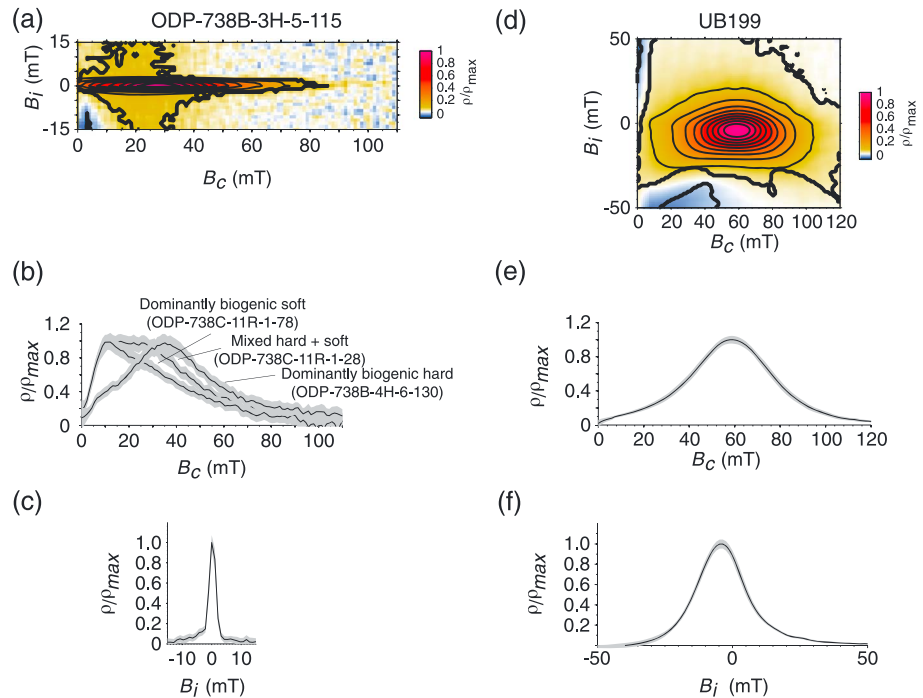
Figure 11. Statistical significance levels for FORC diagrams and confidence intervals for profiles through FORC distributions. (a) Noisy FORC diagram for a pelagic carbonate sample with a strong central ridge signature [*Roberts et al.*, 2011a]. The 0.05 significance level is indicated by a thick solid black line (and throughout this paper). For coercivity profiles along the central ridge for three pelagic carbonate samples, relatively broad 95% confidence intervals limit interpretation beyond ~85 mT. Regardless, the coercivity profiles are statistically distinct, which indicates that the central ridge signatures are due to variable mixtures of (b) biogenic soft and hard magnetite [*Roberts et al.*, 2013; *Heslop et al.*, 2014]. The central ridge signature is the strongest feature in Figure 11a, which gives rise to (c) a sharply peaked, clearly defined (Lorentzian) interaction field distribution, as indicated by the narrow 95% confidence intervals. Contrasting results for (d) strongly interacting stable SD greigite (sample from *Roberts and Turner* [1993]). The (e) coercivity and (f) interaction field distributions both have a broad Gaussian form, with the peak of the interaction field distribution displaced to negative B_i values. The signal-to-noise ratio is higher for this sample, therefore, the 95% confidence intervals are narrow.

smoothing approach (VARIFORC) [*Egli*, 2013] produces statistically significant results over a much larger part of the FORC diagram than conventional processing algorithms.

6.5. Calculation Algorithms

Two classes of algorithm have been produced (so far) for calculating FORC distributions. The first involves different philosophies for resolving the challenge of calculating the FORC distribution along the B_i axis. The second deals with different approaches to suppressing noise and smoothing of FORC distributions. We deal with these two classes of algorithm in turn. The two sets of philosophies are not mutually exclusive and have been used in different combinations in popular algorithms for calculating FORC distributions.

6.5.1. Calculating the FORC Distribution Along the B_i Axis

A FORC distribution can only be rigorously calculated to the limits of a FORC diagram if the number of measurements on the local grid (Figure 1f) extends beyond the limits of the diagram by SF. This is achieved by measuring extra data points for the upper, lower, and right-hand bounds of the FORC diagram (see gridded points in Figure 1f), but it is impossible along the B_i axis. Four approaches have been developed to deal with this problem (Figures 12a–12d). The first is to truncate the FORC diagram at the left-hand limit at which the polynomial surface can be rigorously calculated (Figures 12a and 12f) [e.g., *Kruiver et al.*, 2003]. This leaves a gap of SF × δB between the calculated FORC distribution and the B_i axis. While this approach is mathematically rigorous, its principal limitation is that many features of greatest interest occur within the region closest to the B_i axis (see section 7 below). This problem was recognized by *Pike et al.* [1999] who relaxed the calculation of $\rho(B_r, B)$ by reducing smoothing near the B_i axis (Figures 12b and 12g). This approach has been referred to as the "relaxed fit" method [*Muxworthy and Roberts*, 2007]. Relaxation distorts the FORC
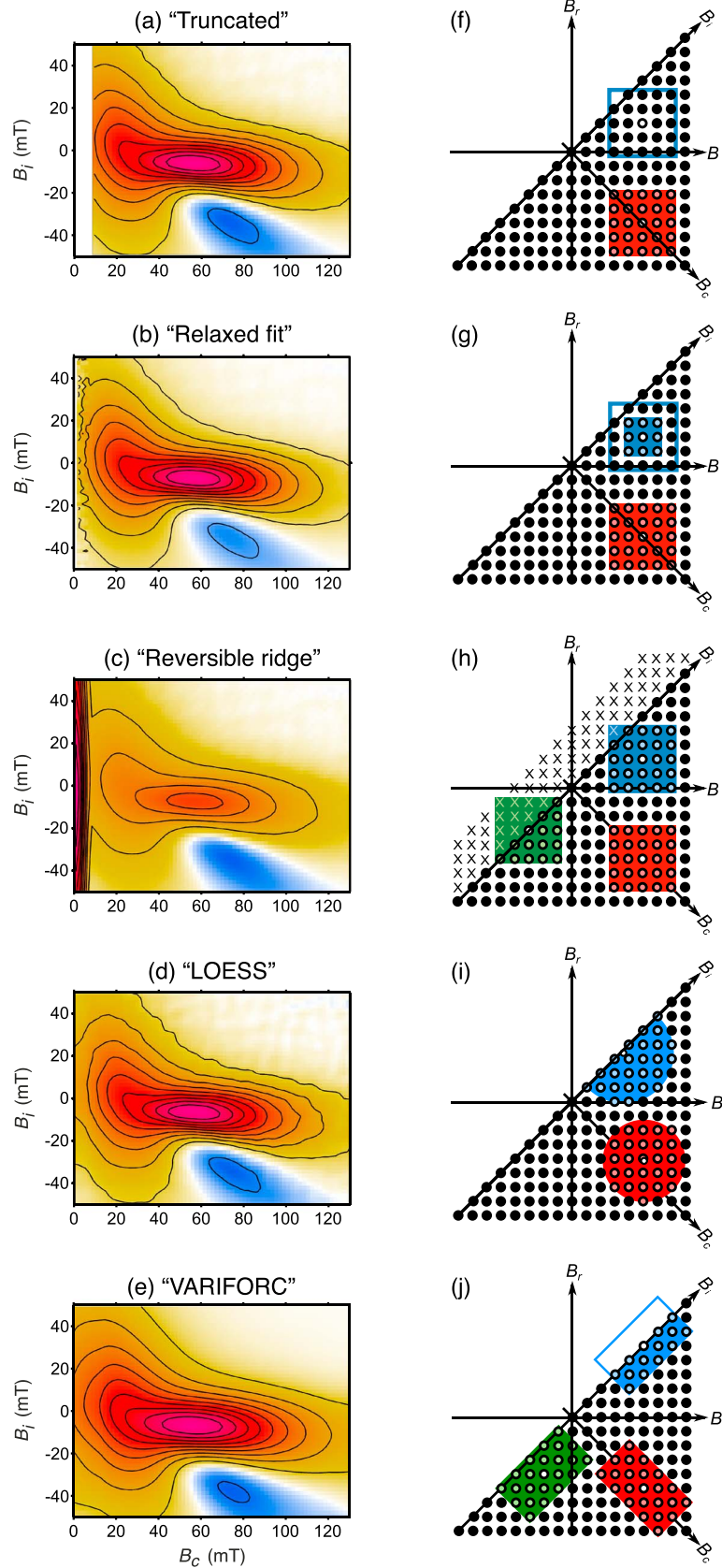
Figure 12

distribution, which can be misleading if the field increment, δB, is too large, but it at least enables detection of signals due to low-coercivity magnetic components. This key advantage is generally taken to outweigh the argument for truncation. *Pike* [2003] developed a third approach to avoid the deficiencies of the first two approaches by using the reversible magnetization component to extrapolate measured FORCs beyond $B_r < 0$. This enables rigorous calculation of $\rho(B_r, B)$ to the B_i axis (Figures 12c and 12h). It creates a peak, or ridge, at $B_c = 0$ (Figure 12c); this method has been referred to as the "reversible ridge" method [*Pike*, 2003]. This approach, while rigorous, can also cause low-coercivity components of interest to be obscured because the reversible ridge can swamp signals from the irreversible magnetization component that is of greater interest [e.g., *Chang et al.*, 2007]. This is not the case in Figure 12c, although the magnitude of the main FORC distribution is subdued with respect to the reversible ridge, which means that the FORC distribution is less well resolved than for other calculation methods (Figures 12a–12e). A fourth approach is the locally weighted regression (LOESS—LOcal regrESSion) method [*Harrison and Feinberg*, 2008]. Instead of assigning a uniform weight to points within the $(2SF + 1)^2$ grid (Figures 12f, 12g, and 12h), the LOESS method assigns a higher weight to data points closer to the point being evaluated (Figure 12i). These data points, therefore, have a greater effect on the polynomial fit. This approach does not require a regular grid of data points, which means that $\rho(B_r, B)$ can be calculated rigorously along the B_i axis with smoothing using a constant number of data points. Of the four approaches discussed, weighted regression smoothing, following *Harrison and Feinberg* [2008], is now used most commonly (including within VARIFORC; Figure 12j) because it enables rigorous calculation of $\rho(B_r, B)$ along the B_i axis without significant distortion of the FORC distribution. Nevertheless, all four approaches remain in use and all are compatible with those outlined below for noise suppression in FORC diagrams.

6.5.2. Noise Suppression

As discussed above, the best way to minimize noise in FORC diagrams is to make the best possible measurements. Many strategies, including stacking of measurements, can be employed to improve the signal-to-noise ratio. When all reasonable steps have been taken to obtain the best possible measurements, selection of an appropriate value of the smoothing factor, SF, in the FORC algorithm becomes the principal means by which noise suppression is achieved.

Roberts et al. [2000] illustrated how increasing smoothing simultaneously reduces noise and causes loss of signal; a similar illustration is provided in Figure 13 for stable SD samples, but with contrasting signal-to-noise ratios. An important question that arises is "what is the optimal SF at which noise is suppressed without causing further loss of signal?" It is preferable to assess this question quantitatively rather than by subjective user assignment of SF. *Heslop and Muxworthy* [2005] assessed signal-to-noise ratios in FORC data using spatial autocorrelation to examine residuals between observed and fitted $M(B_r, B)$ values to determine the optimal smoothing that removes substantial noise and avoids significant changes to the shape of the FORC distribution. While this approach is useful, it has not been adopted widely in FORC algorithms. In contrast, the LOESS approach of *Harrison and Feinberg* [2008] does not require a regular grid of data points, which enables excessively noisy individual FORCs to be removed from consideration. Noninteger SF values can also be assigned, which allows finer control on the degree of smoothing and automated control of optimal smoothing [*Harrison and Feinberg*, 2008].

Optimal smoothing is inherently difficult for samples that contain both a strong localized FORC contribution and weaker signals that are more widely distributed across the FORC space, especially when both sets of

Figure 12. Illustration of different methods for calculating a FORC distribution. (a, f) A truncated FORC diagram with no extrapolation onto the B_i axis. $\rho(B_r, B)$ cannot be calculated rigorously to the B_i axis with a conventional square grid, therefore, the grid in the blue box in Figure 12f is incomplete, and the region $SF \times \delta B$ closest to the B_i axis is left blank. (b, g) A relaxed fit FORC diagram where the smoothing algorithm is relaxed for the grid points with no data in the blue area in Figure 12g so that $\rho(B_r, B)$ is distorted in the region that is blanked out in Figure 12a, as evident in the noisier contours near the B_i axis. The advantage of relaxing the fit is that many important magnetization processes produce a FORC response in this region. (c, h) A reversible ridge FORC diagram (following *Pike* [2003]) in which $\rho(B_r, B)$ is calculated by extending FORCs into negative B_c space (crosses in Figure 12h) using the magnetization-extended method [see *Egli et al.*, 2010]. (d, i) FORC diagram calculated using locally weighted regression (LOESS) following *Harrison and Feinberg* [2008]. (e, j) FORC diagram calculated using the variable smoothing (VARIFORC) algorithm of *Egli* [2013]. Different vertical (green box) and horizontal (red box) smoothing can be achieved in Figure 12j to produce a smoother final FORC diagram in Figure 12e than with other methods in Figures 12a–12d. Use of locally weighted regression [*Harrison and Feinberg*, 2008] within the boxes in Figure 12j enables robust calculation of the FORC distribution up to the B_i axis (blue box).
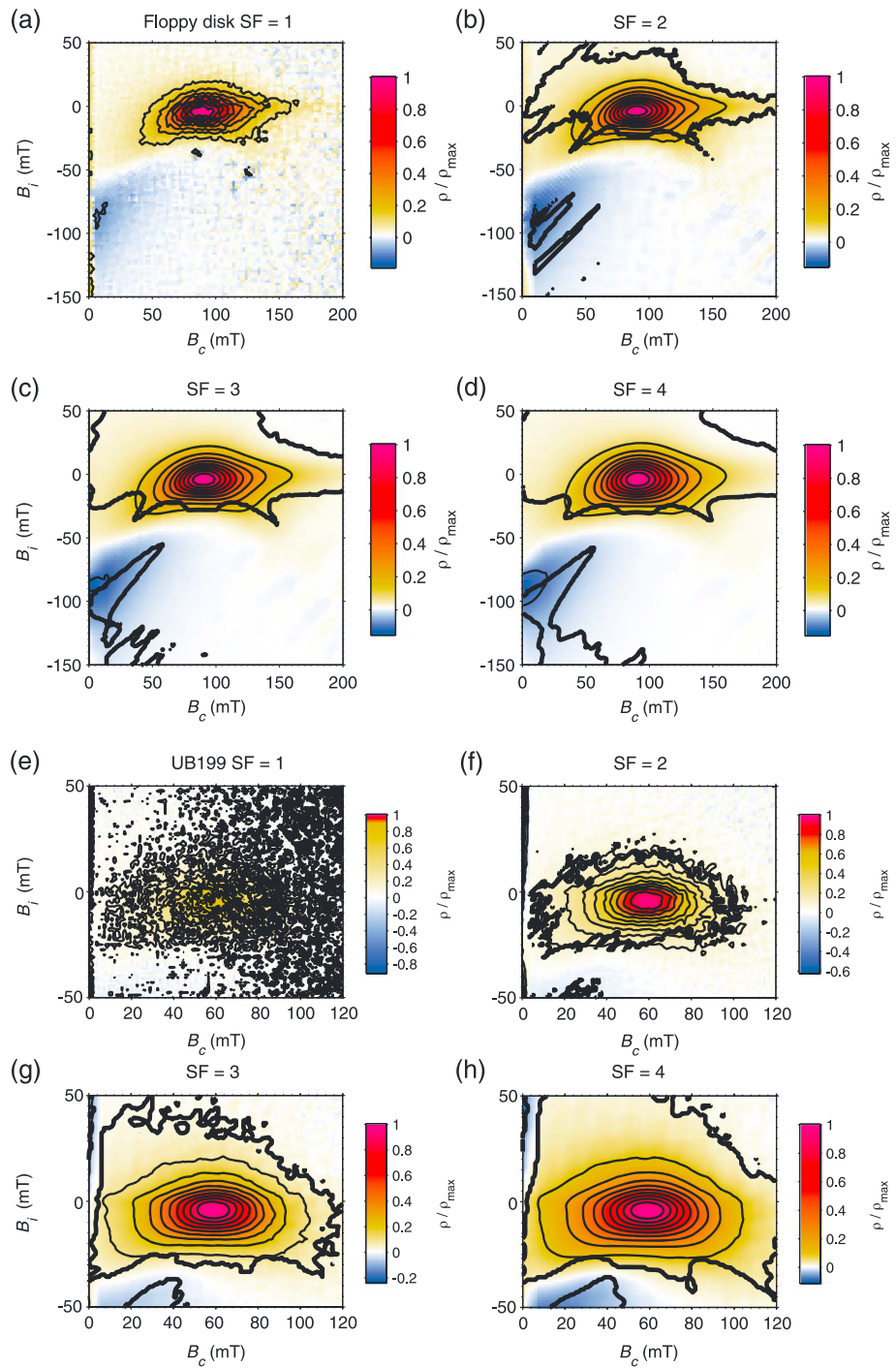
Figure 13. Illustration of smoothing in FORC diagrams for two samples with stable SD particles but with relatively higher and lower signal-to-noise ratios, respectively. SF values of (a) 1, (b) 2, (c) 3, and (d) 4 are illustrated for a floppy recording disk. SF values of (e) 1, (f) 2, (g) 3, and (h) 4 are illustrated for a sedimentary greigite sample [from *Roberts and Turner*, 1993]. The 0.05 significance level [*Heslop and Roberts*, 2012a] is shown for all FORC diagrams except for SF = 1, where there are insufficient degrees of freedom to allow its calculation.

features are of interest. Conventional approaches to noise suppression, as outlined above, encounter difficulties when seeking to adequately resolve both contributions. *Egli* [2013] tackled this problem by developing a variable smoothing procedure (VARIFORC). *Egli* [2013] used weighted regression, following *Harrison and Feinberg* [2008], but used data on rectangular grids the dimensions of which vary according to

the resolution required for different parts of the FORC diagram (Figure 12j). Depending on the features within a FORC diagram, variable smoothing can be applied horizontally (useful for isolating central ridge features; red in Figure 12j) or vertically (useful for isolating vertical ridges; green in Figure 12j) or in both directions. Of the available algorithms, VARIFORC appears to deal best with the competing requirements of noise suppression and maximizing resolution, as is evident when comparing the FORC diagrams in Figures 12a–12e. However, smoothing will progressively increase toward the outer limits of a FORC diagram (the extent depends on λ, the parameter used to control the rate of SF increase), which results in smoothing above levels normally considered acceptable for conventional FORC processing. This type of data processing can cause artifact horizontal and vertical ridges when nonoptimal λ values are used [e.g., *de Groot et al.*, 2014]. Throughout this paper, we use conventional smoothing with LOESS processing (Figure 12i). With use of appropriate λ values, much of the noise in the outer parts of these FORC diagrams could be removed by variable smoothing. However, we have used conventional smoothing to retain a uniform style consistent with that of the many older FORC diagrams presented in this paper.

Several FORC algorithms are used widely and employ different calculation philosophies and approaches to noise suppression, as discussed above. These algorithms include the original Mathematica code of *Pike et al.* [1999], the FORCobello code of *Winklhofer and Zimanyi* [2006], which was modified and renamed UNIFORC by *Egli et al.* [2010], the FORCIT code of *Acton et al.* [2007a], the FORCinel code of *Harrison and Feinberg* [2008], the FORCme code of *Heslop and Roberts* [2012a], and the VARIFORC code of *Egli* [2013]. Weighted regression smoothing [*Harrison and Feinberg*, 2008] is now widely used, and the VARIFORC approach of *Egli* [2013] can also be used as an option within other data processing packages. Attempts to deal with noise suppression, minimization of smoothing, maximization of resolution, a greater appreciation of the need to assess statistical significance, and the high level of recent activity associated with improving FORC processing algorithms suggest that opportunities for improving FORC data analysis have not been exhausted and that future improvements are likely.

7. Interpretational Framework for FORC Diagrams

The classic Preisach-Néel model [*Preisach*, 1935; *Néel*, 1954], as outlined in section 5, provides a framework for interpreting FORC diagrams. This framework has been extensively tested in two principal ways: (i) through measurement of well-constrained synthetic and natural samples and (ii) through numerical modeling of Stoner-Wohlfarth particles and micromagnetic modeling. Results of these efforts are summarized below for different types of magnetic behavior, including SD (with and without magnetostatic interactions), SP, vortex, pseudosingle domain (PSD), and MD behavior. Collectively, these constraints provide a robust interpretational framework for FORC diagrams from geological and industrially relevant synthetic materials.

### 7.1. Noninteracting Single Domain Behavior

SD behavior in FORC diagrams can be well understood using the phenomenological Preisach-Néel model [*Preisach*, 1935; *Néel*, 1954]. As illustrated in Figure 3, FORC diagrams for SD particle systems can be interpreted straightforwardly as representing coercivity and interaction field distributions along the horizontal and vertical axes, respectively [e.g., *Pike et al.*, 1999; *Roberts et al.*, 2000; *Muxworthy and Williams*, 2005; *Egli*, 2006; *Winklhofer and Zimanyi*, 2006; *Dubrota and Stancu*, 2013]. Even with the more complex and realistic representation involving Stoner-Wohlfarth particles [*Stoner and Wohlfarth*, 1948] illustrated in Figure 4, SD particle systems can be represented by a dominant distribution with closed contours centered at the switching field mode for the particle assemblage and a subsidiary negative peak [*Muxworthy et al.*, 2004; *Newell*, 2005] near the lower B_i axis at a 45° angle below the peak on the $B_i = 0$ axis (Figures 13a–13d). Thus, for geological samples that contain noninteracting SD particles, including a volcanic tuff (Figure 14a) [*Schlinger et al.*, 1988; *Rosenbaum*, 1993; *Till et al.*, 2011] and sediment that contains magnetite magnetofossils (the inorganic remains of magnetotactic bacteria) (Figure 14b), FORC diagrams contain a ridge-like distribution along the B_c axis with no vertical spread. *Pike et al.* [1999] confirmed with models of Stoner-Wohlfarth particles that noninteracting SD behavior is manifest as a central ridge [cf. *Egli et al.*, 2010] on FORC diagrams (Figure 14c). The spread of a FORC distribution along the B_c axis represents the coercivity distribution of the magnetic particle assemblage. The origin of the negative region along the lower B_i axis [*Newell*, 2005] is described in section 5 and is illustrated in Figures 13a–13d and 14b. Many FORC diagrams are truncated so that this negative region does not appear (as in Figures 14a, 14c, and 14d).
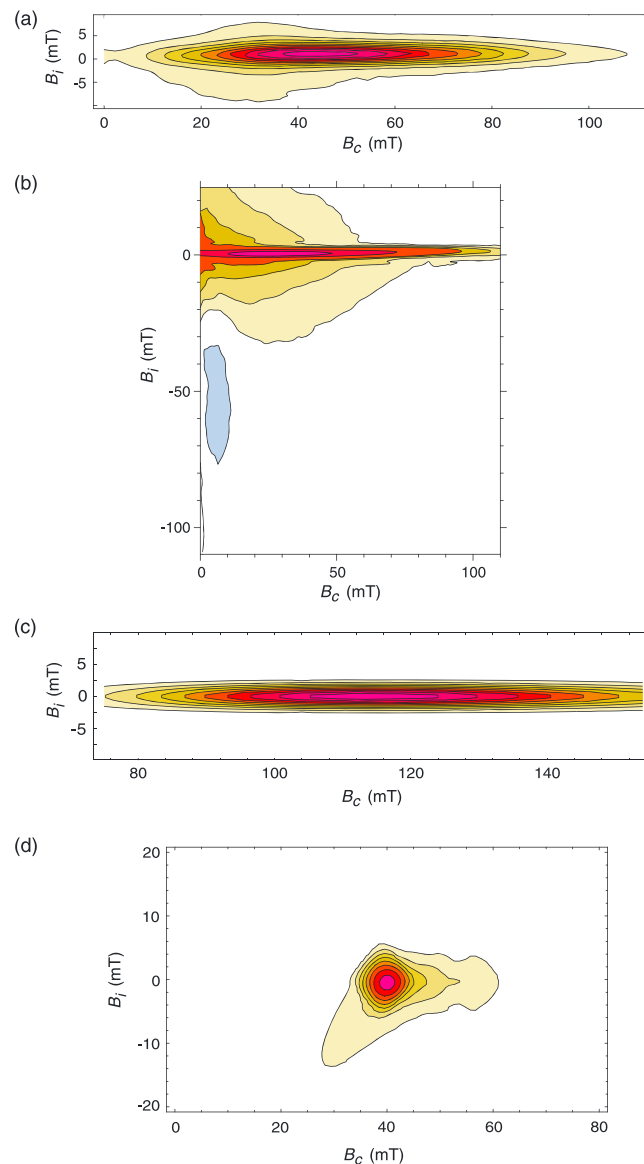
Figure 14. FORC diagrams for magnetostatically noninteracting SD particle systems. (a) FORC diagram for sample CS911 from the Tiva Canyon Tuff, Nevada [from *Roberts et al.*, 2000]. The tight distribution of contours along the $B_i = 0$ axis reflects the noninteracting nature of the magnetic particle assemblage, while the distribution along the B_c axis reflects its coercivity distribution. (b) High-resolution FORC diagram for a dominantly noninteracting SD assemblage in magnetotactic bacteria [after *Roberts et al.*, 2012]. The diagram is dominated by a strong "central ridge" feature [*Egli et al.*, 2010], a weaker negative region near the B_i axis, and a broader positive distribution due to detrital PSD particles. (c) Numerical model results for a noninteracting SD particle system with lognormal coercivity distribution [after *Pike et al.*, 1999]. (d) Micromagnetic model results for isolated SD particles based on averaging 100 FORC diagrams from randomly oriented, isolated, elongated SD grains with constant particle size (45 × 30 × 30 nm) [after *Carvallo et al.*, 2003].

The fact that FORC diagrams for magnetofossil-bearing samples (Figure 14b) reflect noninteracting SD behavior requires explanation. Magnetosomes produced by magnetotactic bacteria align into chain structures that result from strong magnetic interactions between consecutive particles [e.g., *Muxworthy and Williams*, 2009]. Magnetic flux linking between magnetosome particles gives an intact chain a strong magnetic anisotropy [*Dunin-Borkowski et al.*, 1998]. Intact magnetosome chains, therefore, effectively behave as isolated elongated SD particles with strong magnetic moment, with only two stable magnetization states (positive and negative saturation) [*Penninga et al.*, 1995; *Hanzlik et al.*, 2002], as expected for ideal elongated SD particles [*Jacobs and Bean*, 1955]. Thus, although the individual magnetic particles interact strongly, the net magnetic behavior is that of an isolated elongated SD particle, as exemplified in FORC diagrams [*Egli et al.*, 2010] (Figure 14b). Magnetostatic interactions among different magnetosome chains are negligible [e.g., *Moskowitz et al.*, 1993], so that FORC diagrams for recently deceased magnetotactic bacteria are dominated by a central ridge [e.g., *Pan et al.*, 2005; *Chen et al.*, 2007; *Fischer et al.*, 2008; *Carvallo et al.*, 2009; *Li et al.*, 2009; *Jovane et al.*, 2012; *Roberts et al.*, 2012], which indicates the presence of noninteracting SD particles [*Pike et al.*, 1999; *Roberts et al.*, 2000; *Egli et al.*, 2010]. Increased measurement of high-resolution FORC diagrams and identification of central ridge signatures [*Egli et al.*, 2010] have led to a boom in identification of magnetofossils in sediments that is revolutionizing our understanding of sedimentary magnetizations in the geological record [e.g., *Yamazaki*, 2008, 2009, 2012; *Abrajevitch and Kodama*, 2009; *Kind et al.*, 2011; *Roberts et al.*, 2011a, 2012, 2013; *Larrasoaña et al.*, 2012].

Micromagnetic modeling of isolated SD particles confirms the interpretive framework outlined above for FORC diagrams [*Carvallo et al.*, 2003; *Muxworthy et al.*, 2004]. As shown in Figure 14d, averaging of 100 FORC diagrams from randomly oriented (with respect to the applied field direction), isolated, elongated SD grains
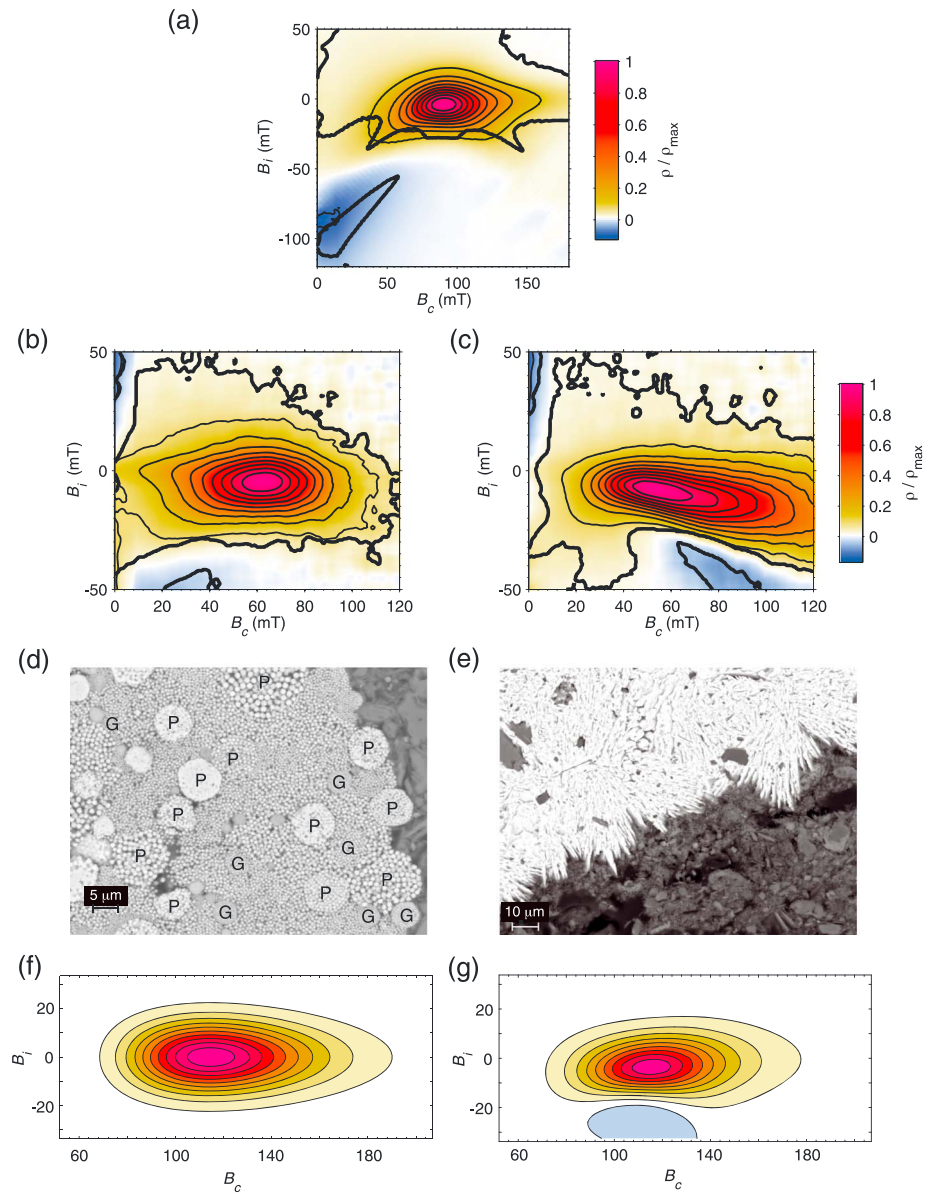
Figure 15. FORC diagrams for magnetostatically interacting SD particle systems. (a) FORC diagram for a floppy disk with closely packed SD particles (SF = 3). FORC diagrams for strongly interacting (b) greigite (V10) and (c) pyrrhotite (V14) samples from Vrica, Italy (both SF = 5), with (d, e) corresponding scanning electron microscope images [from *Roberts et al.*, 2010]. In Figure 15d, representative aggregates of G = greigite and P = pyrite are labeled. The greigite particles in Figure 15d are equant cubo-octohedra, while the pyrrhotite particles in Figure 15e are platy; touching or interlocking particles are responsible for the strong interactions. Modeled FORC diagrams for interacting SD particle systems for (f) a basic *Preisach* [1935], and (g) a moving *Preisach* [1935] model with a positive mean interaction field [after *Pike et al.*, 1999].

with constant particle size (45 × 30 × 30 nm) gives rise to a FORC diagram with a peak that is consistent with that obtained for Stoner-Wohlfarth particles (Figure 4). The lack of magnetostatic interactions gives rise to a point FORC distribution (with minor vertical spreading resulting from smoothing (SF = 3)).

7.2. Single Domain Behavior With Magnetostatic Interactions

As discussed above, magnetostatic interactions are expected to give rise to vertical spreading of a FORC distribution (Figure 3f). This can be visualized for thermally stable SD particle systems using samples with known close spacing of particles, such as industrially produced magnetic recording media (Figure 15a) or iron sulfide-bearing samples that contain diagenetic greigite (Figure 15b) or pyrrhotite (Figure 15c). Diagenetic

greigite generally grows with close packing of discrete particles [e.g., *Rowan and Roberts*, 2006] (Figure 15d) and monoclinic pyrrhotite grows as interlocking plates [e.g., *Weaver et al.*, 2002; *Roberts et al.*, 2010] (Figure 15e). FORC diagrams for these strongly magnetically interacting samples have large vertical spread and contain a dominant SD peak centered at the modal coercivity of the respective particle assemblages (Figures 15a–15c) and a subsidiary negative peak near the lower B_i axis at 45° below the peak on the $B_i = 0$ axis (Figure 15a). In addition, the pyrrhotite sample gives rise to a negative peak below the main positive peak (Figure 15c).

Experimentally determined FORC diagrams for magnetostatically interacting SD particle systems have been replicated using a range of modeling approaches. A FORC diagram calculated using the basic *Preisach* [1935] model for magnetostatically interacting Stoner-Wohlfarth particle assemblages, with symmetric interaction and switching field distributions [*Pike et al.*, 1999], has a symmetric vertical spread about the $B_i = 0$ axis (Figure 15f). This model result is too symmetric compared to FORC distributions for real samples that contain interacting SD particles (e.g., Figures 15a–15c). Part of the asymmetry of measured FORC diagrams results from the fact that the measurements start at positive saturation. If the measurements started from negative saturation, the FORC distribution would be a mirror image reflected about the $B_i = 0$ axis. The asymmetry will, therefore, disappear when the two are averaged. Nevertheless, some additional features need to be introduced to models to capture important aspects of measured FORC distributions. When the model is adjusted using a moving Preisach model [*Vajda and Della Torre*, 1991] to include a mean interaction field, three changes arise (Figure 15g). The peak of the FORC distribution is displaced below the $B_i = 0$ axis for a positive mean field (and above the $B_i = 0$ axis for a negative mean field), the distribution becomes elongated with a positive slope for a positive mean field (and with a negative slope for negative mean fields) [*Pike et al.*, 1999], and a negative region appears below the main positive peak. Such negative regions, in addition to those discussed above as inherent manifestations of SD behavior [*Newell*, 2005], occur in experimentally determined FORC diagrams (e.g., Figure 15c). *Stancu et al.* [2003] argued that such negative regions result from positive mean-field interactions that are related to a demagnetizing effect as seen in oriented acicular magnetic particulate systems. While these features are manifestations of mean-field interactions, *Pike et al.* [1999] demonstrated that mean-field interactions do not increase vertical spread in FORC diagrams. Thus, observed combinations of vertical spread, displacement of the FORC distribution peak below the $B_i = 0$ axis, elongation of the FORC distribution with positive slope, and negative regions not associated with SD behavior requires both local interaction fields and a positive mean interaction field. Numerical modeling of this type provides important constraints on understanding micromagnetic hysteresis mechanisms revealed in FORC diagrams.

Nanofabrication of regular arrays of magnetite particles has been attempted to provide a well-constrained test of interaction effects on paleomagnetic recording [*Krása et al.*, 2009, 2011]. So far, technical limitations have prevented production of large numbers of samples with varying particle size and separation. The magnetizations of such samples are also weak, and FORC diagrams are noisy; significant smoothing is needed, which limits analysis of magnetostatic interactions. Nevertheless, this approach has considerable potential in rock magnetism and future developments in nanofabrication of suitable samples would be welcome. Micromagnetic modeling of such particulate arrays provides useful confirmation of how SD particle systems behave with different particle spacings. *Carvallo et al.* [2003] modeled $3 \times 3 \times 3$ arrays of aligned elongated particles ($45 \times 30 \times 30$ nm) to assess magnetostatic interaction effects. When particles are separated by twice the particle length (or more), the resulting FORC diagram is the same as for an isolated SD particle, complete with negative region near the lower B_i axis at 45° below the peak on the $B_i = 0$ axis (Figure 16a). When the interparticle spacing is decreased to four thirds the particle length, interactions become important and different switching events become evident as separate isolated peaks in the FORC diagram (Figure 16b), as expected from the hysteron-based and Stoner-Wohlfarth-based analyses (Figures 3 and 4). For more closely spaced particles, FORC contributions overlap (Figure 16c), as is the case for large assemblages of interacting SD particles. Micromagnetic models, therefore, replicate the essential features observed experimentally for interacting SD particle systems and for *Preisach* [1935] models of interactions (Figure 3f).

7.3. Superparamagnetism

SP behavior occurs in small SD particles where thermal fluctuations cause random changes in direction of magnetic moments [*Néel*, 1949]. This relaxation occurs on laboratory timescales and can be measured as a
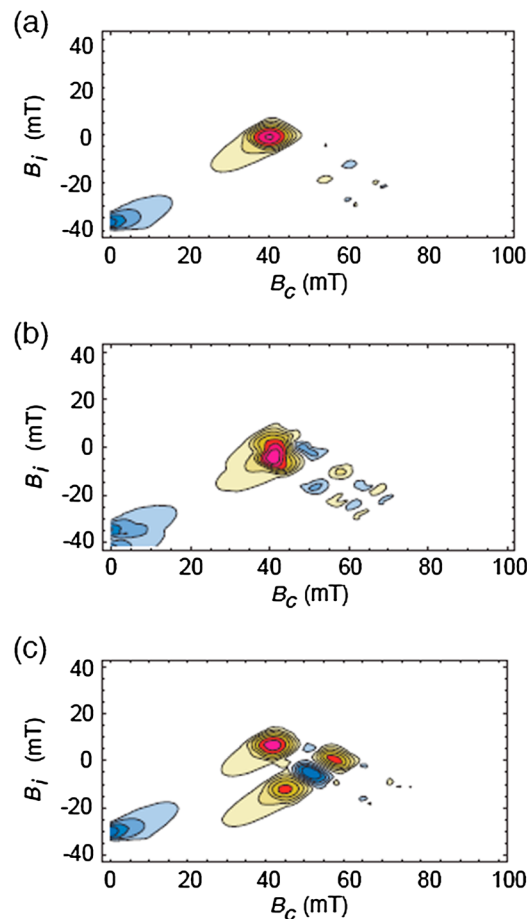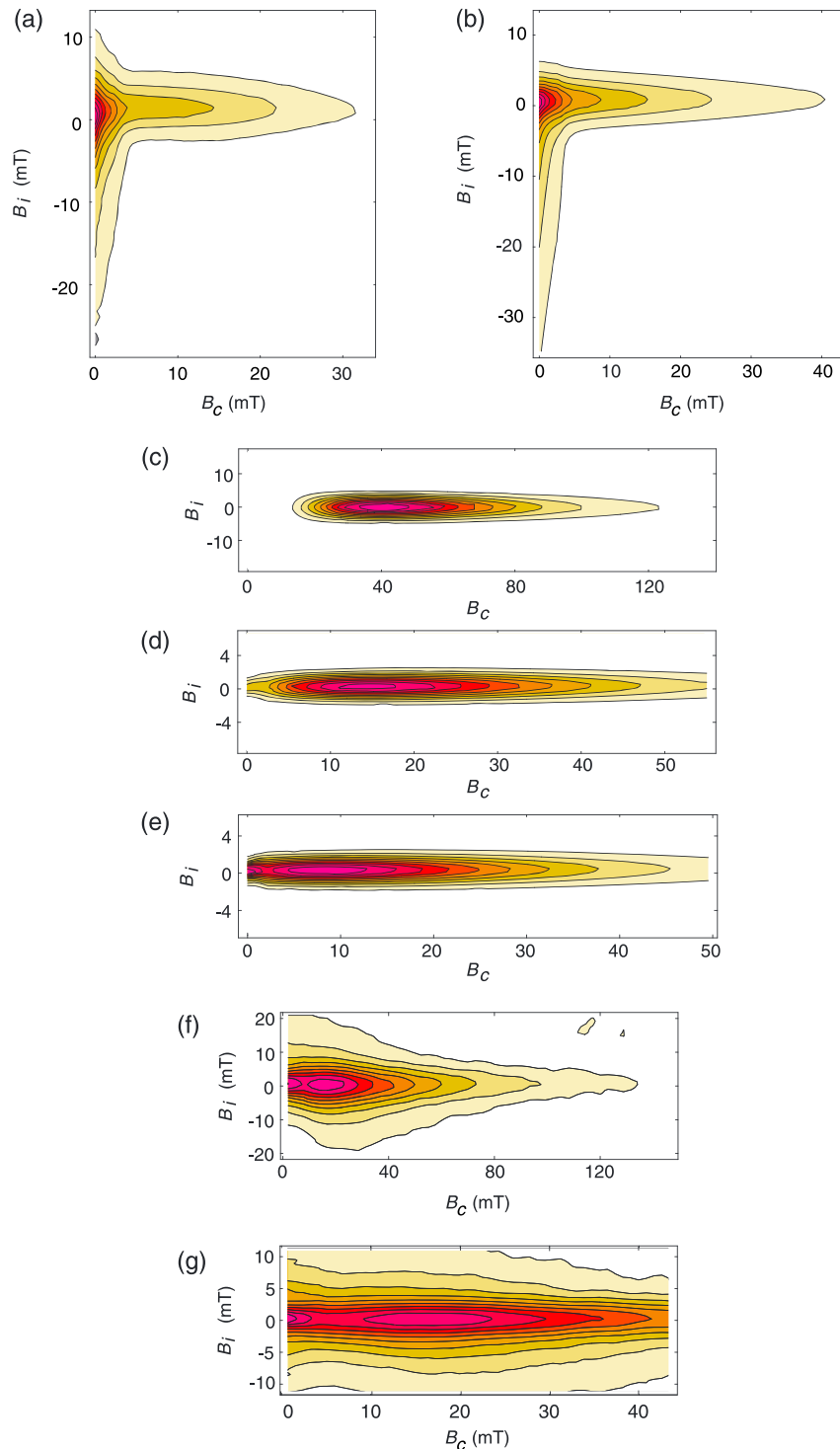
Figure 16. FORC diagrams for micromagnetic models of interacting SD particle systems. The models are for an array of $3 \times 3 \times 3$ elongated SD particles with grain size of $45 \times 30 \times 30$ nm. Few interactions are evident for (a) a particle spacing of twice the grain length, while interactions progressively increase at particle spacings of (b) 4/3 the grain length, and (c) 2/3 the grain length [after *Carvallo et al.*, 2003]. See text for discussion.

function of time, temperature, or field. SP particles give rise to completely reversible hysteresis loops (i.e., they cannot hold a remanent magnetization and do not exhibit hysteresis). Reversible magnetizations should make no contribution to a FORC diagram because the mixed second derivative in equation (1) will equal zero. However, FORC measurements are made rapidly so that particles with volumes near the SP to stable SD threshold size will produce hysteresis loops with slight irreversibility [*Pike et al.*, 2001a]. This can be visualized by imagining two FORCs, an upper one with B_r just greater than zero and another one with B_r just below zero. At B_r for the lower FORC, some SP particles, which did not switch their magnetization in the upper FORC, will switch. As the applied field increases, the magnetization of the lower FORC will, therefore, lag that of the upper FORC because of this relaxation. The small difference between successive FORCs will give rise to slight hysteresis that produces a nonzero result in equation (1) that contributes near the origin (i.e., $B_i = 0$, $B_c = 0$) of a FORC diagram [*Pike et al.*, 2001a]. Thermal relaxation in SP particles should, therefore, give rise to a peak near the origin of a FORC diagram, which will be in addition to any peak due to stable SD particles.

Examples of measured and modeled SP behavior in FORC diagrams are illustrated in Figure 17. A FORC diagram for a sample from the Tiva Canyon Tuff, Nevada, where magnetic properties are controlled by stratigraphic variations in SP particle concentration [e.g., *Worm*, 1998, 1999; *Worm and Jackson*, 1998; *Pike et al.*, 2001a; *Till et al.*, 2011], is shown in Figure 17a. *Worm* [1998, 1999] reported a frequency-dependent susceptibility of 30% for this sample. The dominant distribution at the origin of the FORC diagram is the major indicator of SP behavior, while the nearly vertical distribution in the lower quadrant is also an important feature associated with thermal relaxation [*Pike et al.*, 2001a]. These features can be replicated in numerical models of thermally relaxing uniaxially anisotropic SD particle systems (Figure 17b; for model details, see *Pike et al.* [2001a]). An assemblage of noninteracting stable SD particles with a lognormal particle volume distribution gives rise to the FORC diagram in Figure 17c. By progressively increasing the temperature, thermal relaxation causes the peak of the FORC distribution to shift progressively to lower coercivities (Figures 17d and 17e). As a result, what was a thermally stable population of SD particles (Figure 17c) still has a dominant peak associated with the SD particles, but now with lower coercivity, as well as a secondary peak at the origin of the FORC diagram (Figure 17e). Such manifestations of thermal relaxation have been widely reported [e.g., *Roberts et al.*, 2000; *Pike et al.*, 2001a] (Figures 17f and 17g).

The above results demonstrate that coercivity is not an intrinsic magnetic property, but that it depends on the thermal state of a sample. It is, therefore, only reasonable to use room temperature coercivity as indicative of magnetic mineralogy when the magnetic particle assemblage is in a thermally stable state. For example, a coercivity peak due to magnetite can only be distinguishable from one due to greigite if thermal relaxation has not caused overlap between the coercivity ranges of the two minerals. Thermal relaxation should be borne in mind when interpreting coercivity in terms of magnetic mineralogy. For a more comprehensive treatment of thermal relaxation and SP behavior on FORC diagrams, readers are referred to *Pike et al.* [2001a].

Figure 17. FORC diagrams for thermally relaxing (superparamagnetic) particles. Comparison of room temperature (300 K) FORC diagrams for (a) Tiva Canyon Tuff sample CS914 with (b) numerical model results. The dominant distribution at the origin of the FORC diagrams is due to particles near the SP to stable SD threshold size. Numerical model results for SD particle systems at different temperatures illustrate the effects of progressive thermal relaxation, where (c) at 0 K all particles are magnetically blocked in the stable SD state and (d, e) are at arbitrary higher temperatures where the FORC distribution progressively shifts to lower coercivities. At the highest modeled temperature in Figure 17e, a secondary peak appears at the origin of the FORC diagram in addition to the dominant peak due to thermally stable SD particles. (f) Normal and (g) high-resolution FORC diagrams with such secondary peaks for sediment from Butte Valley, California [*Roberts et al.*, 1996]. FORC diagrams in Figures 17a–17e and Figures 17f and 17g are after *Pike et al.* [2001a] and *Roberts et al.* [2000], respectively.

Temperature-dependent FORC measurements enable effective testing for thermally activated magnetic behavior. The first such low-temperature test was that of *Pike and Marvin* [2001] who worked with 10 nm magnetite particles in frozen ferrofluids. The particles are so fine grained that they only have stable SD properties at extremely low temperatures. By making FORC measurements between 20 and 5 K, *Pike and Marvin* [2001] demonstrated the features associated with thermal relaxation as illustrated in Figures 17c–17e. In Figure 18, we present previously unpublished results to illustrate how SP-dominated Tiva Canyon Tuff sample CS914 (Figure 17a) progressively blocks a stable SD magnetization with decreasing temperature. When cooled from room temperature (Figure 18a) to 200 K (Figure 18c), the dominantly SP assemblage changes to a dominantly SD assemblage; the secondary peak near the origin of the FORC diagram and the vertical distribution in the lower quadrant indicates that a significant amount of the magnetic particle assemblage remains in the SP state [*Pike et al.*, 2001a]. At 50 K, almost the entire assemblage is blocked in the stable SD state (Figure 18e). The peak coercivity shifts progressively from 0 mT at 300 K to ~30 mT at 200 K to ~90 mT at 50 K (Figures 18a, 18c, and 18e). These results can also be simulated using a numerical model (Figures 18b, 18d, and 18f) of the type used by *Pike et al.* [2001a]. Temperature-dependent FORC results in Figure 18 illustrate the range of effects associated with SP behavior, as outlined by *Pike et al.* [2001a].

7.4. Multidomain Behavior
7.4.1. Weak Domain Wall Pinning
Magnetic hysteresis in MD particle systems is complex and involves domain wall (DW) nucleation and annihilation, DW pinning, DW curvature, and DW interactions. For some well-behaved MD systems, hysteresis can be adequately explored using the simple DW pinning model of *Néel* [1955]. In this model, complex curvilinear DWs observed in real samples are treated as a collection of noninteracting planar DWs. The model thereby treats a bulk sample as a collection of small, noninteracting particles with similar size and with each particle containing a single planar DW. It is assumed that each DW travels through a one-dimensional DW pinning field, which represents the DW interactions within the particle. The pinning field can be modeled by a random function [*Bertotti et al.*, 1999], and the behavior of the bulk sample is modeled by taking an average over a statistical ensemble of pinning fields. *Bertotti et al.* [1999] obtained an analytical solution for a *Preisach* [1935] distribution (roughly equivalent to a FORC distribution) for the DW pinning model, which demonstrates that a FORC diagram will have a purely vertical form that will be a decreasing function of coercivity [*Pike et al.*, 2001b]. For mathematical details of the DW pinning model, and FORC diagrams that result from this model, see *Pike et al.* [2001b]. A FORC diagram for a simple DW pinning system is illustrated for a transformer steel sample, which has low coercivity and remanence and weak DW pinning (Figure 19a). The coercivity for this FORC distribution is <1 mT, which provides a measure of the strength of the DW pinning. Weak DW pinning behavior is also evident in a single 2 mm magnetite particle; after annealing at 1100°C, the FORC diagram (Figure 19b) is similar to that obtained for transformer steel (Figure 19a), except that it has higher coercivities. A much more complicated FORC diagram was obtained before annealing (Figure 19c), which indicates that factors related to internal stress (which appear to be largely removed by annealing) are likely to have a more important influence on hysteresis [*Pike et al.*, 2001b]. Detailed studies of how internal stress influences the hysteresis behavior observed in FORC diagrams have yet to be undertaken; however, it clearly introduces complexities into DW mechanics that cannot be accounted for by the simple DW model of *Néel* [1955]. Vertical lines that characterize weak DW pinning are still evident in a high-resolution FORC diagram at low coercivities for the 2 mm magnetite particle before annealing (Figure 19d). This difference compared to Figure 19c can be explained by the likelihood that DW segments can move locally in weak fields as if they are noninteracting, planar DWs, as is the case for transformer steel (Figure 19a). However, when the applied field is increased to larger values, DW movements occur throughout the particle over lengths comparable to the particle length. In this situation, stress provides a more dominant control on DW movement, which produces a more complicated FORC diagram (Figure 19c) compared to the vertical FORC distributions that occur within particle systems with weak DW pinning (Figure 19a) [*Pike et al.*, 2001b].

7.4.2. Strong Domain Wall Pinning
When pinning fields are not weak, the simple DW pinning model of *Néel* [1955] is no longer applicable. A physically more realistic random process is needed to represent the pinning field function. By treating bulk samples as statistical ensembles of grains with Gaussian volume distributions and an Ornstein-Uhlembeck random process [*Uhlenbeck and Ornstein*, 1930] to generate a pinning field in each grain, *Pike et al.* [2001b]
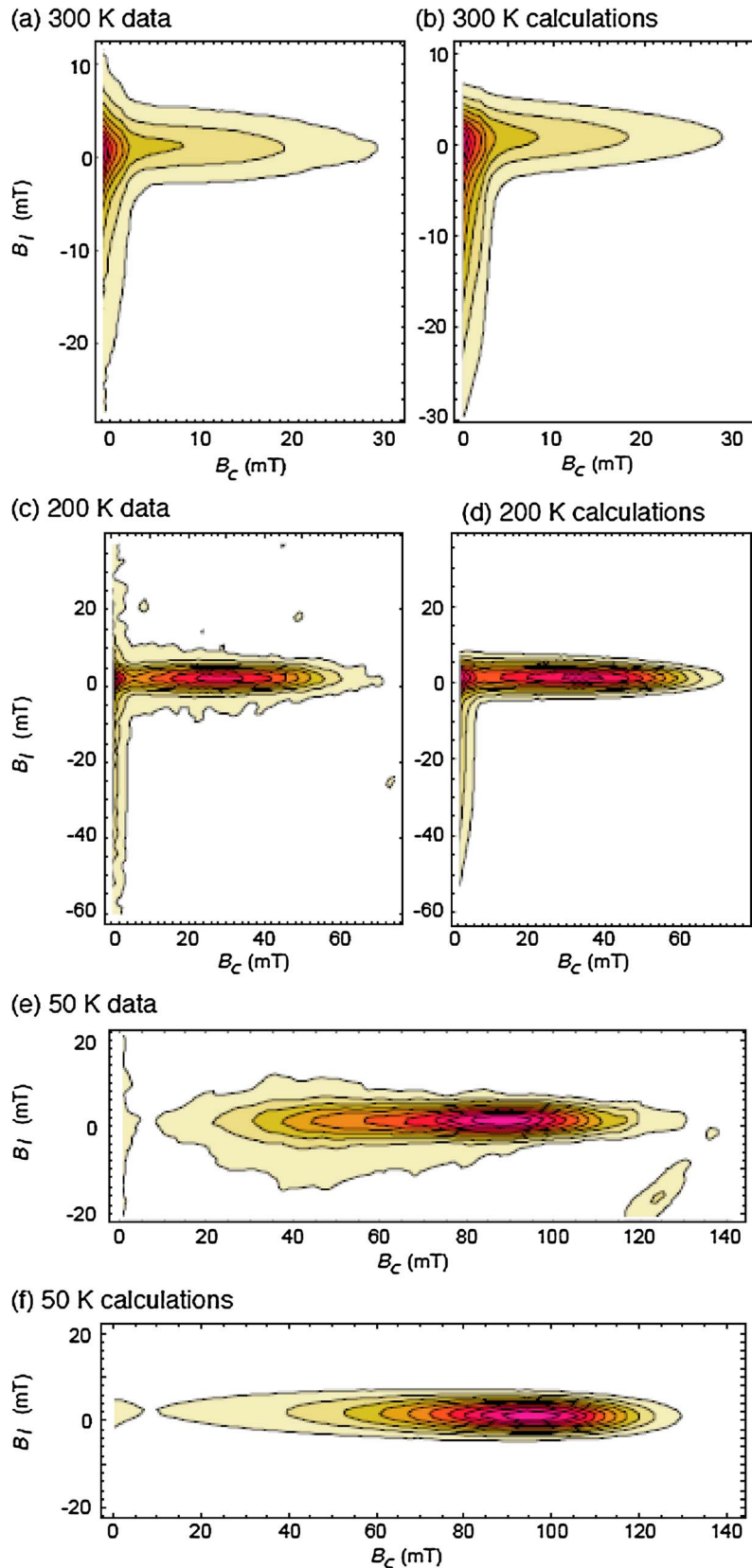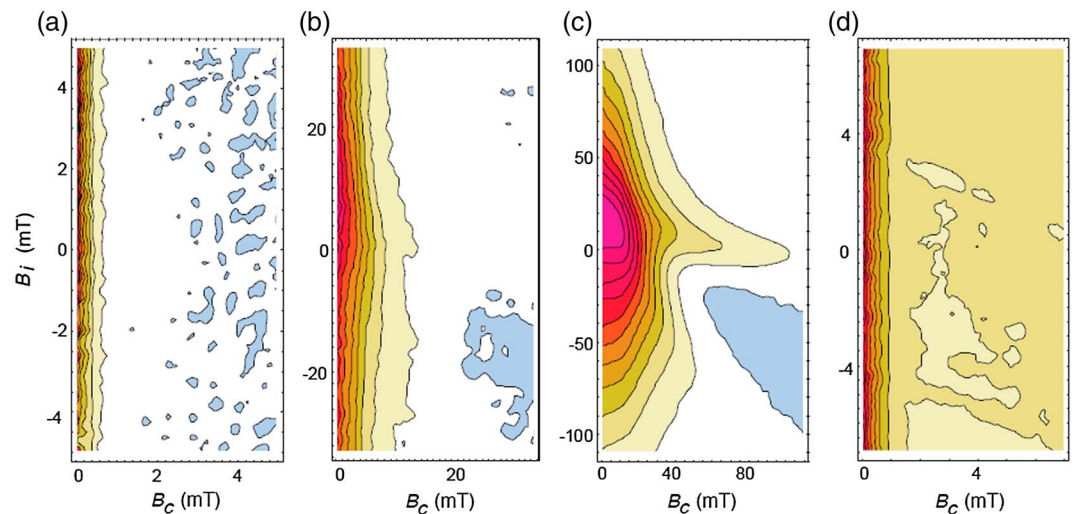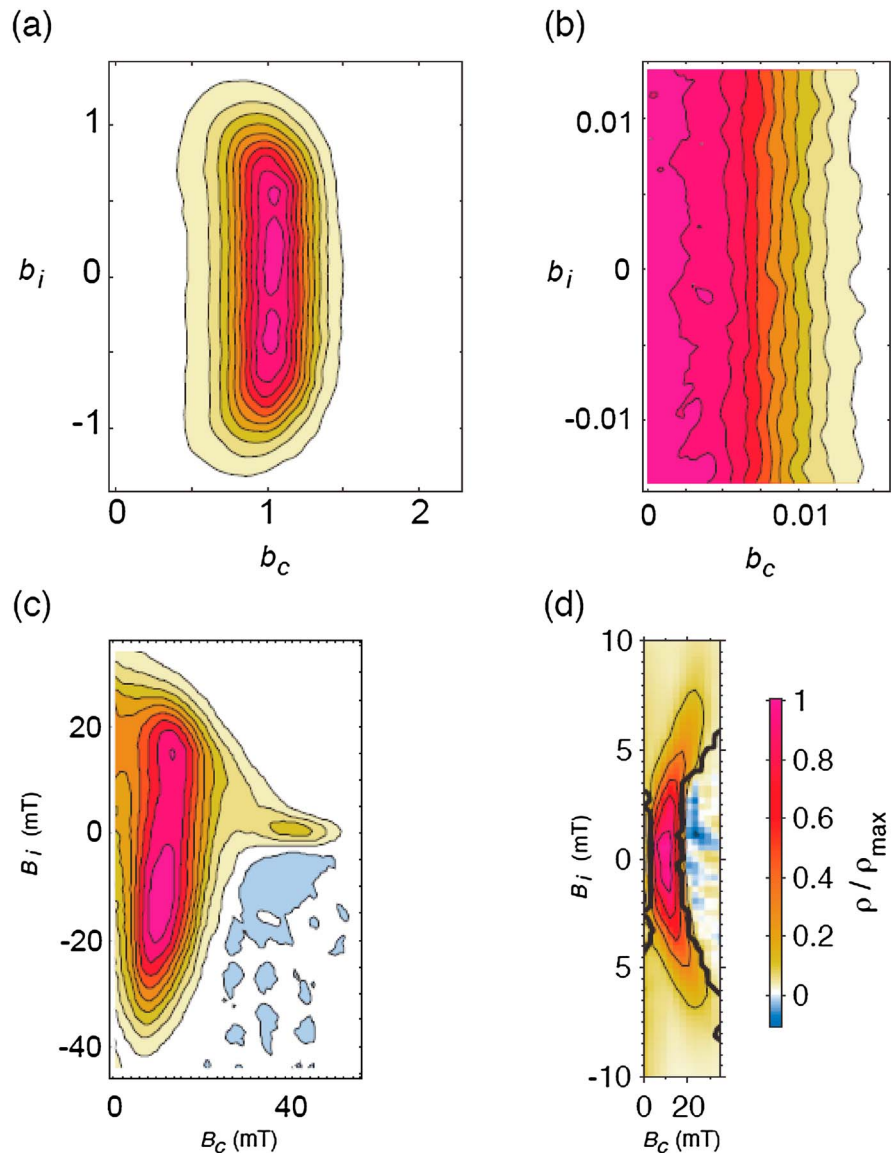
Figure 18

Figure 19. FORC diagrams for MD samples with weak domain wall (DW) pinning. Results for (a) transformer steel (sample M-80, Temple Steel Company) and a 2 mm magnetite (b) after and (c) before annealing at 1100°C [after *Pike et al.*, 2001b], and (d) a high-resolution FORC diagram for the low-field, weak DW pinning regime in the 2 mm magnetite before annealing. FORC diagrams in Figures 19a and 19d were collected for the study of *Pike et al.* [2001b] but have not been published before.

numerically simulated FORC diagrams for particle systems with strong DW pinning. These FORC distributions are vertically elongated, with variable separations from the vertical axis (Figure 20a). The coercivity of the peak of the FORC distribution occurs at the value of the dominant pinning field [*Pike et al.*, 2001b]. If the pinning field is weakened or strengthened, respectively, the peak of the FORC distribution will move closer or further away from the vertical axis of the FORC diagram (compare Figures 20a and 20b). Vertical spread in FORC diagrams for MD particle systems is a function of the internal demagnetization field [*Pike et al.*, 2001b], which depends on several factors (e.g., magnetic cancelation among domains, domain shape, and DW interactions) and increases with particle volume.

Many of the features observed by *Pike et al.* [2001b] in models for strong DW pinning had not been replicated in published studies of geological samples until the study of *Church et al.* [2011], although features shown in Figure 20a have been observed for alnico (iron-aluminum-nickel-cobalt alloy) magnets that were not previously published (Figure 20c) and in 65 nm diameter Co nanowires and nanotubes [*Proenca et al.*, 2013]. *Church et al.* [2011] investigated DW pinning in titanomagnetites and reported that a transition from weak (low-coercivity) to strong (high-coercivity) DW pinning occurs within the same samples during cooling from 100 to 50 K. A further modification was observed in their results at 50 K (Figure 20d) compared to those shown in Figure 20a, where the upper and lower ends of the vertical distributions shift to higher coercivities to produce a "crescent moon" FORC distribution. *Church et al.* [2011] replicated these features by modifying the model of *Pike et al.* [2001b]. To obtain larger coercivities at the tips of the distribution, *Church et al.* [2011] increased the amplitude of the pinning field as the sample approached magnetic saturation (i.e., as the DW approaches the edge of the particles). They attributed the crescent moon FORC distribution to a thermally activated relaxation process due to electron hopping, with relaxation occurring as a result of a magnetoelastic effect caused by enhanced magnetocrystalline anisotropy due to rearrangement of Fe^{2+}-Fe^{3+} within DWs. This example provides an excellent case study of the usefulness of FORC diagrams in detecting micromagnetic processes that can be explained successfully with numerical models, which together provide important insights into processes under investigation.

Figure 18. Comparison of experimental FORC diagrams for a dominantly SP particle system at room temperature (Tiva Canyon Tuff sample CS914) with numerical model results, respectively, at three temperatures. At (a, b) 300 K, where most of the assemblage is in a thermally relaxed state; (c, d) 200 K, where much of the particle system is in a thermally stable SD state, but part of the assemblage is in a thermally relaxed state; and (e, f) 50 K where almost all particles are blocked in a stable SD state. See text for discussion. These results have not been published before; model results were obtained using the model of *Pike et al.* [2001a].

Figure 20. FORC diagrams with strong domain wall (DW) pinning from (a, b) numerical models and (c, d) experimental measurements. In Figures 20a and 20b, the distribution peak is the dominant pinning field, while the vertical spread is due to internal demagnetizing fields within MD particles, which increases with particle size. Models are for particle systems with (Figure 20a) strong and (Figure 20b) weak DW pinning [after *Pike et al.*, 2001b]. Experimental FORC diagrams for an iron-aluminum-nickel-cobalt (alnico) hard magnet in Figure 20c, and large (tens to hundreds of micrometers) sintered synthetic polycrystalline titanomagnetite (TM40) at 50 K [*Church et al.*, 2011]. The FORC diagram in Figure 20c can be reproduced numerically using the strong DW pinning model of *Pike et al.* [2001b] with interacting DWs simulated using a local demagnetizing field, while the crescent moon features at the ends of the vertical FORC distribution in Figure 20d can be simulated by increasing the amplitude of the pinning field as the FORCs approach saturation (see text).

7.4.3. Natural Samples and Other MD Hysteresis Mechanisms

The above discussion of MD behavior and FORC diagrams has centered around variations on the DW pinning model of *Néel* [1955]. However, the MD behavior observed in FORC diagrams for most geological samples is of the type shown in Figure 21 rather than the types shown in Figures 19 and 20. The FORC diagrams in Figure 21 have contours that diverge away from the $B_i = 0$ axis and that are asymmetric about the $B_c = 0$ axis. We illustrate this pattern for synthetic MD magnetite (Figures 21a–21d) and sediment samples that contain MD particles (Figures 21e and 21f). This diverging pattern has been widely observed in Preisach and FORC diagrams for geological samples [e.g., *Mullins and Tite*, 1973; *Ivanov et al.*, 1981; *Ivanov and Sholpo*, 1982; *Zelinka et al.*, 1987; *Hejda and Zelinka*, 1990; *Dunlop et al.*, 1990; *Fabian and von Dobeneck*, 1997; *Roberts et al.*, 2000;
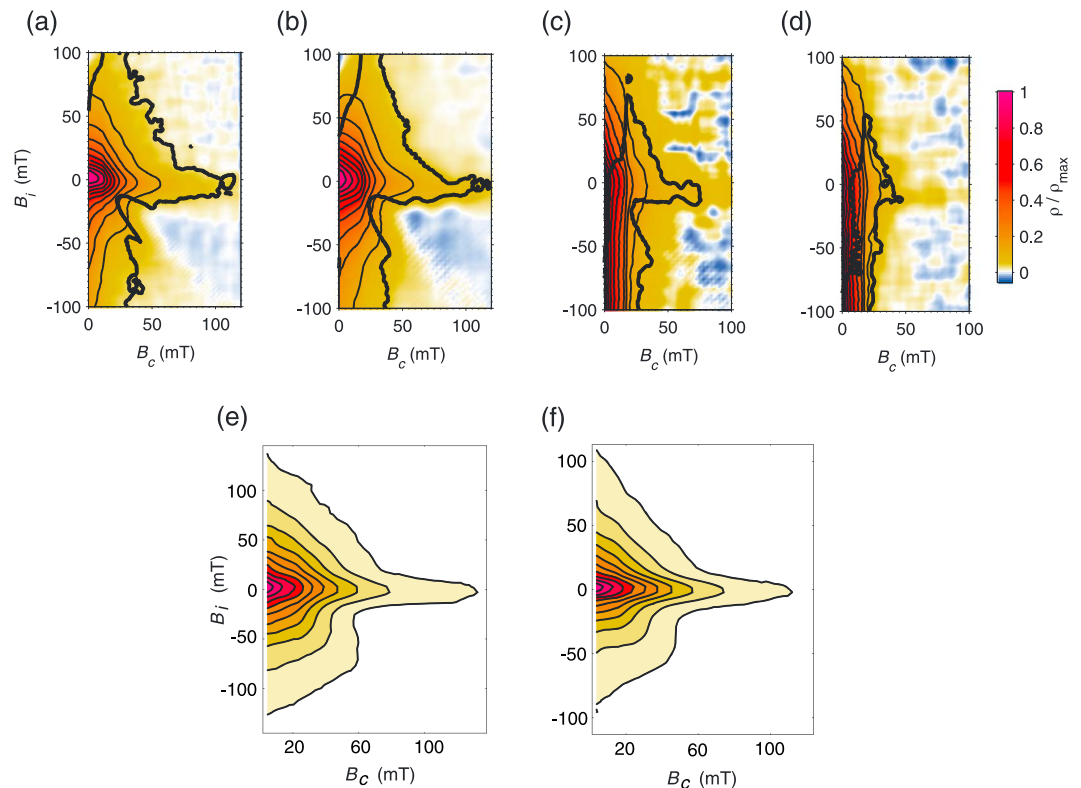
Figure 21. FORC diagrams for geologically relevant MD particle systems. Synthetic magnetite (W = Wright Industries; H = hydrothermal) with grain sizes of (a) 7 μm (W), (b) 11 μm (W), (c) 39 μm (H), and (d) 76 μm (H) [after *Muxworthy and Dunlop*, 2002]. With increasing grain size, there is a progressive divergence away from horizontal distributions for SD particle systems (Figure 14) toward vertical distributions parallel to the B_i axis (Figure 19). FORC diagrams for MD-dominated sediments from (e) the Labrador Sea and (f) North Pacific Ocean [after *Roberts et al.*, 2000] are consistent with those from the fine end of the MD spectrum from *Muxworthy and Dunlop* [2002]. The classical DW pinning model of *Néel* [1955] does not explain hysteresis in natural MD samples; additional mechanisms, such as DW nucleation and annihilation, DW interactions, and DW curvature, are needed. SF = 3 for all.

Pike et al., 2001b; *Muxworthy and Dunlop*, 2002; *Muxworthy et al.*, 2005; *Wehland et al.*, 2005a, 2005b; *Smirnov*, 2006, 2007]. *Pike et al.* [2001b] concluded that the classical DW pinning model of *Néel* [1955] is inadequate to explain hysteresis mechanisms in natural MD samples and argued that additional mechanisms, such as DW nucleation and annihilation, DW interactions, and DW curvature, are needed to explain observations. Detailed modeling has yet to be undertaken to explain the observed features of FORC diagrams for natural MD materials. As shown throughout this paper, combining numerical modeling with experimental results can help to explain not only the major features but also subtleties in hysteresis mechanisms that are important for understanding different types of magnetic behavior. However, much remains to be done to explain important details of hysteresis mechanisms in MD materials.

7.5. Single Vortex Behavior

In the paleomagnetic literature, the transitional state between the SD and MD states is referred to as the PSD state where magnetic particles have a mixture of SD-like (high-M_{rs}) and MD-like (low-B_c, B_{cr}) properties [*Stacey*, 1963]. Micromagnetic simulations indicate that within fine particles with nonuniform but relatively stable magnetizations, the magnetization fans or curls into flower or vortex states [*Schabes and Bertram*, 1988; *Williams and Dunlop*, 1989, 1995]. Some authors consider the flower and vortex states to provide a more feasible explanation [e.g., *Tauxe et al.*, 2002] than the many traditional explanations for widely observed PSD behavior [e.g., *Halgedahl and Fuller*, 1983; *Dunlop*, 1986]. FORC diagrams provide a useful test of these possibilities, as discussed below (including section 7.6).

Pike and Fernandez [1999] used FORC diagrams to investigate the single vortex magnetic state within arrays of cobalt dots (with dimensions of 260 × 450 × 30 nm) produced by interference lithography. They reported
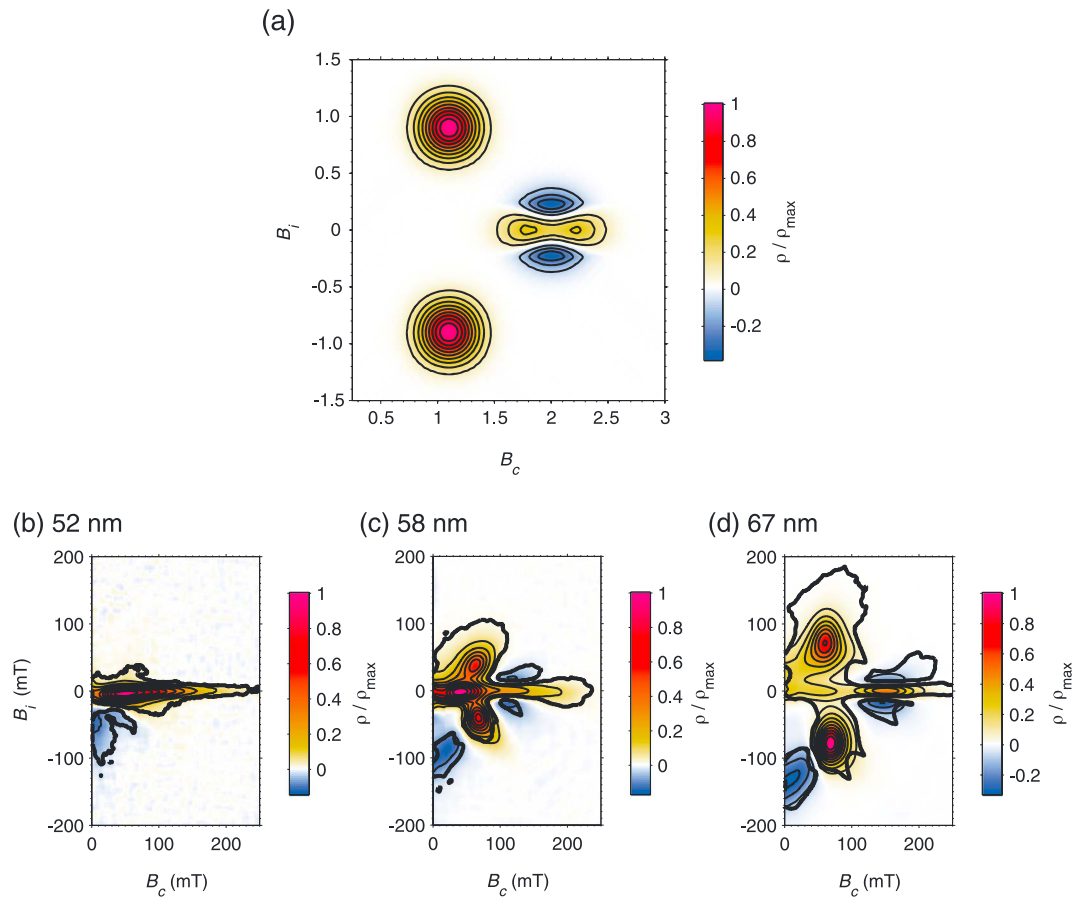
Figure 22. FORC diagrams for models and synthetic samples with single vortex systems. (a) Model results from *Pike and Fernandez* [1999]. The offset of the upper and lower peaks from the $B_i = 0$ axis provides a measure of the vortex nucleation and annihilation fields. FORC diagrams for iron nanodots with a progression from (b) stable SD behavior (for 52 nm nanodots) to (c) single vortex behavior (for 58 nm nanodots) to (d) single vortex behavior with a larger nucleation/annihilation field (for 67 nm nanodots) [after *Dumas et al.*, 2007a].

FORC diagrams with three prominent features (Figure 22a): two positive peaks occur in the upper and lower half planes of the diagram, and a weaker "butterfly" feature occurs along the $B_i = 0$ axis that consists of a circular negative region with a superimposed elongated horizontal positive region. The features in Figure 22a are explained by nucleation and annihilation of a single vortex state within fine magnetic particles. That is, when the magnetization is decreased from saturation, a vortex will form at a given nucleation field. Likewise, for an ascending FORC, the vortex will annihilate but not necessarily at the same absolute field value at which it nucleated. Different nucleation and annihilation fields are more likely if there are physical irregularities in a sample. The positive peaks in the upper and lower quadrants occur at a distance from the $B_i = 0$ axis that corresponds to the value of the vortex nucleation/annihilation fields. Any vertical spread in these peaks reflects the distribution of nucleation/annihilation fields. The butterfly feature along the horizontal axis of a FORC diagram has been modeled as resulting from the presence of two distinct annihilation fields [*Pike and Fernandez*, 1999]. It will not be present without the two distinct annihilation fields.

Single vortex features have been reported on FORC diagrams for <100 nm iron nanodots [*Dumas et al.*, 2007a, 2007b]. As the size of the nanodots increases from a stable SD state (52 nm; Figure 22b), single vortex features become evident at dot sizes of 58 nm (Figure 22c). The magnitude of the major peaks increases, as does their distance from the $B_i = 0$ axis (the nucleation/annihilation field), as the dot size increases further to 67 nm (Figure 22d). To our knowledge, dusty olivine in chondritic meteorites is the only geological material that has been suggested to contain single vortex-like states as inferred from FORC diagrams [*Lappe et al.*, 2011, 2013]. Regardless, micromagnetic simulation of an elongated magnetite particle (100 × 80 × 80 nm) just
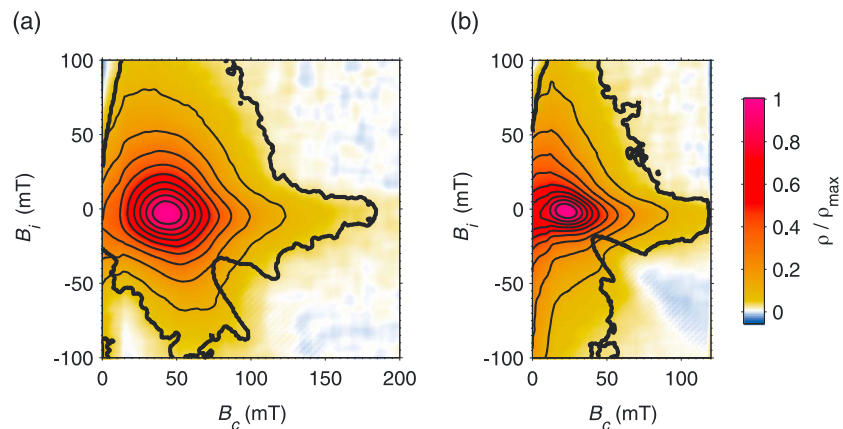
(a)

(b)
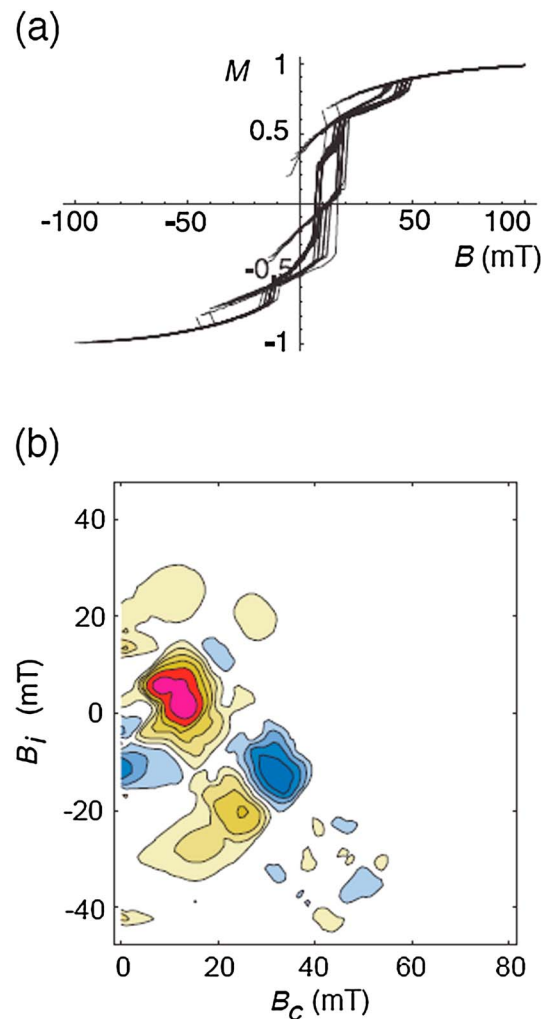
Figure 23. Micromagnetic model results for an elongated single isolated magnetite particle that exceeds the stable SD threshold size (grain size = $100 \times 80 \times 80$ nm). Changes from the stable SD state with decreasing field from positive saturation to a flower state to a vortex state and back with approach to positive saturation during measurement of successive FORCs gives rise to (a) magnetic switching events at different fields, which produces (b) a complex FORC diagram with multiple peaks [after *Carvallo et al.*, 2003].

above the stable SD-PSD threshold is likely to be relevant to geological samples [*Carvallo et al.*, 2003]. When the magnetization of such a particle decreases from saturation, it progressively changes from a stable SD state to a flower state to a vortex state, and back to a flower state and SD state as it approaches negative saturation. These intermediate magnetization states have variable switching branches in simulated FORCs that do not always occur at the same field (Figure 23a). These branches give rise to splitting of the single peak for an isolated stable SD particle (Figure 3b) into several positive and negative peaks (Figure 23b). A randomly oriented assemblage of such particles will give rise to multiple peaks on a FORC diagram that could explain the broad spread observed in geological samples with PSD behavior (Figure 24). Future work is needed to test whether PSD behavior in natural materials can be fully explained by vortex states.

7.6. Pseudosingle Domain Behavior

Roberts et al. [2000] provided the first description of PSD behavior in FORC diagrams. Their FORC diagrams contained evidence of mixtures of SD-like and MD-like magnetic moments. The SD-like moments are evident as peaks with closed contours, while the MD-like moments are evident as contours that diverge toward the B_i axis. The FORC distributions are also asymmetric, with a vertical part of the distribution occurring in the lower half of the diagram. However, *Roberts et al.* [2000] studied sediment samples for which the presence of SD and MD mixtures could not be excluded. A crucial test of their observations was provided by analysis of synthetic magnetite with known grain size [*Muxworthy and Dunlop*, 2002], which confirms the presence of both SD-like and MD-like moments in these PSD magnetites (Figure 24). For the finest-grained sample (0.3 μm; Figure 24a), the SD peak is affected by magnetostatic interactions that give rise to large vertical spread of the FORC distribution, which has a high coercivity (>40 mT), with the outer contours diverging toward the B_i axis. The 1.7 μm sample gives rise to a more typical PSD FORC diagram in which the coercivity peak occurs at lower values of ~20 mT, with more of the FORC distribution diverging toward the B_i axis. *Roberts et al.* [2000] provided results for more PSD samples and demonstrated that with increasing grain size, the SD-like peak progressively shifts to lower coercivities (high-resolution FORC diagrams are often needed to detect this) and that the MD-like magnetization diverges increasingly toward the B_i axis. *Muxworthy and Dunlop* [2002] provided a further important observation for PSD particles by making high-temperature FORC measurements. At elevated temperatures, FORC diagrams progressively contract without changing shape up to ~500°C. This apparent decrease in interaction field strength with temperature is proportional to the corresponding decrease in M_s for the measured samples, which is consistent with the interpretation of *Néel* [1954], which suggests that the underlying domain structure did not change with temperature. Above 500°C, the FORC diagrams become more MD-like and symmetric. The decrease in asymmetry with temperature indicates that magnetostatic interactions are responsible for the asymmetry.

Figure 24. FORC diagrams for synthetic PSD samples with well-controlled grain size. Results (SF = 3) are for two Wright Industries samples with grain sizes of (a) 0.3 μm and (b) 1.7 μm [after *Muxworthy and Dunlop*, 2002]. As grain size increases, the SD-like peak shifts progressively to lower coercivities, and the outer contours diverge progressively toward the $B_i = 0$ axis and become more MD-like [cf. *Roberts et al.*, 2000].

Low-temperature FORC features have been proposed to provide a diagnostic indicator of PSD magnetite. Above the Verwey transition temperature, FORC diagrams are typical of PSD systems (Figures 25f–25i). Below the transition, the FORC distribution splits into upper and lower peaks that are roughly symmetric about $B_i = 0$ (Figures 25a–25d) [*Carvallo and Muxworthy*, 2006; *Smirnov*, 2006, 2007]. *Smirnov* [2007] demonstrated that the splitting of the FORC distribution depends on applied field during cooling; it is present after cooling in zero or low applied field (10–50 mT) and disappears at higher fields (>100 mT). This splitting was suggested to be diagnostic of PSD magnetite. Such splitting has not been observed in the spinel iron sulfide, greigite, which lacks a Verwey-like low-temperature transition [*Chang et al.*, 2009; *Roberts et al.*, 2011b].

Now that FORC diagrams have been presented for PSD particle systems, we can return to the question as to whether they can be explained by magnetic vortex states. If one imagines a random particle assemblage with a grain size distribution that spans the types of FORC diagrams in Figure 22b-d, the resultant FORC distribution would fill the space between the peaks in Figure 22a and could resemble a typical PSD result (e.g., Figure 24b). The negative peaks in the upper and lower parts of the butterfly structure of *Pike and Fernandez* [1999] or in the micromagnetic simulation of *Carvallo et al.* [2003] are weaker than the positive peaks; a summed FORC response from multiple particles is, therefore, likely to give a net positive response. Splitting of FORC distributions into upper and lower peaks below the Verwey transition temperature [*Carvallo and Muxworthy*, 2006; *Smirnov*, 2006, 2007] is similar to features observed in single vortex systems (Figure 22). These observations provide an avenue for future research to confirm if PSD behavior in natural materials can be explained by vortex states. If so, vortex nucleation and annihilation could explain the divergence of FORC distributions from horizontal distributions due to noninteracting SD systems and vertical distributions due to strong DW pinning in MD systems.

7.7. Other Rock Magnetic Information That Can Be Extracted From FORC Diagrams

Samples are commonly subjected to a series of magnetic analyses, including IRM acquisition, backfield demagnetization, hysteresis, and FORC measurements. While it is important to measure a hysteresis loop to define the parameters for a FORC measurement sequence, IRM acquisition and backfield demagnetization measurements are redundant because they can be derived from FORC measurements. These curves can be reconstructed from remanence values at $B = 0$ for each FORC when it passes from negative to positive applied fields. Resulting coercivity profiles along $B_{int} = 0$ (Figures 1b and 1e) can be subjected to unmixing analysis [e.g., *Robertson and France*, 1994; *Kruiver et al.*, 2001; *Heslop et al.*, 2002; *Egli*, 2004]; much useful information can be obtained from these profiles [e.g., *Muxworthy and Dunlop*, 2002; *Carvallo et al.*, 2006a; *Rowan and Roberts*, 2006; *Geiss et al.*, 2008] and by unmixing or other analyses to understand central ridge signatures [e.g., *Ludwig et al.*, 2013; *Heslop et al.*, 2014].
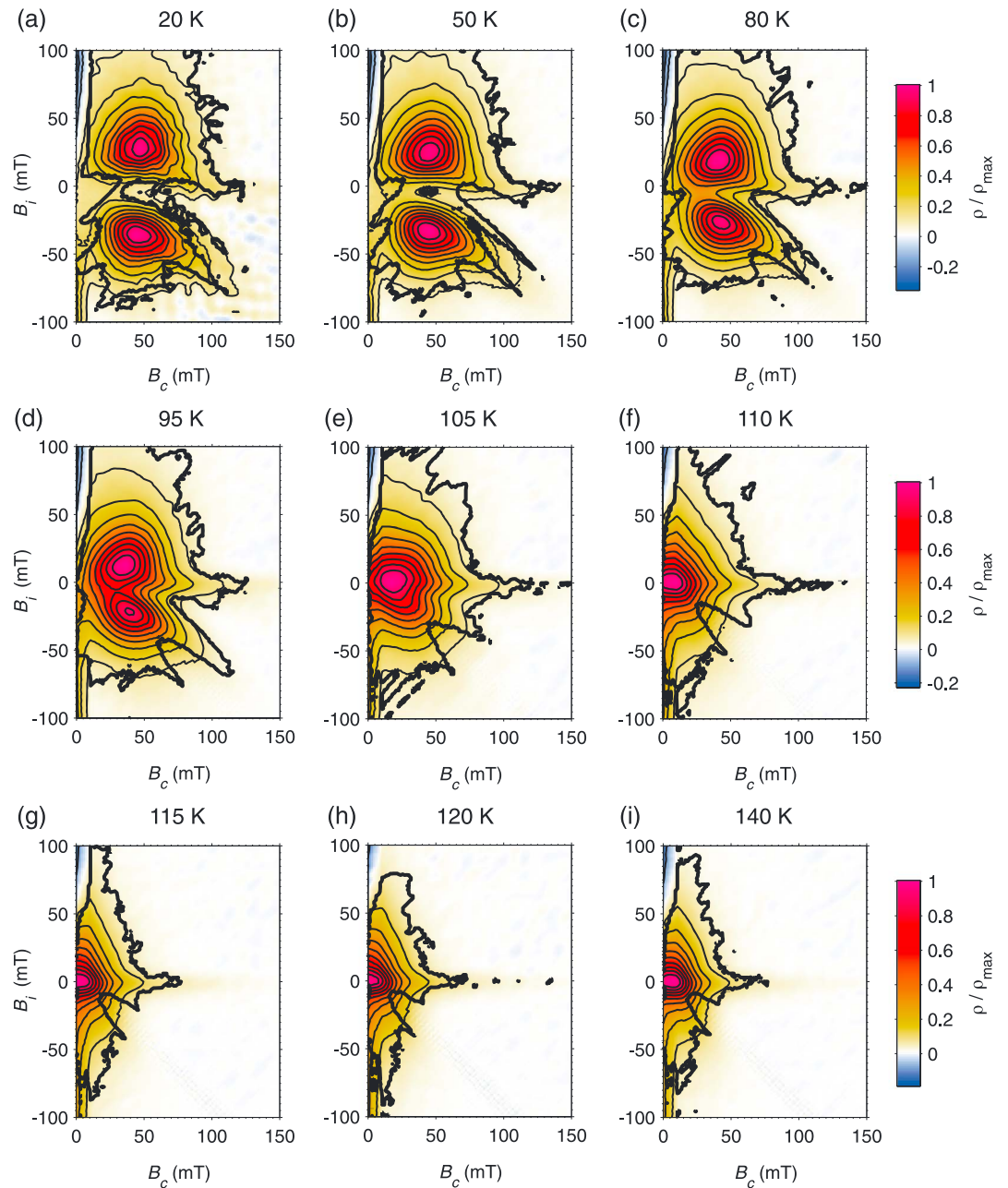
Figure 25. Temperature dependence of FORC diagrams for PSD magnetite above and below the Verwey transition. FORC diagrams (SF = 2 for all) after zero field cooling during warming from 20 to 300 K at (a) 20 K, (b) 50 K, (c) 80 K, (d) 95 K, (e) 105 K, (f) 110 K, (g) 115 K, (h) 120 K, and (i) 140 K [from *Smirnov*, 2006]. Above the Verwey transition temperature, FORC diagrams are typical of PSD systems, as shown in Figure 24. Below the Verwey transition, the FORC distribution splits into upper and lower peaks. This behavior has been suggested to be a diagnostic feature of PSD magnetite [*Carvallo and Muxworthy*, 2006; *Smirnov*, 2006, 2007].

8. Geophysical, Geological, and Environmental Prospects for Use of FORC Diagrams

The domain-state-dependent framework for interpreting FORC diagrams outlined above is based largely on magnetite. The manifestations of domain state variations and magnetostatic interactions in FORC diagrams are the same for all magnetic minerals, so there is no need to provide a detailed exposition of magnetic behaviors observed for all well-studied magnetic minerals, although different magnetic anisotropy regimes could conceivably give rise to different magnetic responses in FORC diagrams. For descriptions of the

magnetic response of different magnetic minerals in FORC diagrams, we refer readers to the following key papers for magnetite [*Roberts et al.*, 2000; *Muxworthy and Dunlop*, 2002], titanomagnetite [*Carvallo et al.*, 2006a; *Church et al.*, 2011], hematite [*Muxworthy et al.*, 2005; *Roberts et al.*, 2006; *Brownlee et al.*, 2011], goethite [*Roberts et al.*, 2006], greigite [*Roberts et al.*, 2006, 2011b; *Rowan and Roberts*, 2006; *Chang et al.*, 2007, 2009; *Vasiliev et al.*, 2007], pyrrhotite [*Weaver et al.*, 2002; *Wehland et al.*, 2005a; *Roberts et al.*, 2006; *Larrasoaña et al.*, 2007], and tetrataenite [*Acton et al.*, 2007b; *Gattacceca et al.*, 2014]. When interpreting FORC diagrams for natural materials, it is important to recognize that thermal relaxation within part of a magnetic mineral assemblage will reduce the coercivity of the sample. This can cause overlap in magnetic properties for minerals that might otherwise have contrasting coercivities [*Roberts et al.*, 2006]. Temperature dependence is an important aspect of FORC diagrams. Readers are referred to the following key papers for the temperature-dependent FORC properties of different minerals, including magnetite [*Muxworthy and Dunlop*, 2002; *Carvallo et al.*, 2004; *Carvallo and Muxworthy*, 2006; *Smirnov*, 2006, 2007], titanomagnetite [*Church et al.*, 2011], and greigite [*Chang et al.*, 2009]. We are unaware of extensive low-temperature FORC data for other magnetic minerals.

We now outline briefly some particularly useful applications and limitations of FORC diagrams that have not been covered in our treatment above. Many important applications, such as identification of biogenic magnetite, are discussed in section 7.1 and are not repeated below. We also focus on some notable features observed in FORC diagrams for some magnetic minerals.

8.1. Prescreening Samples for Absolute Paleointensity Analysis

The effect of magnetostatic interactions on magnetic recording fidelity has been under-assessed in rock magnetism because of ambiguities in the standard methods that have been used to detect interactions [e.g., *Henkel*, 1964; *Cisowski*, 1981]. FORC diagrams are well suited to assessing magnetic recording fidelity in cases where interactions are important. For example, interactions are important for determining the absolute intensity of the ancient geomagnetic field, which depends crucially on the applicability of the three laws of *Thellier* [1938]; reciprocity, independence, and additivity of a pTRM. Rocks with noninteracting SD particles are ideal for absolute paleointensity analysis and will satisfy the laws of *Thellier* [1938], whereas these laws will not be satisfied by rocks in which local interaction fields exceed the strength of the (Earth-like) laboratory field used in the paleointensity experiment [*Dunlop*, 1969]. Earlier attempts to screen for ideal or nonideal magnetic properties for absolute paleointensity analysis [e.g., *Thomas*, 1993; *Cui et al.*, 1997; *Perrin*, 1998] were not successful because bulk magnetic parameters are unsuitable for disentangling different magnetic mineral components. FORC diagrams provide an opportunity to move past these traditional limitations and develop a more robust approach to prescreening samples for absolute paleointensity analysis.

The first study conducted for this purpose was that of *Wehland et al.* [2005b]; only 12 samples were analyzed, which limits the wider applicability of the results. *Carvallo et al.* [2006a] measured FORC diagrams for close to 200 sister samples (mainly basalts) from sites that had been subjected to paleointensity experiments and used two FORC-related parameters to test for ideal magnetic properties. First, the full width at half maximum (FWHM) for profiles of the interaction field distribution through the coercivity peak parallel to the B_i axis provides a measure of the strength of magnetostatic interactions. Second, the width of the FORC distribution along the B_i axis provides a measure of the vertical spread of the FORC distribution associated with MD particles. Bulk coercivity B_c was used as an additional measure of domain state. By setting appropriate values for these easily determined parameters, *Carvallo et al.* [2006a] could only exclude 32% of samples with nonideal magnetic properties for paleointensity experiments. Most paleointensity results that failed to pass the selection criteria of *Kissel and Laj* [2004] are from samples with ideal noninteracting SD properties; their failure to pass the selection criteria resulted from thermal alteration that occurred during repeated heating in the paleointensity experiments. *Carvallo et al.* [2006a] concluded that being able to exclude one third of samples from further consideration would increase the efficiency of paleointensity experiments.

Paterson et al. [2010] used the selection criteria of *Carvallo et al.* [2006a] for paleointensity analysis of multiple lithologies within pyroclastic deposits. B_c was not found to provide discrimination between good and bad paleointensity results. When plotting width versus FWHM, *Paterson et al.* [2010] found that about 50% of samples that pass the experimental criteria for acceptance of paleointensity data were excluded by the

criteria of *Carvallo et al*. [2006a]. Despite these results, *Paterson et al*. [2010] concluded that FORC diagrams provide useful indicators of the causes of failure of paleointensity experiments for samples with ideal rock magnetic properties (i.e., thermal alteration). Likewise, samples with MD-like and PSD-like properties often fail pTRM tail checks. Overall, however, it is likely that the failure of FORC diagrams to provide discriminative preselection in the study of *Paterson et al*. [2010] results from the fact that a TRM is a weak-field remanence that can be controlled by fine (SD) magnetic particles, while high-field FORC measurements can overemphasize the contribution from coexisting large MD grains at the expense of fine SD grains. While the number of such studies remains small, future efforts should bear in mind that high-field measurements (e.g., FORCs) can have limited diagnostic capability when assessing the fidelity of weak-field TRM acquisition.

8.2. Preisach-Based Absolute Paleointensity Determination

Absolute paleointensity determinations are made conventionally for materials that carry a TRM [*Thellier and Thellier*, 1959]. However, the thermal treatments used in Thellier-Thellier and related techniques are not suitable for some materials that are prone to chemical alteration during heating, especially meteorites. This makes it useful to have robust nonheating paleointensity techniques. *Muxworthy and Heslop* [2011] proposed a new nonheating approach for paleointensity determination based on *Preisach* [1935] theory. In this approach, *Preisach* [1935] models are used to predict the response of a magnetic particle system to variations in magnetic field, thermal activation energy, and temperature. The Preisach (FORC) distribution can then be used to estimate the TRM intensity for a given field strength. FORC diagrams also have the advantage of enabling determination of the strength of magnetostatic interactions, which are assumed not to be present and are not considered in conventional paleointensity approaches. Additionally, paleointensity estimations with the Preisach-based approach are claimed to not depend on magnetic domain state [*Muxworthy and Heslop*, 2011]. The theoretical framework provided by *Muxworthy and Heslop* [2011] has been extensively tested on modern volcanic materials from which paleointensities have been determined with other methods and for which the present-day geomagnetic field intensity is known [*Muxworthy et al*., 2011]. Their results compare favorably with known field intensities (within 6% of the known field value) and with results from Thellier-type analyses, although samples with magnetizations carried by MD particles consistently provided underestimates of the known field strength. *Muxworthy et al*. [2011] also obtained accurate results for samples that failed to provide robust results from Thellier-type analyses. *Lappe et al*. [2013] tested the Preisach-based paleointensity method with well-characterized synthetic dusty olivine samples and found that the method works well for noninteracting SD particle systems but that it fails for single vortex-dominated systems because SD thermal relaxation theory is not applicable to such systems. Overall, it appears that the Preisach-based absolute paleointensity method of *Muxworthy and Heslop* [2011] provides a useful complement to the well-established Thellier-type methods for some materials.

## 8.3. Mixtures of Magnetic Minerals and FORC Unmixing

A key original motivation for using FORC diagrams was to move away from simplistic interpretation of natural magnetic mineral assemblages based on bulk magnetic properties and to identify magnetic components within complexly mixed samples [*Roberts et al*., 2000]. Many studies have used FORC diagrams to unravel complex magnetic mixtures. For example, *Roberts et al*. [2000] identified mixtures of magnetite and goethite in archeomagnetic samples and mixtures of SD and MD magnetite (rather than only PSD magnetite) in lake sediments. We selectively illustrate the use of FORC diagrams to discriminate mixtures of magnetic minerals.

Weaver et al. [2002] reported a mixing trend between SD-like and PSD-MD properties in a Day diagram [*Day et al*., 1977] (Figure 26a). When FORC diagrams were measured for samples at each end of the mixing trend, the SD-like sample was confirmed to have closed contours that indicate a strongly interacting SD particle assemblage. Scanning electron microscope observations confirm that this sample contains authigenic pyrrhotite that occurs as interlocking plates, which provides an explanation for the strong magnetostatic interactions detected. Surprisingly, samples at the more MD-like end of the mixing trend contain what would now be recognized as a central ridge signature (Figure 26a), which is probably due to biogenic magnetite. The position at the coarser end of the Day diagram for this sample is likely to result from a detrital PSD magnetite contribution with diverging contours on the FORC diagram. A secondary peak at the origin of the FORC diagram indicates an SP contribution that will also pull the data distribution away from SD values toward PSD-MD-like values. An intermediate sample along the mixing trend (not shown in Figure 26a) appears to contain a mixture of the three components identified in the coarser-grained end-member plus the
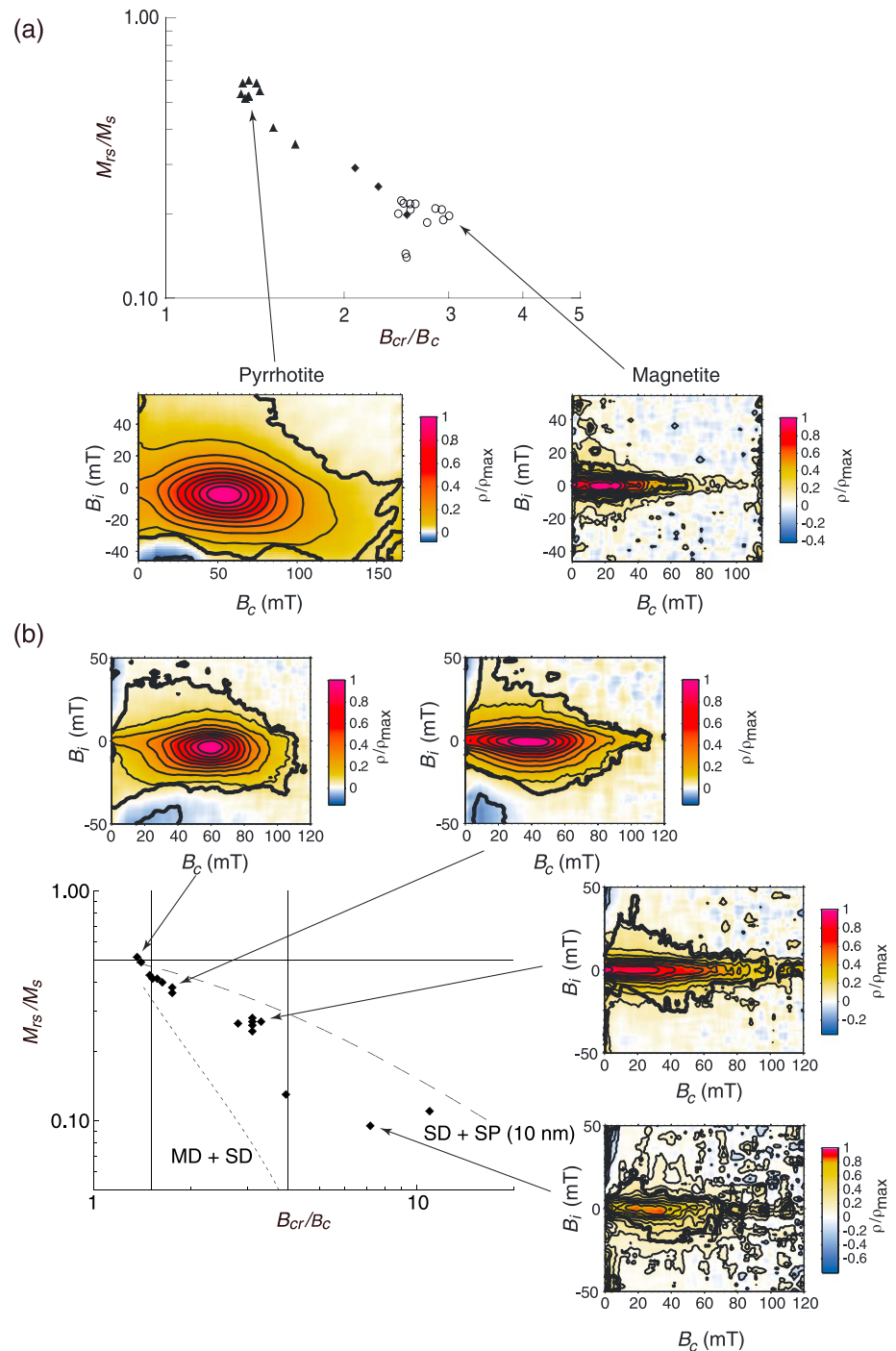
Figure 26. Use of FORC diagrams to understand magnetic mixtures. (a) Mixture of strongly interacting SD pyrrhotite and noninteracting SP, SD, and PSD magnetite plotted on a Day diagram [*Day et al.*, 1977] for Miocene mudstones from Sakhalin, Russia [after *Weaver et al.*, 2002]. (b) Mixture of strongly interacting SD greigite with variable admixtures of SP and noninteracting SD greigite [after *Rowan and Roberts*, 2006]. SF = 5 for all.

interacting SD pyrrhotite end-member [*Weaver et al.*, 2002]. The pyrrhotite component has caused a late diagenetic remagnetization, while samples that contain the SD magnetite were interpreted to carry a reliable syndepositional paleomagnetic signal [*Weaver et al.*, 2002]. Overall, the samples studied by *Weaver et al.* [2002] contain four detected mineral magnetic components despite the fact that the Day diagram appears to represent a simple binary mixing system. Binary mixing does not appear to be common in geological
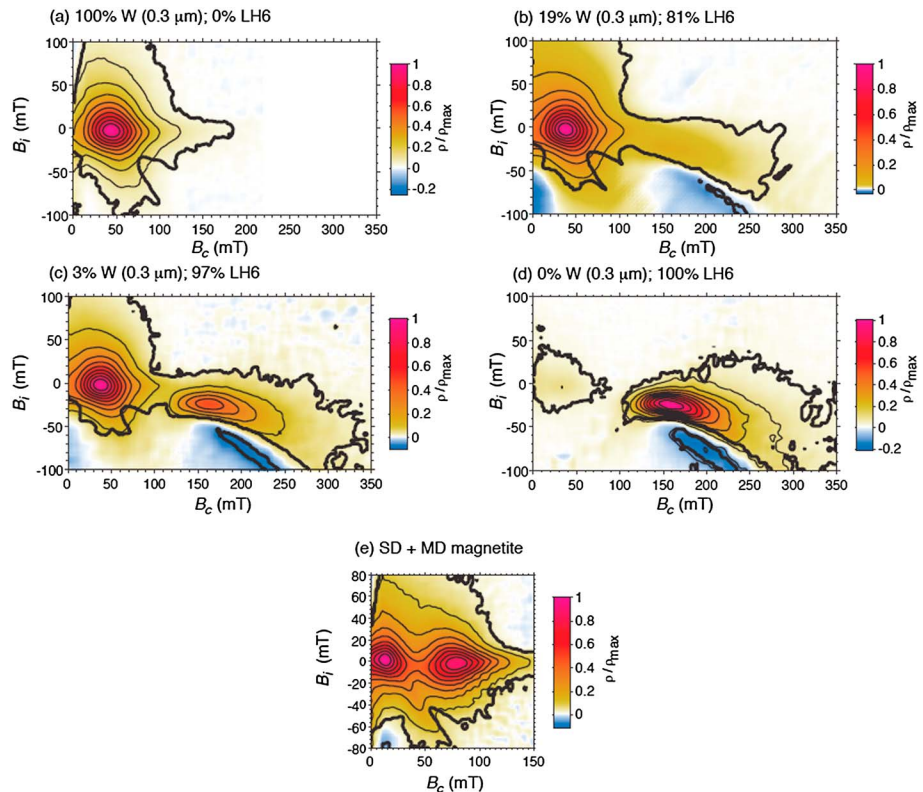
Figure 27. Examples of magnetic mixtures in FORC diagrams. For mixtures of magnetite and hematite [after *Muxworthy et al.*, 2005]: (a) 100% magnetite (W 0.3 μm) and 0% hematite (sample LH6; nominal size range of 75–100 μm [*Hartstra*, 1982]). The large difference in spontaneous magnetization between magnetite and hematite means that large hematite concentrations must be present before hematite becomes visible when magnetite is also present. (b) Mixture of 19% of W (0.3 μm) and 81% of LH6. Hematite is evident as an additional contribution at higher coercivities compared to Figure 27a. (c) A mixture of 3% of W (0.3 μm) and 97% of LH6. (d) 100% hematite (LH6). (e) FORC diagram measured at 20 K after zero-field cooling for a mixture of acicular SD and MD magnetite [from *Smirnov*, 2006]. For Figures 27a–27d, SF = 3; for 27e, SF = 5.

samples; ternary or more complex mixing appears to be more common [*Heslop and Roberts*, 2012b, 2012c; *Roberts et al.*, 2013]. Samples that contain only a single magnetic mineral can also consist of particles with mixed domain states. For example, greigite often occurs in an interacting SD state as well as in an SP state [*Roberts et al.*, 2011b]. Variable mixtures of the two will also produce a mixing trend on a Day diagram (Figure 26b) [*Rowan and Roberts*, 2006; *Heslop and Roberts*, 2012b].

In contrast to the natural mixing systems discussed above, it is instructive to artificially mix magnetic minerals to understand the limitations of FORC diagrams for quantifying mixing. *Muxworthy et al.* [2005] measured FORC diagrams for varying artificial binary magnetic mineral mixtures. When mixing magnetite and hematite (Figures 27a–27d), they found critical concentrations at which the strongly magnetic phase (magnetite) magnetically swamps the contribution from the weakly magnetic phase (hematite) so that it becomes undetectable. For example, even when hematite represents 81% of the mixture by mass, it is barely detectable (Figure 27b). *Carvallo et al.* [2006b] compared micromagnetic simulations and FORC measurements for magnetic mineral mixtures and found that for mixtures of hematite and magnetite, hematite must comprise at least 88% of the mixture (by mass) to be detectable. *Smirnov* [2006] mixed acicular SD with MD magnetite and found that these contrasting grain sizes provide a distinctive mixed signature on a FORC diagram (Figure 27e). FORC diagrams have also proven useful for identifying magnetic mixtures created by laboratory heating [*Wang et al.*, 2008; *Jovane et al.*, 2011].

Based partially on the studies cited above, it is widely recognized that geological samples routinely comprise mixtures of multiple magnetic components [*Heslop and Roberts*, 2012c]. Even in white pelagic carbonates
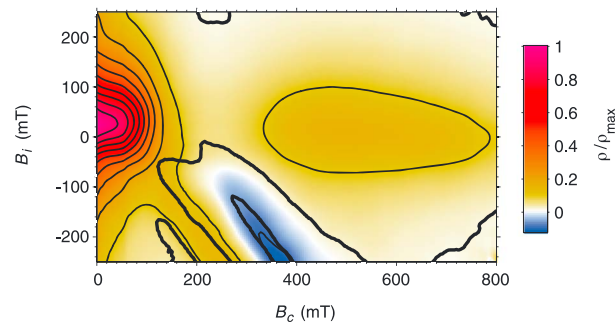
Figure 28. FORC diagram (SF = 4) for the Bjurbole-L5 chondrule [after *Acton et al.*, 2007b]. The sample has three coercivity components (high, intermediate, and low). The large positive (upward) bias of the FORC distribution at intermediate coercivities is attributed to interactions between the intermediate-coercivity component and nearby higher-coercivity and lower coercivity particles. The paired ridge/trough at −135° from the origin of the FORC diagram is attributed to interactions between low- and intermediate-coercivity components that cause magnetic moments to switch prior to the field polarity change in the FORC measurements. These distinctive features have yet to be reported from terrestrial materials.

deposited far from land, we routinely document at least four magnetic mineral components, including biogenic hard and soft magnetite, detrital magnetite, and detrital hematite [*Roberts et al.*, 2013]. FORC diagrams have played an important role in documenting such mixtures, including unmixing of central ridge signatures (Figure 11b) [*Ludwig et al.*, 2013; *Roberts et al.*, 2013; *Heslop et al.*, 2014]. The cases discussed above demonstrate the importance of unraveling magnetic mixtures in paleomagnetic, rock magnetic, and environmental magnetic investigations. Quantitative separation of FORC responses due to multiple magnetic components represents a major goal in these fields [*Roberts et al.*, 2000]. Recognition that noninteracting SD components can be separated from the rest of a FORC distribution, through subtraction

of the central ridge signature [*Egli et al.*, 2010], represents a major step toward unmixing of FORC signals. This significantly simplifies the task of unmixing remaining FORC components. The coming years should see increased focus on addressing this important problem. Success will enable rigorous quantitative mineral magnetic interpretation in wide-ranging research endeavors.

8.4. Hematite, Monoclinic Pyrrhotite, and Magnetite Below the Verwey Transition Temperature

In contrast to the approximately symmetrical FORC distributions for interacting SD particle systems (Figures 15a and 15b), so-called kidney- (or banana-) shaped features have often been observed in FORC diagrams for hematite and monoclinic pyrrhotite and for magnetite below the Verwey transition. The kidney-shaped structure is an asymmetric closed feature, as expected for interacting SD particles, with a negative region just below the main peak in the FORC diagram (Figures 15c and 27d). Most, and sometimes all, of this structure lies below $B_i = 0$. Such FORC distributions have been reported for hematite [*Muxworthy et al.*, 2005; *Carvallo et al.*, 2006b; *Brownlee et al.*, 2011; *Jovane et al.*, 2011], pyrrhotite [*Weaver et al.*, 2002; *Larrasoaña et al.*, 2007; *Roberts et al.*, 2010], and equidimensional PSD magnetite below the Verwey transition temperature at low applied fields [*Smirnov*, 2007]. *Roberts et al.* [2010] attributed similar kidney-shaped features for hematite and pyrrhotite to the fact that they both have similar magnetization mechanisms with spontaneous magnetization confined to the basal crystallographic plane [*Stacey and Banerjee*, 1974]. Below the Verwey transition, magnetite has a monoclinic structure, and its magnetic behavior is argued to be controlled by the interplay between magnetic and crystallographic twin domain structures [*Smirnov*, 2007]. Adequate explanation of kidney-shaped FORC features has yet to be provided and is needed to account for the observed magnetic properties of an important group of minerals.

8.5. Chondritic Meteorites

FORC diagrams for chondritic meteorites contain features that have not been reported from other materials [e.g., *Acton et al.*, 2007b; *Gattacceca et al.*, 2014]. In addition to FORC responses due to noninteracting and interacting SD tetrataenite particles, these materials can produce two additional otherwise uncommonly reported FORC responses (Figure 28). The first is a positive ridge that is accompanied by a parallel negative trough (to the right) that extends from the origin of the FORC diagram at 135° across the lower half of the diagram. This paired ridge/trough is attributed to interactions between low- and intermediate-coercivity components that cause magnetic moments to switch prior to the field polarity change in a FORC measurement [*Acton et al.*, 2007b; *Gattacceca et al.*, 2014]. The second distinctive feature is a large positive bias (to positive B_i values) of the FORC distribution that is attributed to magnetostatic interactions between intermediate-coercivity particles with nearby higher-coercivity and lower coercivity grains [*Acton et al.*, 2007b]. These features

result from interactions between two or more magnetic components with contrasting coercivity. Such features are much more pronounced than those observed so far for terrestrial materials [*Acton et al.*, 2007b] and confirm the power of FORC diagrams for understanding the origin of magnetic signals in fine magnetic particle systems. Along with the results of *Lappe et al.* [2013], they also demonstrate that FORC diagrams can provide important constraints on interaction-biased magnetic recording [e.g., *Dunlop*, 1969]. Such biasing needs to be tested for in absolute paleointensity studies of terrestrial and meteoritic materials.

8.6. Summary

This brief discussion about applications of FORC diagrams in the Earth sciences is far from exhaustive. Space limitations prevent more complete discussion. Suffice it to conclude that FORC diagrams are likely to continue to provide valuable information for understanding magnetic hysteresis mechanisms and for identifying domain state and interaction field distributions that will have wide geophysical, geological, and environmental applicability.

9. Conclusions

FORC diagrams are now widely used in geophysics, geology, environmental science, and solid-state physics. In this paper, we have synthesized an extensive literature that is relevant to interpretation of FORC diagrams in paleomagnetism, rock magnetism, and environmental magnetism. We describe important strategies for obtaining good FORC measurements, including sample preparation and technical considerations for suppressing measurement noise and making optimal calculations of FORC diagrams, including consideration of statistical significance. We also describe a framework for interpreting FORC distributions that has emerged over the last 15 years through experimental, theoretical, numerical, micromagnetic, and statistical approaches. This range of constraints is summarized to aid interpretation of the magnetic behavior of magnetostatically interacting and noninteracting single domain, superparamagnetic, multidomain, single vortex, and pseudosingle domain particle systems. These types of magnetic behavior are illustrated mainly with geological examples and a range of important applications are described to which FORC diagrams can be usefully applied. FORC diagrams will continue to be used to probe magnetization mechanisms in novel materials and to make new discoveries. The technical considerations expounded here should be of assistance in making such discoveries. Our synthesis of the manifestations of different types of magnetic behavior on FORC diagrams should enable researchers to better understand fine magnetic particle systems using FORC diagrams.

References

Abrajevitch, A., and K. Kodama (2009), Biochemical vs. detrital mechanism of remanence acquisition in marine carbonates: A lesson from the K-T boundary interval, *Earth Planet. Sci. Lett.*, *286*, 269–277.

Acton, G., A. Roth, and K. L. Verosub (2007a), Analyzing micromagnetic properties with FORCIT software, *Eos Trans. AGU*, *88*(21), 230, doi:10.1029/2007EO210004.

Acton, G., Q. Z. Yin, K. L. Verosub, L. Jovane, A. Roth, B. Jacobsen, and D. S. Ebel (2007b), Micromagnetic coercivity distributions and interactions in chondrules with implications for paleointensities of the early solar system, *J. Geophys. Res.*, *112*, B03S90, doi:10.1029/2006JB004655.

Barkhausen, H. (1935), *Lehrbuch der Elektronen-Röhren*, S. Hirzel Verlag, Leipzig, Germany.

Bertotti, G., V. Basso, and A. Magni (1999), Stochastic dynamics in quenched-in disorder and hysteresis, *J. Appl. Phys.*, *85*, 4355–4357.

Brownlee, S. J., J. M. Feinberg, T. Kasama, R. J. Harrison, G. R. Scott, and P. R. Renne (2011), Magnetic properties of ilmenite-hematite single crystals from the Ecstall pluton near Prince Rupert, British Columbia, *Geochem. Geophys. Geosyst.*, *12*, Q07Z29, doi:10.1029/2011GC003622.

Carvallo, C., and A. R. Muxworthy (2006), Low-temperature first-order reversal curve (FORC) diagrams for synthetic and natural samples, *Geochem. Geophys. Geosyst.*, *7*, Q09003, doi:10.1029/2006GC001299.

Carvallo, C., A. R. Muxworthy, D. J. Dunlop, and W. Williams (2003), Micromagnetic modeling of first-order reversal curve (FORC) diagrams for single-domain and pseudo-single-domain magnetite, *Earth Planet. Sci. Lett.*, *213*, 375–390.

Carvallo, C., Ö. Özdemir, and D. J. Dunlop (2004), First-order reversal curve (FORC) diagrams of elongated single-domain grains at high and low temperatures, *J. Geophys. Res.*, *109*, B04105, doi:10.1029/2003JB002539.

Carvallo, C., A. P. Roberts, R. Leonhardt, C. Laj, C. Kissel, M. Perrin, and P. Camps (2006a), Increasing the efficiency of paleointensity analyses by selection of samples using first-order reversal curve (FORC) diagrams, *J. Geophys. Res.*, *111*, B12103, doi:10.1029/2005JB004126.

Carvallo, C., A. R. Muxworthy, and D. J. Dunlop (2006b), First-order reversal curve (FORC) diagrams of magnetic mixtures: Micromagnetic models and measurements, *Phys. Earth Planet. Inter.*, *154*, 308–322.

Carvallo, C., S. Hickey, D. Faivre, and N. Menguy (2009), Formation of magnetite in *Magnetospirillum gryphiswaldense* studied with FORC diagrams, *Earth Planets Space*, *61*, 143–150.

Chang, L., A. P. Roberts, A. R. Muxworthy, Y. Tang, Q. Chen, C. J. Rowan, Q. Liu, and P. Pruner (2007), Magnetic characteristics of synthetic pseudo-single-domain and multi-domain greigite (Fe$_3$S$_4$), *Geophys. Res. Lett.*, *34*, L24304, doi:10.1029/2007GL032114.

Chang, L., A. P. Roberts, C. J. Rowan, Y. Tang, P. Pruner, Q. Chen, and C. S. Horng (2009), Low-temperature magnetic properties of greigite (Fe$_3$S$_4$), *Geochem. Geophys. Geosyst.*, *10*, Q01Y04, doi:10.1029/2008GC002276.

Chen, A. P., R. Egli, and B. M. Moskowitz (2005), A FORC in the road?, *IRM Quart.*, *15*(1), 8–11.

Chen, A. P., R. Egli, and B. M. Moskowitz (2007), First-order reversal curve (FORC) diagrams of natural and cultured biogenic magnetic particles, *J. Geophys. Res.*, *112*, B08S90, doi:10.1029/2006JB004575.

Church, N., J. M. Feinberg, and R. Harrison (2011), Low-temperature domain wall pinning in titanomagnetite: Quantitative modeling of multidomain first-order reversal curve diagrams and AC susceptibility, *Geochem. Geophys. Geosyst.*, *12*, Q07Z27, doi:10.1029/2011GC003538.

Cisowski, S. (1981), Interacting vs. non-interacting domain behavior in natural and synthetic samples, *Phys. Earth Planet. Inter.*, *26*, 56–62.

Cui, Y. L., K. L. Verosub, A. P. Roberts, and M. Kovacheva (1997), Mineral magnetic criteria for sample selection in archaeomagnetic studies, *J. Geomag. Geoelectr.*, *49*, 567–585.

Day, R., M. Fuller, and V. A. Schmidt (1977), Hysteresis properties of titanomagnetites: Grain size and composition dependence, *Phys. Earth Planet. Inter.*, *13*, 260–267.

de Groot, L. V., M. J. Dekkers, M. Visscher, and G. W. ter Maat (2014), Magnetic properties and paleointensities as function of depth in a Hawaiian lava flow, *Geochem. Geophys. Geosyst.*, *15*, 1096–1112, doi:10.1002/2013GC005094.

Dubrota, C. I., and A. Stancu (2013), What does a first-order reversal curve diagram really mean? A study case: Array of ferromagnetic nanowires, *J. Appl. Phys.*, *113*, 043928, doi:10.1063/1.4789613.

Dumas, R. K., C. P. Li, I. V. Roshchin, I. K. Schuller, and K. Liu (2007a), Magnetic fingerprints of sub-100 nm Fe dots, *Phys. Rev. B*, *75*, 134405, doi:10.1103/PhysRevB.75.134405.

Dumas, R. K., K. Liu, C. P. Li, I. V. Roshchin, and I. K. Schuller (2007b), Temperature induced single domain-vortex state transition in sub-100 nm Fe nanodots, *Appl. Phys. Lett.*, *91*, 202501, doi:10.1063/1.2807276.

Dunin-Borkowski, R. E., M. R. McCartney, R. B. Frankel, D. A. Bazylinski, M. Pósfai, and P. R. Buseck (1998), Magnetic microstructure of magnetotactic bacteria by electron holography, *Science*, *282*, 1868–1870.

Dunlop, D. J. (1969), Interactions in rocks and the reliability of paleointensity data, *Earth Planet. Sci. Lett.*, *7*, 178–182.

Dunlop, D. J. (1986), Hysteresis properties of magnetite and their dependence on particle size: A test of pseudo-single-domain remanence models, *J. Geophys. Res.*, *91*, 9569–9584, doi:10.1029/JB091iB09p09569.

Dunlop, D. J. (2002), Theory and application of the Day plot (M_{rs}/M_s versus H_{cr}/H_c): 1. Theoretical curves and tests using titanomagnetite data, *J. Geophys. Res.*, *107*(B3), 2056, doi:10.1029/2001JB000486.

Dunlop, D. J., M. F. Westcott-Lewis, and M. E. Bailey (1990), Preisach diagrams and anhysteresis: Do they measure interactions?, *Phys. Earth Planet. Inter.*, *65*, 62–77.

Egli, R. (2004), Characterization of individual rock magnetic components by analysis of remanence curves. 1. Unmixing natural sediments, *Stud. Geophys. Geod.*, *48*, 391–446.

Egli, R. (2006), Theoretical aspects of dipolar interactions and their appearance in first-order reversal curves of thermally activated single-domain particles, *J. Geophys. Res.*, *111*, B12S17, doi:10.1029/2006JB004567.

Egli, R. (2013), VARIFORC: An optimized protocol for calculating non-regular first-order reversal curve (FORC) diagrams, *Global Planet. Change*, *110*, 302–320.

Egli, R., A. P. Chen, M. Winklhofer, K. P. Kodama, and C. S. Horng (2010), Detection of noninteracting single domain particles using first-order reversal curve diagrams, *Geochem. Geophys. Geosyst.*, *11*, Q01Z11, doi:10.1029/2009GC002916.

Ewing, J. A. (1882), On effects of retentiveness in the magnetisation of iron and steel, *Proc. R. Soc. London*, *34*, 39–45.

Fabian, K., and T. von Dobeneck (1997), Isothermal magnetization of samples with stable Preisach function: A survey of hysteresis, remanence, and rock magnetic parameters, *J. Geophys. Res.*, *102*, 17,659–17,677, doi:10.1029/97JB01051.

Fischer, H., G. Mastrogiacomo, J. F. Löffler, R. J. Warthmann, P. G. Weidler, and A. U. Gehring (2008), Ferromagnetic resonance and magnetic characteristics of intact magnetosome chains in *Magnetospirillum gryphiswaldense*, *Earth Planet. Sci. Lett.*, *270*, 200–208.

Flanders, P. J. (1991), An alternating gradient magnetometer, *J. Appl. Phys.*, *63*, 3940–3945.

Foner, S. (1959), Versatile and sensitive vibrating-sample magnetometer, *Rev. Sci. Instrum.*, *30*, 548–557.

Gattacceca, J., C. Suavet, P. Rochette, B. P. Weiss, M. Winklhofer, M. Uehara, and J. M. Friedrich (2014), Metal phases in ordinary chondrites: Magnetic hysteresis properties and implications for thermal history, *Meteorit. Planet. Sci.*, *49*, 652–676.

Geiss, C. E., R. Egli, and C. W. Zanner (2008), Direct estimates of pedogenic magnetite as a tool to reconstruct past climates from buried soils, *J. Geophys. Res.*, *113*, B11102, doi:10.1029/2008JB005669.

Halgedahl, S., and M. Fuller (1983), The dependence of magnetic domain structure upon magnetization state with emphasis upon nucleation as a mechanism for pseudo-single-domain behavior, *J. Geophys. Res.*, *88*, 6505–6522, doi:10.1029/JB088iB08p06505.

Hanzlik, M., M. Winklhofer, and N. Petersen (2002), Pulsed-field-remanence measurements on individual magnetotactic bacteria, *J. Magn. Magn. Mater.*, *248*, 258–267.

Harrison, R. J., and J. M. Feinberg (2008), FORCinel: An improved algorithm for calculating first-order reversal curve distributions using locally weighted regression smoothing, *Geochem. Geophys. Geosyst.*, *9*, Q05016, doi:10.1029/2008GC001987.

Hartstra, R. L. (1982), Some rock magnetic parameters for natural iron-titanium oxides, PhD thesis, Utrecht Univ., Utrecht, Netherlands.

Hejda, P., and T. Zelinka (1990), Modelling of hysteresis processes in magnetic rock samples using the Preisach diagram, *Phys. Earth Planet. Inter.*, *63*, 32–40.

Henkel, O. (1964), Remanenzverhalten und wechselwirkungen in hartmagnetischen teilchenkollektiven, *Phys. Status Solidi*, *7*, 919–924.

Heslop, D., and A. R. Muxworthy (2005), Aspects of calculating first-order reversal curve distributions, *J. Magn. Magn. Mater.*, *288*, 155–167.

Heslop, D., and A. P. Roberts (2012a), Estimation of significance levels and confidence intervals for first-order reversal curve distributions, *Geochem. Geophys. Geosyst.*, *13*, Q12Z40, doi:10.1029/2012GC004115.

Heslop, D., and A. P. Roberts (2012b), Estimating best-fit binary mixing lines in the Day plot, *J. Geophys. Res.*, *117*, B01101, doi:10.1029/2011JB008787.

Heslop, D., and A. P. Roberts (2012c), A method for unmixing magnetic hysteresis loops, *J. Geophys. Res.*, *117*, B03103, doi:10.1029/2011JB008859.

Heslop, D., M. J. Dekkers, P. P. Kruiver, and I. H. M. van Oorschot (2002), Analysis of isothermal remanent magnetization acquisition curves using the expectation-maximization algorithm, *Geophys. J. Int.*, *148*, 58–64.

Heslop, D., G. McIntosh, and M. J. Dekkers (2004), Using time- and temperature-dependent Preisach models to investigate the limitations of modelling isothermal remanent magnetization acquisition curves with cumulative log Gaussian functions, *Geophys. J. Int.*, *157*, 55–63.

Heslop, D., A. P. Roberts, and L. Chang (2014), Characterizing magnetofossils from first-order reversal curve central ridge signatures, *Geochem. Geophys. Geosyst.*, *15*, 2170–2179, doi:10.1002/2014GC005291.

Ivanov, V. A., and L. Y. Sholpo (1982), Quantitative criteria for single- and multi-domain states in ferromagnetic minerals in rocks, *Izvestiya Earth Phys.*, *18*, 612–616.

Ivanov, V. A., I. A. Khaburzaniya, and L. Y. Sholpo (1981), Use of Preisach diagram for diagnosis of single- and multi-domain grains in rock samples, *Izvestiya Earth Phys.*, *17*, 36–43.

Jackson, M., and P. Solheid (2010), On the quantitative analysis and evaluation of magnetic hysteresis data, *Geochem. Geophys. Geosyst.*, *11*, Q04Z15, doi:10.1029/2009GC002932.

Jacobs, I. S., and C. P. Bean (1955), An approach to elongated fine-particle magnets, *Phys. Rev.*, *100*, 1060–1067.

Jovane, L., E. Yokoyama, T. Seda, R. F. Burmester, R. I. F. Trindade, and B. A. Housen (2011), Rock magnetism of hematitic "bombs" from the Araguainha impact structure, Brazil, *Geochem. Geophys. Geosyst.*, *12*, Q12Z34, doi:10.1029/2011GC003758.

Jovane, L., F. Florindo, D. A. Bazylinski, and U. Lins (2012), Prismatic magnetite magnetosomes from cultivated *Magnetovibrio blakemorei* strain MV-1: A magnetic fingerprint in marine sediments?, *Environ. Microbiol. Rep.*, *4*, 664–668.

Kind, J., A. U. Gehring, M. Winklhofer, and A. M. Hirt (2011), Combined use of magnetometry and spectroscopy for identifying magnetofossils in sediments, *Geochem. Geophys. Geosyst.*, *12*, Q08008, doi:10.1029/2011GC003633.

Kissel, C., and C. Laj (2004), Improvements in procedure and paleointensity selection criteria (PICRIT-03) for Thellier and Thellier determinations: Applications to Hawaiian basaltic long cores, *Phys. Earth Planet. Inter.*, *147*, 155–169.

Krása, D., C. D. W. Wilkinson, N. Gadegaard, X. Kong, H. Zhou, A. P. Roberts, A. R. Muxworthy, and W. Williams (2009), Nanofabrication of two dimensional arrays of magnetite particles for fundamental rock magnetic studies, *J. Geophys. Res.*, *114*, B02104, doi:10.1029/2008JB006017.

Krása, D., A. R. Muxworthy, and W. Williams (2011), Room- and low-temperature magnetic properties of 2-D magnetite particle arrays, *Geophys. J. Int.*, *185*, 167–180.

Kruiver, P. P., M. J. Dekkers, and D. Heslop (2001), Quantification of magnetic coercivity components by the analysis of acquisition curves of isothermal remanent magnetization, *Earth Planet. Sci. Lett.*, *189*, 269–276.

Kruiver, P. P., C. G. Langereis, M. J. Dekkers, and W. Krijgsman (2003), Rock-magnetic properties of multicomponent natural remanent magnetization in alluvial red beds (NE Spain), *Geophys. J. Int.*, *153*, 317–322.

Lappe, S.-C. L. L., N. S. Church, T. Kasama, A. Bastos da Silva Fanta, G. Bromiley, R. E. Dunin-Borkowski, J. M. Feinberg, S. Russell, and R. J. Harrison (2011), Mineral magnetism of dusty olivine: A credible recorder of pre-accretionary remanence, *Geochem. Geophys. Geosyst.*, *12*, Q12Z35, doi:10.1029/2011GC003811.

Lappe, S.-C. L. L., J. M. Feinberg, A. Muxworthy, and R. J. Harrison (2013), Comparison and calibration of nonheating paleointensity methods: A case study using dusty olivine, *Geochem. Geophys. Geosyst.*, *14*, 2143–2158, doi:10.1002/ggge.20141.

Larrasoaña, J. C., A. P. Roberts, R. J. Musgrave, E. Gràcia, E. Piñero, M. Vega, and F. Martínez-Ruiz (2007), Diagenetic formation of greigite and pyrrhotite in marine sedimentary systems containing gas hydrates, *Earth Planet. Sci. Lett.*, *261*, 350–366.

Larrasoaña, J. C., A. P. Roberts, L. Chang, S. A. Schellenberg, J. D. Fitz Gerald, R. D. Norris, and J. C. Zachos (2012), Magnetotactic bacterial response to Antarctic dust supply during the Palaeocene-Eocene thermal maximum, *Earth Planet. Sci. Lett.*, *333–334*, 122–133.

Li, J., Y. Pan, G. Chen, Q. Liu, L. Tian, and W. Lin (2009), Magnetite magnetosome and fragmental chain formation of *Magnetospirillum magneticum* AMB-1: Transmission electron microscopy and magnetic observations, *Geophys. J. Int.*, *177*, 33–42.

Ludwig, P., R. Egli, S. Bishop, V. Chernenko, T. Frederichs, S. Rugel, S. Merchel, and M. J. Orgeira (2013), Characterization of primary and secondary magnetite in marine sediment by combining chemical and magnetic unmixing techniques, *Global Planet. Change*, *110*, 321–339.

Mayergoyz, I. D. (1986), Mathematical models of hysteresis, *IEEE Trans. Magn.*, *MAG-22*, 603–608.

Moskowitz, B. M., R. B. Frankel, and D. A. Bazylinski (1993), Rock magnetic criteria for the detection of biogenic magnetite, *Earth Planet. Sci. Lett.*, *120*, 283–300.

Mullins, C. E., and M. S. Tite (1973), Preisach diagrams and magnetic viscosity phenomena for soils and synthetic assemblies of iron oxide grains, *J. Geomag. Geoelectr.*, *25*, 213–229.

Muxworthy, A. R., and D. J. Dunlop (2002), First-order reversal curve (FORC) diagrams for pseudo-single-domain magnetites at high temperature, *Earth Planet. Sci. Lett.*, *203*, 369–382.

Muxworthy, A. R., and D. Heslop (2011), A Preisach method for estimating absolute paleofield intensity under the constraint of using only isothermal measurements: 1. Theoretical framework, *J. Geophys. Res.*, *116*, B04102, doi:10.1029/2010JB007843.

Muxworthy, A. R., and A. P. Roberts (2007), First-order reversal curve (FORC) diagrams, in *Encyclopedia of Geomagnetism and Paleomagnetism*, *Encycl. Earth Sci. Ser.*, edited by D. Gubbins and E. Herrero-Bervera, pp. 266–272, Springer, Dordrecht, Netherlands.

Muxworthy, A. R., and W. Williams (2005), Magnetostatic interaction fields in first-order-reversal curve diagrams, *J. Appl. Phys.*, *97*, 063905, doi:10.1063/1.1861518.

Muxworthy, A. R., and W. Williams (2009), Critical superparamagnetic/single domain grain sizes in interacting magnetite particles: Implications for magnetosome crystals, *J. R. Soc. Interface*, *6*, 1207–1212.

Muxworthy, A. R., W. Williams, and D. Virdee (2003), Effect of magnetostatic interactions on the hysteresis properties of single-domain and pseudo-single domain grains, *J. Geophys. Res.*, *108*(B11), 2517, doi:10.1029/2003JB002588.

Muxworthy, A. R., D. Heslop, and W. Williams (2004), Influence of magnetostatic interactions on first-order-reversal-curve (FORC) diagrams: A micromagnetic approach, *Geophys. J. Int.*, *158*, 888–897.

Muxworthy, A. R., J. G. King, and D. Heslop (2005), Assessing the ability of first-order reversal curve (FORC) diagrams to unravel complex magnetic signals, *J. Geophys. Res.*, *110*, B01105, doi:10.1029/2004JB003195.

Muxworthy, A. R., D. Heslop, G. A. Paterson, and D. Michalk (2011), A Preisach method for estimating absolute paleofield intensity under the constraint of using only isothermal measurements: 2. Experimental testing, *J. Geophys. Res.*, *116*, B04103, doi:10.1029/2010JB007844.

Néel, L. (1949), Théorie du trainage magnétique des ferromagnétiques en grains fin avec application aux terres cuites, *Ann. Geophys.*, *5*, 99–136.

Néel, L. (1954), Remarques sur la théorie des propriétés magnétiques des substances dures, *Appl. Sci. Res., Sect. B*, *4*, 13–24.

Néel, L. (1955), Some theoretical aspects of rock magnetism, *Adv. Phys.*, *4*, 191–243.

Newell, A. J. (2005), A high-precision model of first-order reversal curve (FORC) functions for single-domain ferromagnets with uniaxial anisotropy, *Geochem. Geophys. Geosyst.*, *6*, Q05010, doi:10.1029/2004GC000877.

Pan, Y. X., N. Petersen, M. Winklhofer, A. F. Davila, Q. S. Liu, T. Frederichs, M. Hanzlik, and R. X. Zhu (2005), Rock magnetic properties of uncultured magnetotactic bacteria, *Earth Planet. Sci. Lett.*, *237*, 311–325.

Paterson, G., A. R. Muxworthy, A. P. Roberts, and C. MacNiocaill (2010), Assessment of the usefulness of lithic clasts from pyroclastic deposits for paleointensity determination, *J. Geophys. Res.*, *115*, B03104, doi:10.1029/2009JB006475.

Penninga, I., H. de Waard, B. M. Moskowitz, D. A. Bazylinski, and R. B. Frankel (1995), Remanence measurements on individual magnetotactic bacteria using a pulsed magnetic field, *J. Magn. Magn. Mater.*, *149*, 279–286.

Perrin, M. (1998), Paleointensity determination, magnetic domain structure, and selection criteria, *J. Geophys. Res.*, *103*, 30,591–30,600, doi:10.1029/98JB01466.

Pike, C., and A. Fernandez (1999), An investigation of magnetic reversal in submicron-scale Co dots using first order reversal curve diagrams, *J. Appl. Phys.*, *85*, 6668–6676.

Pike, C., and J. Marvin (2001), FORC analysis of frozen ferrofluids, *IRM Quart.*, *11*(1), 10–11.

Pike, C. R. (2003), First-order reversal-curve diagrams and reversible magnetization, *Phys. Rev. B*, *68*, 104424, doi:10.1103/PhysRevB.68.104424.

Pike, C. R., A. P. Roberts, and K. L. Verosub (1999), Characterizing interactions in fine magnetic particle systems using first order reversal curves, *J. Appl. Phys.*, *85*, 6660–6667.

Pike, C. R., A. P. Roberts, and K. L. Verosub (2001a), First-order reversal curve diagrams and thermal relaxation effects in magnetic particles, *Geophys. J. Int.*, *145*, 721–730.

Pike, C. R., A. P. Roberts, M. J. Dekkers, and K. L. Verosub (2001b), An investigation of multi-domain hysteresis mechanisms using FORC diagrams, *Phys. Earth Planet. Inter.*, *126*, 11–25.

Pike, C. R., C. A. Ross, R. T. Scalettar, and G. Zimanyi (2005), First-order reversal curve diagram analysis of a perpendicular nickel nanopillar array, *Phys. Rev. B*, *71*, 134407, doi:10.1103/PhysRevB.71.134407.

Preisach, F. (1935), Über die magnetische Nachwirkung, *Z. Phys.*, *94*, 277–302.

Proenca, M. P., C. T. Sousa, J. Escrig, J. Ventura, M. Vazquez, and J. P. Araujo (2013), Magnetic interactions and reversal mechanisms in Co nanowire and nanotube arrays, *J. Appl. Phys.*, *113*, 093907, doi:10.1063/1.4794335.

Roberts, A. P., and G. M. Turner (1993), Diagenetic formation of ferrimagnetic iron sulphide minerals in rapidly deposited marine sediments, New Zealand, *Earth Planet. Sci. Lett.*, *115*, 257–273.

Roberts, A. P., R. L. Reynolds, K. L. Verosub, and D. P. Adam (1996), Environmental magnetic implications of greigite (Fe_3S_4) formation in a 3 million year lake sediment record from Butte Valley, Northern California, *Geophys. Res. Lett.*, *23*, 2859–2862, doi:10.1029/96GL02831.

Roberts, A. P., C. R. Pike, and K. L. Verosub (2000), FORC diagrams: A new tool for characterizing the magnetic properties of natural samples, *J. Geophys. Res.*, *105*, 28,461–28,475, doi:10.1029/2000JB900326.

Roberts, A. P., Q. S. Liu, C. J. Rowan, L. Chang, C. Carvallo, J. Torrent, and C. S. Horng (2006), Characterization of hematite (α-Fe_2O_3), goethite (α-$FeOOH$), greigite (Fe_3S_4), and pyrrhotite (Fe_7S_8) using first-order reversal curve diagrams, *J. Geophys. Res.*, *111*, B12S35, doi:10.1029/2006JB004715.

Roberts, A. P., F. Florindo, J. C. Larrasoaña, M. A. O'Regan, and X. Zhao (2010), Complex polarity pattern at the (former) Plio-Pleistocene global stratotype section at Vrica (Italy): Remagnetization by magnetic iron sulphides, *Earth Planet. Sci. Lett.*, *292*, 98–111.

Roberts, A. P., F. Florindo, G. Villa, L. Chang, L. Jovane, S. M. Bohaty, J. C. Larrasoaña, D. Heslop, and J. D. Fitz Gerald (2011a), Magnetotactic bacterial abundance in pelagic marine environments is limited by organic carbon flux and availability of dissolved iron, *Earth Planet. Sci. Lett.*, *310*, 441–452.

Roberts, A. P., L. Chang, C. J. Rowan, C. S. Horng, and F. Florindo (2011b), Magnetic properties of sedimentary greigite (Fe_3S_4): An update, *Rev. Geophys.*, *49*, RG1002, doi:10.1029/2010RG000336.

Roberts, A. P., L. Chang, D. Heslop, F. Florindo, and J. C. Larrasoaña (2012), Searching for single domain magnetite in the "pseudo-single-domain" sedimentary haystack: Implications of biogenic magnetite preservation for sediment magnetism and relative paleointensity determinations, *J. Geophys. Res.*, *117*, B08104, doi:10.1029/2012JB009412.

Roberts, A. P., F. Florindo, L. Chang, D. Heslop, L. Jovane, and J. C. Larrasoaña (2013), Magnetic properties of pelagic marine carbonates, *Earth Sci. Rev.*, *127*, 111–139.

Robertson, D. J., and D. E. France (1994), Discrimination of remanence-carrying minerals in mixtures, using isothermal remanent magnetisation acquisition curves, *Phys. Earth Planet. Inter.*, *84*, 223–234.

Rochette, P., P. E. Mathé, L. Esteban, H. Rakoto, J. L. Bouchez, Q. S. Liu, and J. Torrent (2005), Non-saturation of the defect moment of goethite and fine-grained hematite up to 57 Teslas, *Geophys. Res. Lett.*, *32*, L22309, doi:10.1029/2005GL024196.

Rosenbaum, J. G. (1993), Magnetic grain-size variations through an ash flow sheet: Influence on magnetic properties and implications for cooling history, *J. Geophys. Res.*, *98*, 11,715–11,727, doi:10.1029/93JB00355.

Rowan, C. J., and A. P. Roberts (2006), Magnetite dissolution, diachronous greigite formation, and secondary magnetizations from pyrite oxidation: Unravelling complex magnetizations in Neogene marine sediments from New Zealand, *Earth Planet. Sci. Lett.*, *241*, 119–137.

Schabes, M. E., and H. N. Bertram (1988), Magnetization processes in ferromagnetic cubes, *J. Appl. Phys.*, *64*, 1347–1357.

Schlinger, C. M., J. G. Rosenbaum, and D. R. Veblen (1988), Fe-oxide microcrystals in welded tuff from southern Nevada: Origin of remanence carriers by precipitation in volcanic glass, *Geology*, *16*, 556–559.

Smirnov, A. V. (2006), Low-temperature magnetic properties of magnetite using first-order reversal curve analysis: Implications for the pseudo-single domain state, *Geochem. Geophys. Geosyst.*, *7*, Q11011, doi:10.1029/2006GC001397.

Smirnov, A. V. (2007), Effect of the magnetic field applied during cooling on magnetic hysteresis in the low-temperature phase of magnetite: First-order reversal curve (FORC) analysis, *Geochem. Geophys. Geosyst.*, *8*, Q08005, doi:10.1029/2007GC001650.

Sprowl, D. R. (1990), Numerical estimation of interactive effects in single-domain magnetite, *Geophys. Res. Lett.*, *17*, 2009–2012, doi:10.1029/GL017i011p02009.

Stacey, F. D. (1963), The physical theory of rock magnetism, *Adv. Phys.*, *12*, 45–133.

Stacey, F. D., and S. K. Banerjee (1974), *The Physical Principles of Rock Magnetism*, Elsevier, New York.

Stancu, A., C. Pike, L. Stoleriu, P. Postolache, and D. Cimpoesu (2003), Micromagnetic and Preisach analysis of the first order reversal curves (FORC) diagram, *J. Appl. Phys.*, *93*, 6620–6622.

Stoner, E. C., and E. P. Wohlfarth (1948), A mechanism of magnetic hysteresis in heterogeneous alloys, *Philos. Trans. R. Soc. London, Ser. A*, *240*, 599–642.

Tarduno, J. A., R. D. Cottrell, and A. V. Smirnov (2006), The paleomagnetism of single silicate crystals: Recording geomagnetic field strength during mixed polarity intervals, superchrons, and inner core growth, *Rev. Geophys.*, *44*, RG1002, doi:10.1029/2005RG000189.

Tauxe, L., H. N. Bertram, and C. Seberino (2002), Physical interpretation of hysteresis loops: Micromagnetic modeling of fine particle magnetite, *Geochem. Geophys. Geosyst.*, *3*(10), 1055, doi:10.1029/2001GC000241.

Thellier, E. (1938), Sur l'aimantation des terres cuites et ses applications geophysiques, *Ann. Inst. Phys. Globe Univ. Paris*, *16*, 157–302.

Thellier, E., and O. Thellier (1959), Sur l'intensité du champ magnétique terrestre dans la passé historique et géologique, *Ann. Géophys.*, *15*, 285–376.

Thomas, D. N. (1993), An integrated rock magnetic approach to the selection or rejection of ancient basalt samples for palaeointensity experiments, *Phys. Earth Planet. Inter.*, *75*, 329–342.

Till, J. L., M. J. Jackson, J. G. Rosenbaum, and P. Solheid (2011), Magnetic properties in an ash flow tuff with continuous grain size variation: A natural reference for magnetic particle granulometry, *Geochem. Geophys. Geosyst.*, *12*, Q07Z26, doi:10.1029/2011GC003648.

Uhlenbeck, G. E., and L. S. Ornstein (1930), On the theory of Brownian Motion, *Phys. Rev.*, *36*, 823–841.

Vajda, F., and E. Della Torre (1991), Relationship between the moving and the product Preisach model, *IEEE Trans. Magn.*, *MAG-27*, 3823–3826.

Vasiliev, I., M. J. Dekkers, W. Krijgsman, C. Franke, C. G. Langereis, and T. A. T. Mullender (2007), Early diagenetic greigite as a recorder of the palaeomagnetic signal in Miocene-Pliocene sedimentary rocks of the Carpathian foredeep (Romania), *Geophys. J. Int.*, *171*, 613–629.

Wang, L., Y. X. Pan, J. H. Li, and H. F. Qin (2008), Magnetic properties related to thermal treatment of pyrite, *Sci. China D*, *51*, 1144–1153.

Weaver, R., A. P. Roberts, and A. J. Barker (2002), A late diagenetic (syn-folding) magnetization carried by pyrrhotite: Implications for paleomagnetic studies from magnetic iron sulphide-bearing sediments, *Earth Planet. Sci. Lett.*, *200*, 371–386.

Wehland, F., A. Stancu, P. Rochette, M. J. Dekkers, and E. Appel (2005a), Experimental evaluation of magnetic interaction in pyrrhotite bearing samples, *Phys. Earth Planet. Inter.*, *153*, 181–190.

Wehland, F., R. Leonhardt, F. Vadeboin, and E. Appel (2005b), Magnetic interaction analysis of basaltic samples and pre-selection for absolute paleointensity measurements, *Geophys. J. Int.*, *162*, 315–320.

Wilde, H., and H. Girke (1959), Die messung der wahrscheinlichkeitsverteilung der Barkhausensprünge in einem ferromagnetikum, *Z. Angew. Phys.*, *11*, 339–342.

Williams, W., and D. J. Dunlop (1989), Three-dimensional micromagnetic modelling of ferromagnetic domain structure, *Nature*, *337*, 634–637.

Williams, W., and D. J. Dunlop (1995), Simulation of magnetic hysteresis in pseudo-single-domain grains of magnetite, *J. Geophys. Res.*, *100*, 3859–3871, doi:10.1029/94JB02878.

Winklhofer, M., and G. T. Zimanyi (2006), Extracting the intrinsic switching field distribution in perpendicular media: A comparative analysis, *J. Appl. Phys.*, *99*, 08E710, doi:10.1063/1.2176598.

Worm, H.-U. (1998), On the superparamagnetic–stable single domain transition for magnetite, and frequency dependence of susceptibility, *Geophys. J. Int.*, *133*, 201–206.

Worm, H.-U. (1999), Time-dependent IRM: A new technique for magnetic granulometry, *Geophys. Res. Lett.*, *26*, 2557–2560, doi:10.1029/1999GL008360.

Worm, H.-U., and M. Jackson (1998), The superparamagnetism of Yucca Mountain Tuff, *J. Geophys. Res.*, *104*, 25,415–25,425, doi:10.1029/1999JB900285.

Yamazaki, T. (2008), Magnetostatic interactions in deep-sea sediments inferred from first-order reversal curve diagrams: Implications for relative paleointensity normalization, *Geochem. Geophys. Geosyst.*, *9*, Q02005, doi:10.1029/2007GC001797.

Yamazaki, T. (2009), Environmental magnetism of Pleistocene sediments in the North Pacific and Ontong-Java Plateau: Temporal variations of detrital and biogenic components, *Geochem. Geophys. Geosyst.*, *10*, Q07Z04, doi:10.1029/2009GC002413.

Yamazaki, T. (2012), Paleoposition of the Intertropical Convergence Zone in the eastern Pacific inferred from glacial-interglacial changes in terrigenous and biogenic magnetic mineral fractions, *Geology*, *40*, 151–154.

Zelinka, T., P. Hejda, and V. Kropacek (1987), The vibrating-sample magnetometer and Preisach diagram, *Phys. Earth Planet. Inter.*, *46*, 241–246.